Towards a weak measurement of transverse momentum in a matter-wave interferometer

Joel Morley

A thesis submitted to University College London
in partial fulfilment of the requirements for the
degree of Doctor of Philosophy

Department of Physics and Astronomy
University College London
March 2020

I, Joel Morley, confirm that the work presented in this thesis is my own. Where information has been derived from other sources, I confirm that this has been indicated in the thesis.

Signed .... Date ....

Abstract

This thesis describes the construction of an atomic matter-wave interferometer, combined with a spin-state interferometer, used to weakly measure the average transverse momentum of the atoms.

A velocity-tuneable cold atomic beam was constructed and characterised. By applying radiation pressure to a magneto-optical trap, the beam's velocity was selected between $1 - 52\,\mathrm{ms}^{-1}$. The beam was used to produce interference fringes in a matter-wave interferometer which consisted of a mutli-slit Si_3Ni_4 grating and a planar atom detector placed below the grating. The interference pattern was used to measure the average beam velocity and the Van der Waals coefficient between the atoms and the grating. This was the first instance of such a measurement.

Below the grating a longitudinal Stern-Gerlach interferometer was constructed. The phase shift of the atom's spin, due to the Zeeman effect from the interferometer's magnetic field, was measured. The phase shift provided a measurement of the interferometer's magnetic field in the μT range.

An experiment combining the two interferometers to weakly measure the atom's transverse momentum is described and modelled.

Impact Statement

The experiment developed in this thesis is a necessary progression of the photonic experiment carried out by Kocsis et al., an experiment which was considered the breakthrough of the year by IOP's Physics World magazine. The experiment challenged widely held notions about what information we are allowed to know about a quantum particle, in their case a photon. Our experiment takes this idea further by re-designing the experiment to work with atoms. Making such a measurement with atoms will add weight to alternative interpretations of quantum mechanics, inflating a discussion which is usually lost outside of the inner research circles. During the project, a biographical film about David Bohm was filmed and released. Members of our research group, including myself, were interviewed and the experiment described in this thesis was filmed. Other interviewees included the Dalai Lama and Sir Roger Penrose.

Contents

Acknowledgements

Working in physics research has often been a pleasure; watching friends' reactions while giving them a lab tour, solving that one problem you have spent months on or seeing my work being presented to scientists whom to me, were celebrities. It was also often a nightmare; weeks alone in the lab just after the death of my best friend or months of late, Friday night finishes trying to fix the same problem. But above all the work has always been a huge source of pride and inspiration. For years now I have been enjoying regular tussles with my brain and have been presented with such infuriatingly great mind-bending questions.

So much I have gleaned off a screen or out of a book, but the truly valuable skills could only be transferred from others. Almost all the credit for developing my skills must go to my supervisor, Peter Barker. First and foremost for having faith in me as a PhD student, despite it being 5 years since I had picked up a textbook. Also his patience in thoroughly explaining things and his experience in how to efficiently operate parts of the experiment, these things will stay with me for many years.

My other colleagues played their roles. The closest I got to a lab partner was Vincenzo Monachello, a great person to bounce ideas off, he has a positive demeanour who so many times burst into my lab and snapped me out of the black holes that tired experimenters can fall into. I received a huge amount of support, academic and personal, from our research group notably my second supervisor, Rob Flack. Bob Callaghan and Peter Van Reeth kindly took a lot of their time to help me with simulations and such. I could not forget Basil Hiley, who's mind was the linchpin of the group. A truly inspiring guy, whom it has been a real honour to work with. I also owe thanks to Pete and Lia who best knew all the hurdles and pitfalls waiting ahead and duly directed me.

I couldn't finish without thanking my parents, forever encouraging, supporting and providing everything I've needed to grow and then more. However above all, my largest thank you is reserved for Cristina. My partner of 7.5 years who had plans to live abroad, just around the time I was offered the position. She has put her life on hold for me. A selfless soul, who can always sacrifice herself for ones she loves. Someone who has supported me through my hardest times and even through hers. I can only hope that I can repay it all. This thesis is dedicated to her.

Publications

1. Morley, J., Edmunds, P.D. & Barker, P.F. (2016). Measuring the weak value of momentum in a double slit atom interferometer. Journal of Physics: Conference Series, 701(1), pp.14–16.

Chapter 1

Introduction

The interference fringes in the matter-wave double slit experiment have long been one of the prime examples of the strange implications of quantum theory. Different explanations of the experiment's results point to different interpretations of the theory, including wavefunction collapse, determinism and the principle of locality. The mathematics, regardless of the interpretation, has been successful in consistently predicting the outcomes of this and many other experiments. The most widely accepted interpretation of the mathematics is the Copenhagen interpretation. However, the interpretation states that 'generally, quantum systems do not have definite properties prior to being measured' and so offers no clear way of proving how the ensemble of individual particles produce the results. Consequently there is no agreement on the nature of any underlying reality of quantum theory [1]. One approach, from Bohm [2], takes the wavefunction as $\psi = R\exp\{iS/\hbar\}$ (where R is the amplitude and S is the phase, both are real) and applies it to the Schrödinger equation, splitting it into real and imaginary parts. The real part of the equation gives the local momentum of the particle as $p = \nabla S$. This allows individual particle trajectories or momentum flow lines to be drawn [3], a feature denied as meaningful by the Copenhagen interpretation. This idea was largely ignored, partly for political reasons, but also because there appeared to be no way of measuring this momentum. Interestingly, a recent experiment using a 'weak measurement' technique has drawn attention to a method for measuring an atom's transverse momentum in the double slit experiment, leading to the construction of the 'momentum flow lines'

This thesis does not attempt to speculate about the physical origins of these effects, but demonstrates how the momentum flow lines could be reconstructed by experiment. We develop a method to perform the measurement which aims to reconstruct the momentum flow lines for metastable argon in a multi-slit grating matter-wave interferometer.

1.1 Matter-wave interferometry

The wave like behaviour of matter was proposed by de Broglie in 1924 and was supported by empirical evidence with the observation of interference from diffracted electrons in 1927 [4] and neutrons in 1936 [5] that had been scattered by a crystal. The range of different particles with which to observe matter-wave behaviour was, for some time, limited to just electrons and neutrons. Electrons were used in a Mach-Zender interferometer in 1950 [6] and in 1954 Möllenstedt diffracted electrons with a bi-prism [7], which gave a electrons the choice of two spatially separated paths. In order to observe matter-wave interference with heavier or neutral particles, a more a direct particle analogy of Young's double slit experiment was required. The double or multi-slit experiment was still just out of reach for experimentalists at the time due to the nano meter scale that the double slits would need to be in order to resolve the interference fringes. Eventually Möllenstedt's student, Claus Jönsson, demonstrated electron interference using a multi-slit grating in 1961. They built a 1 μm period grating using early electron beam lithography techniques and electrolytically deposited copper [8]. The experiment used electrons with velocities of 1 x 10^8 $\mathrm{ms^{-1}}$ to show the diffraction, giving a de Broglie wavelength of 5×10^{-12} m. Fabricating such gratings created the opportunity to undertake interferometry with more massive particles. Since a physical grating can be simple to implement in an experiment and it does not rely on the electric or magnetic properties of the particle, the primary challenge was then to create a coherent beam of particles.

In 1991, atomic interference was demonstrated after transmission through a double slit [9]. This experiment used metastable helium atoms in an atomic beam. The small atomic mass gave a long de Broglie wavelength which coherently illuminated the 8 μm separated slits. In 1999, Ardnt et al. used C_{60} buckyballs to demonstrate wave behaviour of large molecules [10] and has since achieved results with ever increasing sizes and complexities of molecule. Most recently diffraction of molecules consisting of 810 atoms was demonstrated [11]. To achieve this superposition, the team used two nano fabricated gratings either side of a standing light wave, which is known as a Kapitza–Dirac–Talbot–Lau configuration. The Talbot-Lau configuration, referring to using multiple gratings to exploit the Talbot effect, does not require a transversely coherent particle beam and therefore provides a superior signal count and improves the interference fringe contrast. Additionally, other matter-wave interferometers have used only optical gratings, either single [12, 13] or multiple gratings [14], produced by standing light waves. In all these cases the source was either an atomic beam created via a pressure differential or a molecular thermal beam, both of which produce velocities typically in the region of 100-1000 ms^{-1}. Faster velocities produce shorter de Broglie wavelengths, which therefore require greater distances between the grating and detector in order to resolve the interference fringes.

Successfully resolving matter-wave interference fringes from a transmission grating requires having enough distance between the grating and detector such that the fringes separate further than the resolution of the detector. If the distance isn't sufficiently long, the fringe separation can also be increased by using slower (colder) atoms to increase the de Broglie wavelength. Here at UCL, a cold atom source in the form of a metastable argon magneto-optical trap (MOT) was available for this application. This MOT uses lasers and magnetic fields to cool the atoms to temperatures as low as 100 μk. Such a trap has been demonstrated as a source for matter-wave interferometry in 1992 by Shimizu et al., who used a neon MOT [15]. To obtain the slowest possible velocity to the detector, the atoms were released from the trap by pumping the atoms to a magnetically neutral state causing them to simply fall out of the trap and accelerate towards the detector under gravity alone. This created a very slow longitudinal velocity, which meant the interference fringes were separated by 227 μm after falling 113 mm from double slit with a centre-to-centre separation of 6 μm. This MOT release method also produced a wide transverse velocity spread, meaning very few of the atoms in the trap would arrive at the detector.

A better signal intensity can be achieved by introducing an additional laser interaction in the form of a vertical push beam. The beam imparts an optical force on the atoms which pushes them out of the trap towards the detector. By manipulating the interaction strength, either through pulse length or beam power, the radiation pressure can be controlled and the atomic beam velocity can be selected. This has been previously demonstrated with metastable argon atoms in a velocity-tunable, pulsed, cold atom beam [16]. This method was developed further by exchanging the pulsed nature of the beam for a continuous cold atom source. This beam was generated by a column of unbalanced radiation pressure within MOT of rubidium atoms [17]. The atoms in the MOT were continuously replenished as other atoms were continuously pushed out.

This review, shows that one of the main components of this PhD project, the multi-slit, matter-wave interferometer, has a very well established experimental history. This makes it a sensible choice for developing a method to measure the atomic transverse momentum.

1.2 Weak measurements

Consider a quantum state described by a wavefunction, ψ_i, comprised of single observable states, $\hat{A}_s$, and a measuring device with a pointer. The pointer has a position x_p and momentum operator $\hat{P}_p$. When the measuring device interacts with the quantum state, the observable becomes coupled to the pointer through an interaction of strength $g(t)$. The interaction Hamiltonian for such a measurement, $\hat{H}_i = g(t)\hat{A}_s\hat{P}_p$, was given by von Neumann.

A typical quantum measurement, referred to here as a strong measurement or von Neumann measurement, can reveal the value of an observable, A_s. When the coupling is strong the pointer imparts a large back action on the system and collapses the wavefunction, producing an expectation value of A_s,

$$\langle A \rangle = \langle \psi_f | A | \psi_i \rangle. \tag{1.1}$$

Conversely, a 'weak measurement' can be made when the observable is very weakly coupled with the measuring device via $g(t)$. In this case, the pointer is only slightly perturbed by the quantum system such that the corresponding back action to the observable is reduced. This avoids collapsing the system's wavefunction at the cost of a greater uncertainty in the measured value, as a result this single measurement event does not contain enough useful information to observe a state. However, repeating the measurement many times and averaging the results can reveal a 'weak value' for the observable.

This form of weak measurement was introduced in 1988 by Aharonov, Albert and Vaidman(AAV) [18] where the weak measurement was outlined in the context of a Stern-Gerlach (SG) spin measurement apparatus. The limit for which a measurement can be considered weak, is given as the range for which the interaction $\exp(iH_I \int dt)$ is approximately equal to the first order of it's Taylor expansion. The quantum system is pre-selected in the state $|\phi_i\rangle$ and post-selected in the state $\langle \phi_f|$, the weak approximation reveals a 'weak value'

$\langle A_w \rangle$ of the observable, A, defined by

$$\langle A_w \rangle = \frac{\langle \psi_f | A | \psi_i \rangle}{\langle \psi_f | \psi_i \rangle}, \tag{1.2}$$

where $\langle A_w \rangle$ is a complex number, but is not an eigenvalue like equation 1.1. The denominator in equation 1.2, highlights how post selecting a particular state can lead to amplification effects. As $|\psi_i\rangle$ and $\langle \psi_f|$ approach orthogonality, the value of A_w can lie outside the range of possible eigenvalues of A. This was initially described in AAV's paper [18] and was later demonstrated experimentally where the amplification allows a higher level of precision measurement than was previously achievable. For example, measurements of frequency [19], angle [20] and velocity [21] all used AAV's weak measurement. More specifically, in 2009, weak measurements were used to measure a laser beam deflection of 400 femto-rad [22] in a Sangac interferometer.

The non-perturbative nature of weak values have also been used to further probe traditional quantum theories, such as introducing a 'which way' measurement in a double slit interferometer [23], albeit only in theory. Experiments did follow [24], including demonstrations of Hardy's paradox using photons [25, 26], the three box problem [27] and a violation of Bell's inequality in time [28].

A weak measurement is essentially an application of an indirect measurement scheme to the von Neumann measurement protocol [29], which in practice process contains 2 stages, a 'weak stage' followed by a strong measurement also called a 'post-selection' stage. The weak stage is a weak coupling of the observable to the pointer, a different property of the system. This weak interaction does not perturb the system enough to collapse the quantum state. This is followed by a strong measurement of the system revealing a shift of the pointer corresponding to a 'weak value' of the observable. It is only when the interaction is weak as defined by Aharonov, that the observable can be amplified. This process used to measure transverse momentum of photons in a double slit interferometer by coupling the momentum of the photon to a phase shift in its polarisation as it passed through a calcite crystal. This was achieved in 2012 by Kocsis et al. [30]. This experiment provided the framework to design a new experiment which measures the transverse momentum of an atom in a matter-wave interferometer, where the phase shift in the atom's spin is induced by a magnetic field.

In the experiment by Kocsis et al., single photons from a quantum dot pass through a double slit setup and gain transverse momentum via diffraction. In between the slits and the interference pattern on the 2D detector, the photons pass through a set of wave-plates and a tilted birefringent crystal, which together act as a polarisation interferometer. The crystal shifts the phase of the horizontal and vertical components of the photon's polarisation by a different amount, dependent on the time spent in the birefringent crystal. The crystals optical axis is tilted such that the time spent within the crystal is dependent on the photon's transverse momentum. Therefore, the phase shift in the polarisation becomes the shift of the transverse momentum pointer via a weak coupling. The photons then continue towards the detector preserving their acquired phase shift. When the photons reach the detector, the phase shift acquired during the polarisation interferometer is observed as interference in the signal intensity. From this, a 'weak value' of the photon's transverse momentum is determined at specific transverse positions. Repeating this measurement at different longitudinal positions between the slits and the detector allowed them to reconstruct what they called the photons' 'average trajectories'.

It is interesting that the trajectories measured by Kocsis compare well with those calculated by Philippidis et al. [3], using the de Broglie-Bohm approach [2] as shown in figure 1.1(b). Bohm (and hence Philippidis) links the phase of the wavefunction to the local momentum ($p = \nabla S$). The 'kinks' in the trajectories, due to a 'quantum potential', are not brought into con-

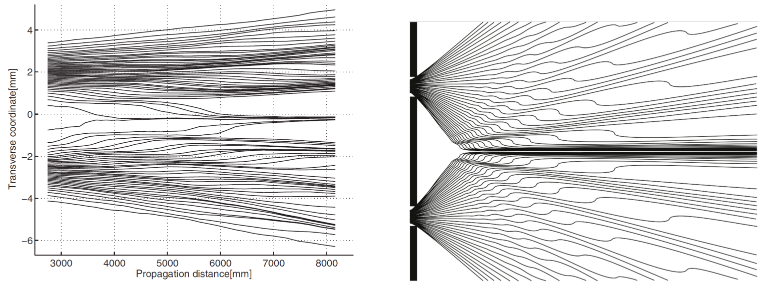

(a) (b)

Figure 1.1: (a) The ‘trajectories’ reconstructed by Kocsis et al. from observing the weak value of the photon’s transverse momenta (b) The trajectories of particles passing through double slits as predicted by the de Broglie-Bohm theory

sideration by the Copenhagen interpretation. The trajectories calculated by Philippidis et al. were for particles which have a localised mass and which follow the Schrödinger equation. However, Kocsis used single photons, which are excitations of the Maxwell field, so the simulations don’t necessarily apply to photons. To truly test the theory, we need to use particles with a finite rest mass. Additionally, Kocsis et al.’s use of the word ‘trajectories’ has been contested by Hiley et al., who replace the word with ‘average momentum, flow lines’, since a Bohm ‘trajectory’ is the average of an ensemble of actual individual stochastic Feynman paths [31].

Furthermore, Kocsis’s does not make it clear if his experiment can be considered ‘weak’, as defined by Aharonov, as opposed to simply being an indirect measurement as described by Svensson [29]. Recall the measurement Hamiltonian, $\hat{H}_i = g(t)\hat{A}_s\hat{P}_p$, used in the unitary time evolution operator $\exp\{i\hat{H}_i t/\hbar\}$. Kocsis states that for the photon’s weak interaction with the birefringent crystal, the observable $\hat{A}_s$ is the photon’s transverse momentum, $\hat{k}_x$ and the pointer $\hat{P}_p$ is the photon’s polarisation, $\hat{S}$. Kocsis then describes the interaction Hamiltonian as $\hat{H}_i = g\hat{k}_x\hat{S}$ (detailed in the paper’s supporting online material), however Kocsis does not explain how this can be constructed using the underlying physics of the photon-crystal interaction.

The interaction coupling strength is given as g and the interaction time, t, is introduced via the the time evolution operator. However, looking at the experiment geometry it is clear that t should be part of the coupling strength between $\hat{k}_x$ and $\hat{S}$ in Kocsis's $\hat{H}_i$. This Hamiltonian provided by Kocsis appears to describe the whole process of the photon's phase shift measurement. However, it is used in the time evolution operator as though it is describing just the interaction involved in the refraction of the photons as they enter the crystal. The observed phase shift in the polarisation is a function of t and the crystal's refractive index. If the crystal properties are known, $\hat{k}_x$ can be inferred from t. This makes it difficult to put $\hat{k}_x$ into the weak measurement formalism since observing the phase is a measurement of t, which is not a quantum operator. The resulting weak value is given as $\langle x_f|\hat{k}_x|\psi\rangle/\langle x_f|\psi\rangle$, where the photon's final position, x_f, acts on the spatial wavefunction of the photon ψ. If we apply the idea of amplification to this 'weak value' it does not provide the same amplification design as previous weak value amplification experiments.

Despite these gaps in ideas, it is still true that the phase shift in the optical wave is coupled to the transverse momentum which provides the justification for this project to measure the atomic transverse momentum in a matter-wave interferometer. Weak measurements have highlighted a pathway for Kocsis, and hence our experiment, to study fundamental quantum mechanics. The definition of 'weak' as described by Aharonov does not apply, but there are many other reasons why the measurement could be described as weak.

Aside from being compared with the 'Bohm momentum', the local momentum has been interpreted in a number of ways, as examined by Berry [32]. Berry discusses different possible meanings of the local momentum of a wavefunction stating that "each have equivalent formulas, but give insight into different underlying physics". The local momentum in a matter-wave interferometer has not been measured for atomic systems before, however weak measurements with atoms have been shown to work with various coupling schemes. This thesis aims to make a weak measurement of momentum using an atomic system that can be compared to the experiment and interpretation of the work of Kocsis.

1.3 Spin-state interferometry

To create a weak measurement of an atomic observable, one must consider what degrees of freedom are available to act as a pointer that can weakly couple to the observable. This consideration must also include the ways in which one can interact with the atom and its degrees of freedom. Typically, atomic weak measurements use the internal degrees of freedom of the atom. These are the spin states, which are the projections of the atom's spin magnetic moment and can interact with optical and magnetic fields.

Denkmayer et al. [33] utilised the spin of a neutron to weakly measure the position in a neutron interferometer, in doing so they appeared to demonstrate the spin separating from the centre-of-mass of the neutron. Rubidium atoms were combined with photon properties in a number of other experiments. For example, the frequency distribution of the emission from rubidium atoms was coupled with the spin polarisation of the atom, so the distribution acts as a pointer for the spin in a new magnetometry technique [34]. The populations of the states in two energy levels of a rubidium atom were weakly measured by coupling the populations to the spin of the atoms, which was then optically measured. The measurement was used as a feedback control to help reduce decoherence of the two level superposition state [35]. Another optical probe beam was used to weakly measure the average spin rotation of a caesium atom ensemble by monitoring the polarisation rotation of the probe beam. This allowed a continuous weak measurement of the ensemble average spin [36].

The atoms used in this experiment's matter-wave interferometer are cold argon atoms in an excited metastable state[1]. The $4s[3/2]_2$ metastable state,

[1]Note: this thesis uses the jl coupling notation, $nl[K]_J$ where n is the principal number of the valence electron, l is the orbital angular momentum of the valence electron, J is the total angular momentum and K is the sum of the total angular momentum of the atomic

that is used to cool and trap metastable argon atoms, is in a $J = 2$ spin state and can be manipulated with a magnetic field via the state's five magnetic sublevels. Additionally, state-to-state transitions can be stimulated via at least two commercially available laser diode wavelengths, at 801nm and 811nm. As discussed, the atomic spin has been used as a pointer for weak measurements. The magnetic degrees of freedom of the multiple magnetic spin states (m states) and the accessibility of the 4s$[3/2]_2$ transitions, provide coupling to the transverse momentum via time spent in magnetic fields and the Zeeman effect.

The spin states of metastable argon travelling through a magnetic field have been previously used to produce a longitudinal Stern-Gerlach interferometer (LSGI). One group based at Universite Paris-Nord showed that Stern-Gerlach splitting from a gradient in the direction of the travelling argon atoms can be used to create an interferometer [37]. The signal modulation due to the interference is m state dependent, so while there is a superposition of m states the phase shift is only observable if the signal intensity from a single m state is measured. Such a scheme was tested using lasers at 811 nm and 801 nm to pre-select and post-select the spin states, respectively, of a supersonic metastable argon beam. The superposition of m states was achieved by a fast rotation of the magnetic field surrounding the atom, as a result of the atom quickly travelling from a region of one magnetic field direction into another. This experiment effectively couples the momentum of the atoms to the phase shift acquired in the magnetic field strength. The phase shift reflects changes in the magnetic field. We develop this design by keeping the magnetic field constant and instead creating a momentum dependent, interaction time.

---

core and l

1.4 Thesis overview

Chapter 2

This chapter contains a full theoretical and technical description of each component of the experiment to weakly measure the transverse momentum of an atom in a matter-wave interferometer. This includes the wavefunction in a matter-wave interferometer, the phase of the spin states of an atom in a Stern-Gerlach interferometer and how the phase is used to measure the transverse momentum.

Chapter 3

A velocity-tuneable, cold metastable argon beam is constructed and characterised. The magneto-optical trap, which acts as the beam source, is also described.

Chapter 4

Matter-wave interferometry using a Si_3Ni_4 multi-slit grating is demonstrated using the atomic beam described in the previous chapter. The resulting interference pattern is used to measure the average beam velocity and the Van der Waals potential between the atom and the grating.

Chapter 5

A measurement of the phase shift in the wavefunction of metastable argon atoms, in a longitudinal Stern-Gerlach interferometer, is presented. Using the atomic beam described in chapter 2, the observed phase shift is used to measure the magnetic field strength of the interferometer

Chapter 6

This chapter describes how a weak measurement of transverse momentum of an atom in a matter-wave interferometer could be made. The experiments from the previous two chapters are combined in a first prototype design. Results from this measurement are the ultimate goal of the research group

Chapter 7

This chapter consists of the conclusions summarising the experiments undertaken and exploring the future development of the project.

Chapter 2

Measurement of the atomic transverse momentum in a matter-wave interferometer

This chapter describes how a weak measurement of the transverse momentum of a metastable argon atom can be made in a matter-wave interferometer, using a spin-state interferometer.

I begin by describing an atomic, multi-slit, matter-wave interferometer, before outlining spin-state interferometry in a longitudinal Stern-Gerlach interferometer (LSGI). Here, the phase shift between the atom's spin states, due to the interaction with the magnetic field of the interferometer, is discussed. Finally, I describe how a modified LSGI can be used to measure the transverse momentum.

2.1 An atom in a matter-wave interferometer

Consider atoms within a MOT (magneto-optical trap) that are accelerated towards a position detector, by external radiation pressure, to create a cold atomic beam. By inserting a mask (material or optical), in the path of the beam, certain paths between the trap and the detector are prohibited. If the mask contains periodic, narrow openings, then the atoms will diffract and create a interference fringes on the detector. We initially consider the wavefunction of a free particle and quantum mechanically model the probability density of the atom's position as it propagates through the mask and towards the detector [38]. This provides a guide for the design of the experiment and also provides a model with which to simulate the transverse momentum.

2.1.1 Wavefunction of the atom

The atomic wavefunction is formulated using the Feynman path integral technique [39]. In this method, all the possible paths between two points α and β are summed to give the probability of finding a particle at a particular point. The sum of all these paths is called the kernel or propagator, K. The propagator is defined using the classical Langrangian

$$K(\beta, t_\beta, \alpha, t_\alpha) = \exp[\frac{i}{\hbar}\int_{t_\alpha}^{t_\beta} m\frac{\dot{x}^2}{2} + m\frac{\dot{z}^2}{2} + mgz\ dt] \tag{2.1}$$

which for an atom of mass m that begins at x_0, t_0 and is found at x_f, t_f, is given as

$$K_x(x_f, t_f, x_0, t_0) = \left(\frac{m}{2\,i\,\pi\,\hbar(t_f - t_0)}\right)^{\frac{1}{2}} e^{\frac{i\,m}{\hbar}\frac{(x_f - x_0)^2}{2\,(t_f - t_0)}}. \tag{2.2}$$

It is sufficient to model these paths in only the x and z plane as shown in figure 2.1. If the double slits are oriented such that the long edge is in the y plane, the atoms will not produce any interference in the y plane. For a set of points, S, where the wavefunction does not vanish, the wavefunction is then calculated by

$$\psi(x_f, t_f) = \int_{x_0, z_0 \in S} K(x_f, t_f, x_0, t_0)\psi_0(x, z)\, dx_0 dz_0, \tag{2.3}$$

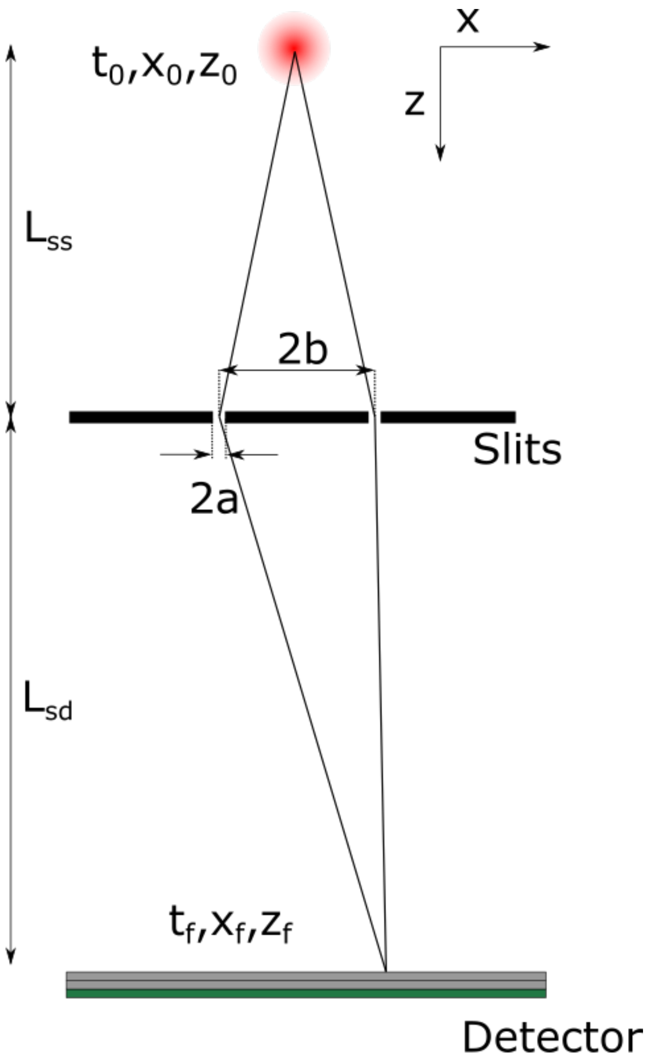

Figure 2.1: Two paths, out of the many possible paths, between the source and the detector. At the source, $x_0 = z_0 = t_0 = 0$, L_{ss} is the distance between the source and the slits, L_{sd} is the distance between the slits and the detector, $2a$ is the slit width, $2b$ is the slit separation, $z_f = L_{ss} + L_{sd}$ and x_f is the final position of the atom on the detector.

where $\psi_0(x, z)$ is the wavefunction at t_0, or the wavefunction at the source defined by

$$\psi_0(x, z) = (2\pi\sigma_x^2)^{-\frac{1}{4}} e^{-\frac{x^2}{4\sigma_x^2}} e^{ik_{0x}x} \left(2\pi\sigma_z^2\right)^{-\frac{1}{4}} e^{-\frac{z^2}{4\sigma_z^2}} e^{ik_{0z}z}. \tag{2.4}$$

This quantum description of the atoms simplifies the MOT by using the statistical variation of atomic positions and velocities as the probabilities of a pure state. The simplification is sufficient for a description of the experimental concept. For more accurate predictions a density matrix would be more appropriate. For this initial wave packet, we assume the wavefunction is Gaussian with the initial standard deviation in position, $\sigma_{x,y,z}$, $\sigma_0 = 10\,\mu\text{m}$. These values can be adjusted depending on the actual source size in the experiment. The initial wave vector is $k_0 = \frac{mv}{\hbar}$, which we choose using the RMS velocity of the atoms in the MOT. Also $\sigma_{k_x} = \sigma_{k_y} = \sigma_{k_z} = \frac{m\sigma_v}{\hbar}$ and $\sigma_k = \frac{m\sigma_v}{\sqrt{3}\hbar}$, where $\sigma_v = \sqrt{K_b T/m}$, K_b is the Boltzman constant and T the MOT temperature.

If the atoms are moving fast enough towards the slits due to an external force, the atom's movement in the z direction is dominated by this force rather than the expansion of the wavepacket, so this motion can be modelled classically. This gives a wavefunction, with only x and t as a variables where equation 2.3 becomes

$$\psi_x(x,t,k_{0x}) = (2\pi s_0^2(t))^{-1/4} \exp[-\frac{(x - v_{0x}t)^2}{4\sigma_0 s_0(t)} + ik_{0x}(x - v_{0x}t)] \tag{2.5}$$

with $s_0 = \sigma_0\big(1 + \frac{i\hbar t}{2m\sigma_0^2}\big)$.

A realistic calculation for the probability density should include the spread of initial transverse momentum, i.e. a sum of all momentum values, k. We therefore write the probability density, ρ, as

$$\begin{aligned} \rho(x,t) &= \int_{-\infty}^{\infty} (2\pi\tau^2)^{1/2} e^{-k_x^2/2\tau} |\psi_x(x,t,k_x)|^2 \, dk_x \\ &= (2\pi\varepsilon_0^2(t))^{-1/2} \exp[-\frac{x^2}{2\varepsilon_0^2(t)}] \end{aligned} \tag{2.6}$$

where

$$\tau = \frac{2m\sigma_0^2}{\hbar}, \tag{2.7}$$

$$\varepsilon_0^2(t) = \sigma_0^2(t) + \big(\frac{\hbar t \sigma_k}{m}\big)^2, \tag{2.8}$$

$$\sigma_0^2(t) = \sigma_0^2 + \frac{\hbar t}{2m\sigma_0}^2. \tag{2.9}$$

This formalism is a sufficient description for the free propagation of the wavefunction for atoms leaving a MOT. To model the diffraction from a slit pair, we consider all the possible paths that an atom may take to reach the detector via the slits. For this we use the same kernel (equation 2.2), but using the positions across the slit width as the atoms' initial positions, x_0 and equation 2.5 as the starting wavefunction.

The wavefunction after transmission through one slit is

$$\psi_s = \int_{b-a}^{b+a} K_x(x, t, x_g, t_g)\psi_x(x, t_g, k_x)\, dx_a \tag{2.10}$$

where the subscript 'g' indicates the value of the component at the grating or double slits. This can be extended to include any number of slits, by simply adding the wavefunctions with x_a adjusted to describe the position of each additional slit. Here, $2b$, is the slit separation and $2a$ is the slit width. Throughout this chapter, the simulation is simplified by describing the atom's propagation through a double slit, rather than a multi-slit grating.

We use equation 2.10 to calculate the probability density for a two slit configuration, where $b = -128\,\text{nm}$ or $128\,\text{nm}$ for the left and right slit respectively, $a = 45\,\text{nm}$ and the atom velocity is $51\,\text{ms}^{-1}$. From this we observe the separation and intensities of the interference fringes as shown in figure.2.2.

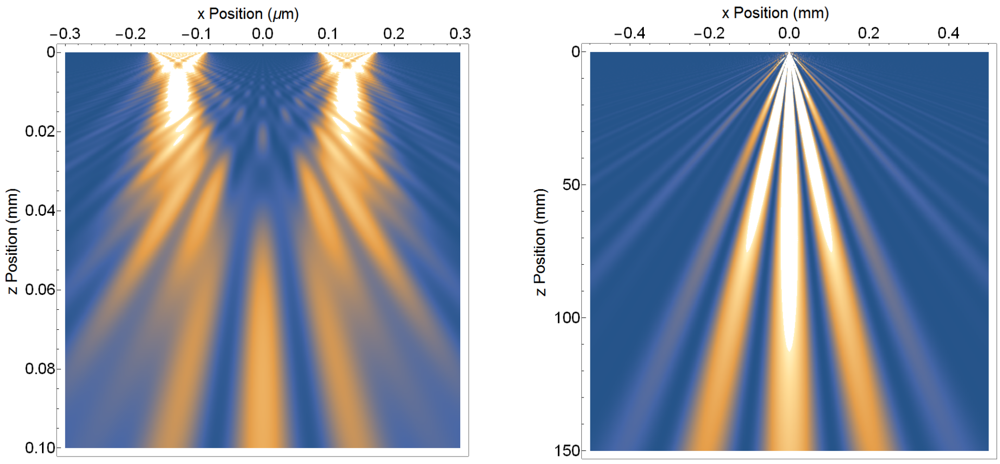

(a) (b)

Figure 2.2: The calculated probability density for atoms emerging from double slits. The grating is positioned 76 mm below the MOT (0 mm). The probability density is given in the (a) near field, 0.1 mm after the slits and (b) the far field, 150 mm after the slits.

A fringe spacing of approximately 200 μm is given by the far field trajectory plot at a distance of 150 mm below the slits. Measuring the fringe spacing allows us to assess the suitability of our detector resolution. For example, for a detector resolution of 20 μm, at 150 mm below the slits, there would be approximately 10 pixels per fringe. Assuming that 2 fringes could be resolved by a minimum of 3 pixels, then fringes as close as 40 mm below the slits, could be observed with the detector. Details on the available detector resolution are covered in section 3.4.

This data not only allows us to confirm the shape and size of the expected interference pattern at various detector positions, but also allows us to accurately determine the atom's spatial distribution while passing though the weak measurement stage. This is the first step in modelling the atom's transverse momentum, which is outlined in section 2.3.

2.1.2 Coherence

The model outlined above is useful for estimating the fringe separation and is necessary to determine the atomic transverse momentum. However, there were some discrepancies when attempting to use the calculated wavefunction to compare with the experimental results of the matter-wave interferometer. The model does not take into account the full spread of the initial longitudinal and transverse velocities and when attempting to do so, revealed some limitations in available computing power. The velocity distributions in the x and z axes contribute to the incoherence of the atomic beam and reduce the contrast of the interference fringes in different ways. An analogy with optics was used to understand the coherence of the atomic beam, with many of the equations taken from [40], which also models a double slit configuration.

Longitudinal Coherence

In matter-wave interferometry the longitudinal coherence, also referred to as the temporal coherence, is a measure of the phase shift, between two points separated longitudinally. For the atomic beam, this can also be viewed as two points in time on the detector. The distance of each fringe from the central axis is $nL\frac{\lambda}{2b}$, where n is the order of the fringe. Considering that the de Broglie wavelength of the atom, λ, is inversely proportional to the velocity, one can see that a distribution of velocity will result in a distribution in the fringe spacings, which increases the width of fringes by proportionally greater amounts for higher order fringes. Figures 2.3 show the effect of this distribution.

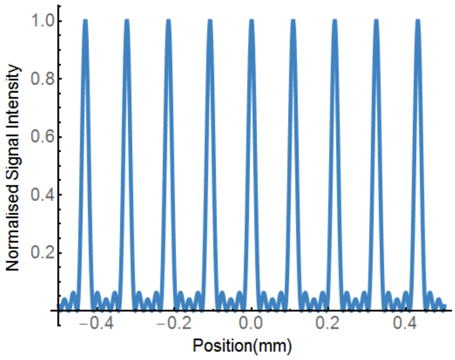

(a)

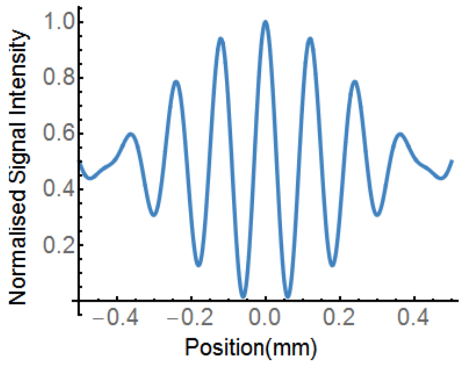

(b)

Figure 2.3: (a) An interference pattern calculated from 5 grating slits for atoms travelling at 55 m.s^{-1}, i.e. 0 ms^{-1} longitudinal velocity distribution (b) the same setup but with the average of 3 velocity contributions 51, 46 and 41 ms^{-1}.

To achieve enough longitudinal coherence to ensure visible interference fringes, the difference in path lengths between adjacent fringes should be less than the longitudinal coherence length given by

$$l_{lc} = \frac{\lambda_0^2}{\Delta\lambda}. \tag{2.11}$$

In this project the central path length l_0 (the 0th order fringe) is 0.1559 m. This is the shortest possible path between the grating and the detector. The fringe separation for a velocity of 51 ms^{-1} is 107 µm. So the difference in path length between the 0th and 1st order, is 3.8×10^{-8}m. We need this value to be less than the longitudinal coherence length in order to observe well resolved higher order fringes. In equation 2.11, if we replace the 'l_{lc} =' with '3.8×10^{-8} <' and rearrange to solve for Δv using $\lambda = h/mv$, we can deduce an upper limit for the longitudinal velocity distribution in order to achieve sufficient longitudinal coherence. For an average velocity of $51\,\mathrm{ms}^{-1}$, the difference in path length for the first order fringe would become greater than the longitudinal coherence length when Δv is greater than $0.25\,\mathrm{ms}^{-1}$

Experimentally, the spread in longitudinal velocities can be attributed to the initial temperature of the atoms in the MOT and the force that accelerates the atoms towards the detector (either by gravity or by radiation pressure from a push beam laser). This is discussed in more detail in section 3. Typically, the temperature of the MOT is of the order of $100\,\mu\mathrm{K}$ with a standard deviation of $20\,\mu\mathrm{K}$. Using the Maxwell-Boltzmann particle velocity distribution and looking at the mean of the magnitude of the temperature of the atoms, $v = \sqrt{8k_bT/m\pi}$ gives a velocity of $0.5 \pm 0.1\,\mathrm{ms}^{-1}$. The typical atomic beam velocities achieved using the push beam are between 1 and $50\,\mathrm{ms}^{-1}$, so it is clear that for higher velocities, the spread in velocities due to temperature is dwarfed by the total velocity, therefore the velocity distribution will be predominantly due to the interaction with the push beam, as described in section 3.6.

Transverse Coherence

We can define the transverse coherence in a similar way to the longitudinal coherence; the phase difference between two points separated along the x axis, perpendicular to the atomic beam direction. Again, as with longitudinal coherence, the interference fringe contrast is reduced by a lack of transverse coherence. For an atomic beam, the transverse coherence depends upon the distribution of the initial positions and transverse velocities of atoms that reach the detector.

To analyse this, we again look at the differences in optical path lengths caused by a variation in the transverse velocities or starting positions. If the atoms in the source had identical transverse (and longitudinal) velocities, the path length between anywhere transversely across the source and wherever the atoms arrive on the grating would always be approximately the same. This distribution of transverse velocities can arise due to the nature of the source, for example due to temperature distribution or scattering as it is not a point source as shown in figure 2.4(a)

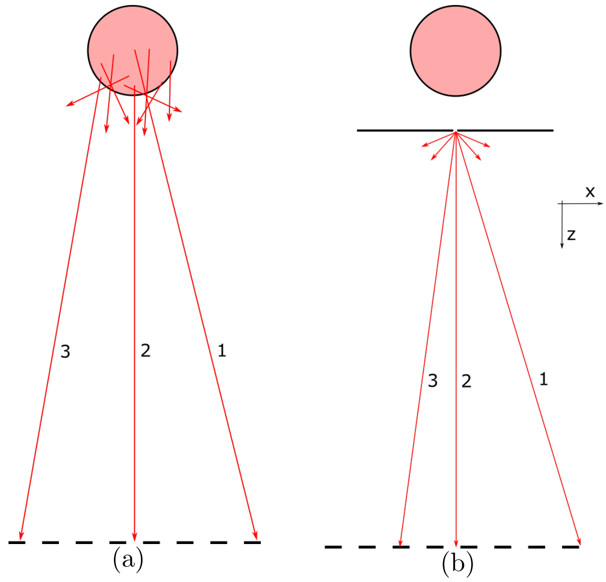

Figure 2.4: (a) Some of the possible path lengths to the grating from a thermal source (b) The same thermal source, set behind a slit or pinhole. There is still a difference in possible path lengths, i.e. 1 and 3, but there will be a central region where the differences are negligible.

The source size may be neglected from coherence calculations if there is zero or very low distribution in transverse velocity. If this does not naturally arise from the properties of the source, restricting the starting positions and selecting only a narrow band of transverse velocities will improve coherence by creating a central region where the path length variation is small as shown in figure 2.4(b). In this case we can consider the transverse distance, over which the path lengths are approximately equal, as the transverse coherence length. Another way to approach transverse coherence when the source is masked by a slit or pinhole, is to consider that the width of the aperture will determine the curvature of the wavefront incident on the grating due to diffraction, which in turn determines the transverse coherence. Figure 2.5 shows how a curved wave front causes the diffracted wavefunction to be transmitted through the grating slits at slightly different times (the wavefront passing x_1 will do so slightly after it passes x_2).

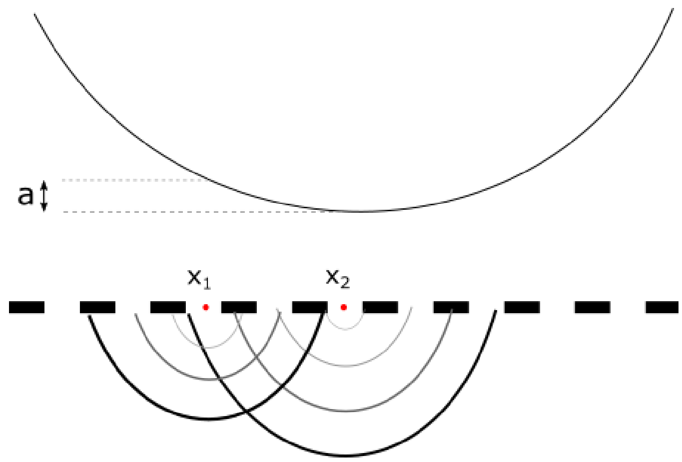

Figure 2.5: Example showing how the curvature of a diffracted wavefront approaching the grating causes a phase shift between points across the grating. This shifts the location at which constructive interference occurs and smears out the overall fringe pattern.

An expression for the transverse coherence length can be derived [13] and is given by

$$l_{trans} = \frac{\lambda}{2\alpha} \tag{2.12}$$

where α is the angle that the source subtends from the grating. To describe the contrast of the interference signal, we talk about the 'degree of spatial coherence'

The spatial coherence as a function of the source size, is a slowly changing value so there is no a clear boundary between a coherent and incoherent source. The contrast of the interference fringes can be used to derive an expression for the degree of spatial coherence, γ_{12}, between two points (1 and 2) on a transverse plane for a double slit interferometer [40] and is given by

$$\gamma_{12} = \text{sinc}\left[\frac{a_{12}\pi w_s}{L_{sg}\lambda_{DB}}\right]. \tag{2.13}$$

Here a_{12} is the separation of two points on the grating over which to determine the degree of spatial coherence. Here the width of the source is given by w_s and the source to grating distance is L_{sg}. The degree of coherence, given by the value of γ_{12}, is described as

$$
\begin{aligned}
|\gamma_{12}| &= 1 \text{ coherent limit} \\
|\gamma_{12}| &= 0 \text{ incoherent limit} \\
1 > |\gamma_{12}| &> 0 \text{ partial Coherence}
\end{aligned}
\tag{2.14}
$$

where $|\gamma_{12}| = 1$ would give 100% contrast in the interference pattern and $|\gamma_{12}| = 0$ would give 0% contrast.

Using this to analyse the coherence in our atomic beam, we need to choose two relevant points on the grating between which to determine the degree of coherence. A collimation slit, positioned immediately above/before the grating, sets the width of the beam when it arrives at the grating, so a_{12} is approximately the width of this collimation slit, w_{s2}. In our case is $w_{s2} = 50\,\mu\text{m}$. For example, if we have a source width of $10\,\mu\text{m}$ with atoms travelling at $50\,\text{ms}^{-1}$, then $\gamma_{12} = 0.13$. This suggests the fringe contrast will be very low, but could still be sufficient to observe and analyse the interference fringes.

2.2 Spin-state interferometer

The weak measurement of an atom's transverse momentum requires its momentum to be coupled to another observable quantity of the atom. This experiment uses metastable argon atoms whose internal magnetic spin states can be manipulated by a weak magnetic field that does not significantly perturb the momentum of the atom. The magnetic field induces a phase shift in the wavefunction describing the atomic spin state and can be arranged such that the interaction between the field and the atom is dependent on the atoms transverse momentum. We can observe this phase shift using a longitudinal Stern-Gerlach interferometer (LSGI).

Initially we test the LSGI in a configuration that does not make the phase sensitive to the atom's transverse momentum. An atomic beam is prepared in a spin polarised state and the atoms are then put into a linear superposition of spin states using a spin-flipper. While in a superposition of spin states, the atoms are exposed to a magnetic field which induces a spin-state dependent phase shift of the atom's wave function. The phase shift is also dependent on the interaction time and the magnetic field strength. Another spin-flip builds a new coherent superposition which combines the spin states and allows the phase shift to be measured as interference in the spin-state population probability density [37]. A schematic diagram of this process is given in figure 2.6.

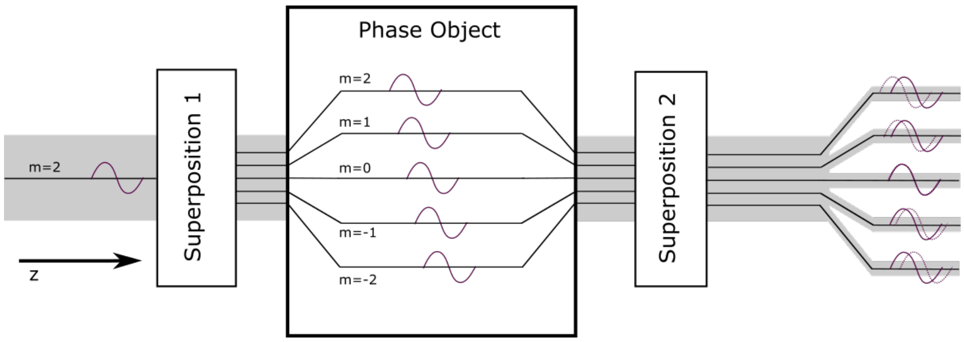

Figure 2.6: A schematic of the stages of an LSGI for an atom in a metastable state with five Zeeman sublevels m. When the individual m states are individually observed, the interference appears as modulations in the intensity of the signal.

The LSGI only becomes coupled to the transverse momentum when we tilt the interferometer with respect to the the atomic beam. We describe how to create a transverse momentum dependent interaction time and this is detailed in the succeeding section, 2.3.

2.2.1 Superposition

Typically, a simple example of an interferometer will begin with a pure state being split into a linear superposition of two or more eigenstates. There are many examples of this; a polarising beam splitter for horizontally and vertically polarised photons or a double slit providing two paths for matter-waves. In this case, we use a superposition of the magnetic quantum states (m states) of the argon atom. For the $J = 2$ state, metastable argon has five magnetic substates ($m = 0, \pm 1, \pm 2$) which we use to create a superposition.

The superposition is achieved using a spin-flipper which re-projects the atom's quantisation axis via a non-adiabatic, spin-axis rotation. This re-projection is achieved, by rapidly rotating the atom's quantisation axis fast enough so the atomic spin, rotating about the external magnetic field direction at the Larmor frequency, does not adiabatically follow the rotating quantisation axis [37]. This transition causes a single state to be re-projected into a linear superposition of five states along a new axis. This quantisation axis rotation is achieved by rotating the external magnetic field.

The populations of each m state after the projection are defined by the angle of rotation θ_{rot} and can be calculated using the Wigner D matrix defined as $D^J(\phi, \theta_{rot}, \chi)$ where $J = 2$ for metastable argon and $\phi = \chi = 0$. An atom's initial state $|\Psi\rangle_i$ is described using a wavefunction which is separated into the spatial components ψ_{path} and spin components ψ_{spin}. Here, the spatial part is described as a plane wave with wavenumber k and the spin part is polarised in the substate $m = 2$. The total wavefunction can be represented by

$$\begin{aligned} |\Psi\rangle_i &= |\psi_{path}\rangle \otimes |\psi_{spin}\rangle \\ &= e^{ikz} \otimes |J = 2, m = 2\rangle \end{aligned} \tag{2.15}$$

where the Wigner matrix for a θ rotation is given in appendix A. For a rotation of $\theta_{rot} = \frac{\pi}{2}$, acting on the initial state $|\psi_{spin}\rangle_1 = |2\rangle$ the superposition state is described by

$$\begin{aligned} |\psi_{spin}\rangle_2 &= D^2(0, \tfrac{\pi}{2}, 0)|\psi_{spin}\rangle_1 \\ &= D^2(0, \tfrac{\pi}{2}, 0)|2\rangle \\ &= \left(\frac{1}{4}|-2\rangle - \frac{1}{2}|-1\rangle + \sqrt{\frac{3}{8}}|0\rangle - \frac{1}{2}|1\rangle + \frac{1}{4}|2\rangle\right). \end{aligned} \tag{2.16}$$

This spin flip projection is only achieved when the condition, $\omega_L \ll \omega_B$ is met.

The Larmor precession frequency is defined as

$$\omega_L = \frac{g_f \mu_B B}{\hbar} \tag{2.17}$$

where B is the magnetic field strength, g_f is the g-factor and μ_B is the Bohr magneton. ω_B is the velocity of the angular rotation between the initial and final quantisation axes and is given by

$$\omega_B = \frac{\theta_{rot}}{\Delta t_{rot}}. \tag{2.18}$$

If this spin-flip condition is fulfilled, the rotation of the atomic spin vector does not adiabatically follow the rotating external magnetic field and provides a superposition of the five m states based on the new quantization axis.

2.2.2 Phase shift

We induce the m state dependent phase shift of the atom's wavefunction using a weak magnetic field. The magnetic field shifts the potential energy of the atom via the Zeeman operator $\hat{V} = g_f \mu_B \hat{J} \cdot B$, where B is the magnetic field strength and $\hat{J}$ is the spin-state operator. If the magnetic field is weak enough such that V is very small compared with the kinetic energy E, we can invoke the WKB approximation. In this limit we can write the wave vector for the matter-wave as

$$k(z) = \left(\frac{2m}{\hbar^2} \left(E - V(z) \right) \right)^{1/2} \tag{2.19}$$

where z is the direction of propagation. The spatial wavefunction is then given by

$$\psi = e^{i \int_0^L k(z) dz}. \tag{2.20}$$

We can see that a change in V will result in a change in the phase via a modification to the wavenumber, k. The phase shift of the wavefunction, ϕ, can be written as

$$\Phi = \int_0^L (k(z) - k_0) dz \tag{2.21}$$

where $k_0 = mv/\hbar$ is the initial wave number. To calculate this equation, we express k_0 as a function of energy, which gives

$$\begin{aligned} k(z) - k_0 &= \frac{\sqrt{2mE}}{\hbar}\left(\left(1 - \frac{V(z)}{E}\right)^{1/2} - 1\right) \\ &\approx -\frac{mv}{\hbar}\frac{V(z)}{2E} \\ &= \frac{1}{\hbar v}V(z). \end{aligned} \tag{2.22}$$

To describe the potential energy $V(z)$ in more detail, consider that the magnetic field of the phase object gives rise to a m dependent phase shift in the Zeeman energy, $V(z) = mg_F\mu_B B(z)$ and therefore the phase in equation 2.20 is given by

$$\begin{aligned} m\phi &= \frac{1}{\hbar v}\int_0^L V(z)\, dz \\ &= \frac{1}{\hbar v}\int_0^L mg_f\mu_B B(z) dz \\ \Phi &= m\frac{g_f\mu_B}{\hbar}Bt_{ws}. \end{aligned} \tag{2.23}$$

This acquired phase for an atom's interaction with the magnetic field is factorisable and can be applied to each term in equation 2.16, to give the spin state of atom, after passing through the magnetic field as

$$|\psi_{spin}\rangle_3 = e^{-2i\phi}\frac{1}{4}|-2\rangle - e^{-i\phi}\frac{1}{2}|-1\rangle + \sqrt{\frac{3}{8}}|0\rangle - e^{i\phi}\frac{1}{2}|1\rangle + e^{2i\phi}\frac{1}{4}|2\rangle. \tag{2.24}$$

2.2.3 Interference

To measure the phase shift we interfere the m states to create interference fringes in the probability density of the m state populations, allowing a measurement of the phase shift. This second spin-flip re-projects the states as the quantization axis is rotated back to the original axis.

As before, the rotation must be abrupt, fulfilling $\omega_L \ll \omega_B$, such that the spin axis does not adiabatically follow the rotating quantisation axis and the new populations of each m state are again determined by the rotation angle and the Wigner matrix shown in section 2.2.1.

The full description of the final state is a 5 x 5 matrix. If we only choose to observe one m state, for example $m = 0$, it will combine the $|0\rangle$ components from each new projection and take elements vertically from the Wigner matrix to give a probability of

$$\begin{aligned}\langle 0|\psi_{spin}\rangle_4 &= \langle 0|D^2(0, -\tfrac{\pi}{2}, 0)|\psi_{spin}\rangle_3 \\ &= \frac{1}{4}\sqrt{\frac{3}{8}}e^{-2i\phi} - \frac{1}{4}\sqrt{\frac{3}{2}} + \frac{1}{4}\sqrt{\frac{3}{8}}e^{2i\phi} \\ &= \sqrt{\frac{3}{8}}\sin^2\phi(v_x).\end{aligned} \tag{2.25}$$

Expanding the exponential component into polar form, simplifying and squaring, we can express the probability density for an atom initially in $m = 2$, to pass through the LSGI and be in $m = 0$ at the detector as the intensity

$$I = |\langle 0|\psi_{spin}\rangle_4|^2 \tag{2.26}$$

By following these steps for any initial and final spin state, the generalised description for signal intensity, $I_{i,f}$, where i is the initial spin polarisation and f is the final spin polarisation is then

$$I_{i,f} = \sum_{m=-2}^{+2} \left| D^2(\theta_2)\, M_A\, D^2(\theta_1)\, M_P\, e^{mi\phi} \right|^2 \tag{2.27}$$

where M_P and M_A are the m states chosen for the initial polarisation and the final detection respectively. For the first and second rotation angles $\theta_1 = \theta_2 =$

$\frac{\pi}{2}$, this produces the following equations for the relative intensities

$$
\begin{aligned}
I_{2,0} = I_{-2,0} &= \left(\sqrt{\frac{3}{32}} + \sqrt{\frac{3}{32}}\cos[2\phi]\right)^2, \\
I_{2,2} = I_{-2,-2} &= \left(\frac{3}{8} - \frac{1}{2}\cos\phi + \frac{1}{8}\cos[2\phi]\right)^2, \\
I_{2,-2} = I_{-2,2} &= \left(\frac{3}{8} + \frac{1}{2}\cos\phi + \frac{1}{8}\cos[2\phi]\right)^2, \\
I_{2,1} = I_{-2,-1} &= \left(\frac{1}{2}\sin\phi + \frac{1}{4}\sin[2\phi]\right)^2.
\end{aligned}
\tag{2.28}
$$

We plot the changing probability of the $m = 0, 1, 2$ states as a function of the incrementally increasing interaction time in figure figure 2.7. The frequency of the oscillations is dependent upon the phase shift ϕ, so we show the effect of different values of the variables of ϕ, given as B and t. We assume that both spin-flip rotations have $\theta_{rot} = 90°$. Due to the experimental setup described in section 5.2, the second rotation angle should be opposite to the first, $\theta_1 = -\theta_2$. In such a case, we can take equation 2.27 and apply an initial polarisation of $m = 2$ and final m states of $m = 0, 1, 2$.

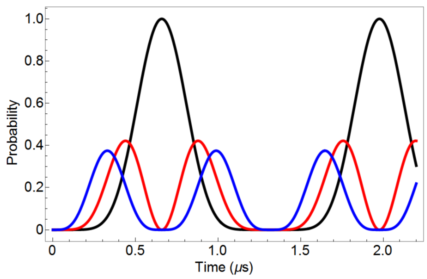

(a)

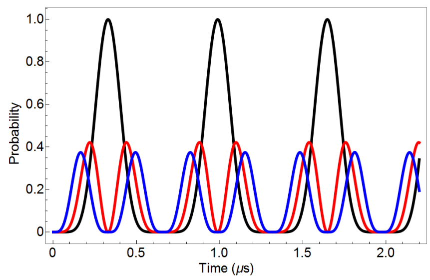

(b)

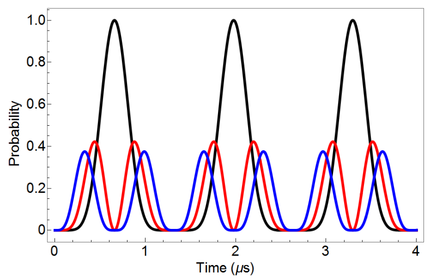

(c)

Figure 2.7: Visualising the phase, ϕ (equation 2.23) through the populations of the $m = 0$ state (black), $m = 1$ state (red) and $m = 2$ state (blue) from equation 2.28. The 3 plots show the change in the probability of the m state as a result of the phase shifts for different phase object interaction strengths, due to either an increase in B or t_{ws}. Here (a) $B(z) = 36\,\mu\mathrm{T}$ and $t_{ws} = 2\,\mu\mathrm{s}$, (b) $B(z) = 72\,\mu\mathrm{T}$ and $t_{ws} = 2\,\mu\mathrm{s}$, (c) $B(z) = 36\,\mu\mathrm{T}$ and $t_{ws} = 4\,\mu\mathrm{s}$.

Another variable we analyse is the rotation angle which should ideally be 90°. If we have a more acute or obtuse angle, the difference between the troughs and peaks changes, shown in figure 2.8.

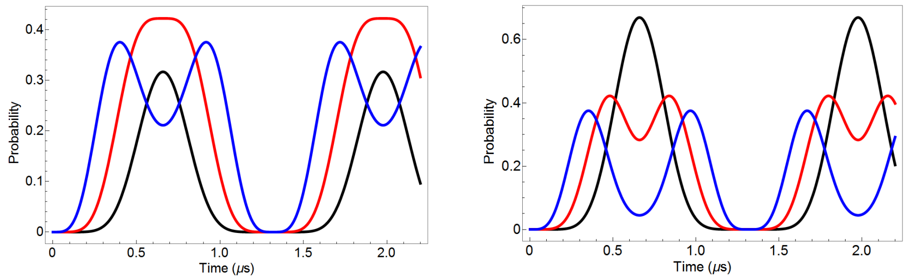

(a) (b)

Figure 2.8: Populations of the $m = 0$ state (black), $m = 1$ state (red) and $m = 2$ state (blue) for different spin-flip rotation angles. The same settings as plot 2.7(a), $B(z) = 36\,\mu\text{T}$ and $t_{ws} = 2\,\mu\text{s}$, but with (a) $\theta = \frac{\pi}{3}$ and (b) $\theta = \frac{2\pi}{5}$.

2.3 The 'weak' measurement

The model for the weak measurement follows the same general steps as the longitudinal Stern-Gerlach interferometer (LSGI) shown in section 2.2. The main difference is the time dependence of the phase shift ϕ is coupled with the transverse momentum of the atom. Firstly, this is achieved by using a permanent magnetic field for the phase object rather than a pulsed field. With a permanent field, the atom's interaction time is dependent on the velocity of the atom. Secondly, the field is tilted with respect to the transverse axis such that there is a different interaction time for atoms with different transverse velocities. In figure 2.9 we consider two trajectories that would arise from equal, but opposite transverse velocities, v_{x1} and v_{x2}.

2.3.1 Observing a transverse momentum dependent phase shift

Consider the same initial state that enters the standard LSGI, (equation 2.15), where the push beam spin polarises the atoms in the $|J = 2, m = 2\rangle$ spin state.

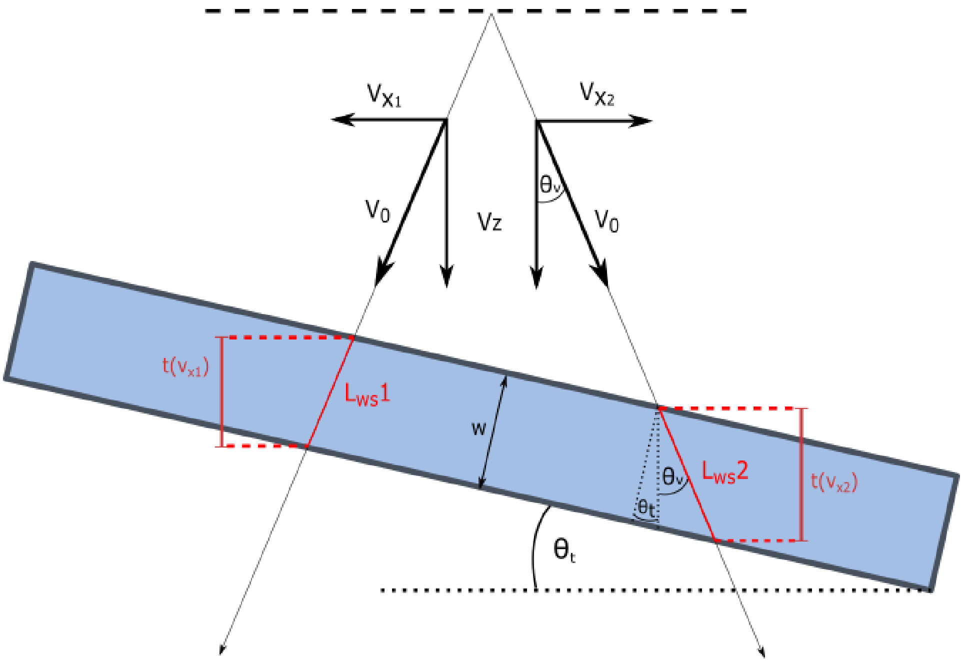

Figure 2.9: Schematic showing how different transverse velocities (v_x) result in different interaction times, $t_{ws}(v_x)$, due to the magnetic field tilted by θ_t.

The same m state superposition is created,

$$\begin{aligned}|\Psi\rangle_i &= |\psi_{path}\rangle \otimes |\psi_{spin}\rangle \\ |\Psi\rangle_2 &= |\psi_{path}\rangle \otimes D^2\left(\tfrac{\pi}{2}\right)|2\rangle \\ &= |\psi_{path}\rangle \otimes \left(\frac{1}{4}|-2\rangle - \frac{1}{2}|-1\rangle + \sqrt{\frac{3}{8}}|0\rangle - \frac{1}{2}|1\rangle + \frac{1}{4}|2\rangle\right).\end{aligned} \tag{2.29}$$

At this point the only difference between the weak measurement description and the LSGI description is that here, the spatial component of the wavefunction has been modified by the introduction of a double slit/diffraction grating. In this case $|\psi\rangle_{path}$ can be described by the wavefunction formulated in section 2.1.1.

The atoms now travel through the weak magnetic field of the phase object which we describe using the time evolution operator

$$|\Psi\rangle_3 = e^{-i\hat{H}_I t/\hbar}|\Psi\rangle_2. \tag{2.30}$$

For an atom in a magnetic field, the potential energy in the Hamiltonian is the Zeeman operator ($\hat{V} = g_f \mu_B \hat{J} \cdot B$). The Hamiltonian does not contain a coupling of the transverse momentum with the phase of the spin. This challenges the idea that this is an AAV type weak measurement as discussed previously, where the interaction Hamiltonian couples the observable to the pointer. However, it is still completely analogous to the work of Kocsis.

The definition of 'weak' for the present measurement

As with the experiment to measure the transverse momentum of photons in a matter-wave interferometer, the coupling of the atomic transverse momentum to the pointer (spin state) does not strictly align with the definition of a weak measurement as defined by AAV. For this to be the case, the interaction strength, $mg_f \mu_B Bt$, would need to be weak enough such that the 1st order Taylor series expansion is approximately equal to the time evolution operator in equation 2.30. However, the simulations performed in this chapter shows no dependence on this limit. Furthermore the Hamiltonian would need to include a transverse momentum component, $\hat{k}_x$. The transverse momentum k_x is introduced into the description via the interaction time, but does not constitute part of the measurement's interaction Hamiltonian.

There are still a number of reasons why the measurement should be defined as 'weak' in a general sense. When the magnetic field is tilted (or when the atom's momentum is not parallel to the field's gradient), the field gradient upon entry to the field imparts a spin-state dependent force in both the x and z components of the atom's momentum. The force can be considered 'weak' if it doesn't spilt the spin states such that the spatial separation exceeds the width of the atom wave packet. This condition of weakness can apply to the force from the gradient or the duration of the interaction and is illustrated in figure 2.10.

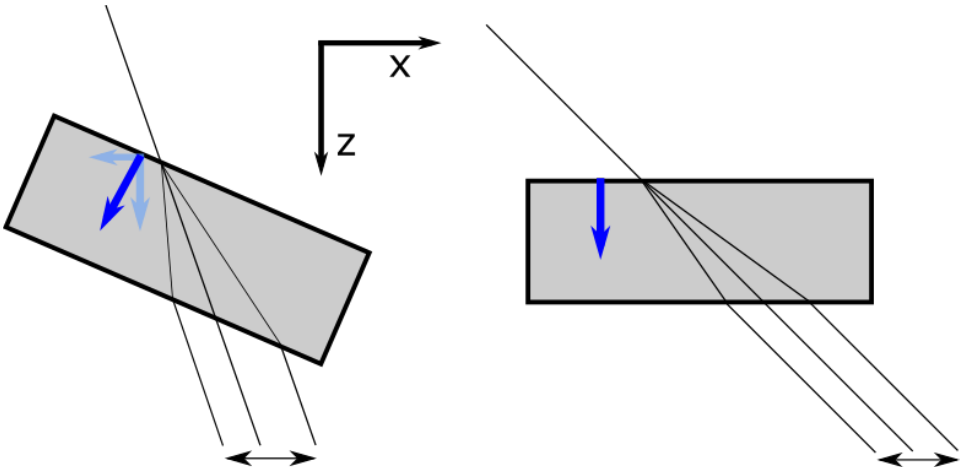

Figure 2.10: Diagram showing how a ‘strong’ interaction with magnetic field can prohibit the phase from being measured. The gradient direction and hence the force direction that the atom experiences going from a region of no field into a magnetic field is shown in blue.

A transverse momentum dependent interaction time

When B is uniform throughout the magnetic field interaction region, the only remaining variable of the atom's evolution is the interaction time, t, which for a tilted field, is dependent on the transverse momentum, illustrated in figure 2.9). After the initial atomic acceleration, the atom falls with an approximately constant velocity, v_0, entirely oriented in the z axis until it reaches the double slits or grating. After the grating the atom has a velocity component in both x and z, the product of which is v_0. Using $t = \frac{L_{ws}}{v_0}$ we can replace t in equation 2.30. The length of the path through the weak stage is

$$L_{ws} = \frac{w}{\cos[\theta_t + \theta_v]} \tag{2.31}$$

where the diffraction angle is $\theta_v = \sin^{-1}[\frac{v_x}{v_0}]$. The expression for L_{ws} for small tilt angles is

$$\begin{aligned} L_{ws} &= \frac{w}{\cos[\theta_t + \sin^{-1}[\frac{v_x}{v_0}]]} \\ &\approx w \sec\theta_t + \frac{w \sec\theta_t \tan\theta_t}{v_0} v_x \\ &= \alpha(1 + \beta v_x) \end{aligned} \tag{2.32}$$

where $\alpha = w \sec\theta_t$ and $\beta = \frac{\tan\theta_t}{v_0}$.

With that, we can write the time dependent phase in equation 2.30 as a function of v_x,

$$\begin{aligned} \frac{\hat{H}_I}{\hbar}t &= \frac{g_f \mu_B}{\hbar} B \hat{J} \frac{\alpha(1+\beta v_x)}{v_0} \\ &= \phi(v_x)\hat{J} \end{aligned} \tag{2.33}$$

where

$$\phi(v_x) = \frac{g_f \mu_B}{\hbar} B \frac{\alpha(1+\beta v_x)}{v_0}. \tag{2.34}$$

The wavefunction in the weak stage is then

$$\begin{aligned} |\Psi\rangle_3 &= e^{-i\hat{H}_I t/\hbar}|\Psi\rangle_2 \\ &= e^{i\phi(v_x)\hat{J}}|\Psi\rangle_2. \end{aligned} \tag{2.35}$$

The spin operator is $\hat{J} = -2|-2\rangle\langle -2| \, - \, 1|-1\rangle\langle -1| \, + \, 0|0\rangle\langle 0| \, + \, 1|1\rangle\langle 1| \, + \, 2|2\rangle\langle 2|$. The equation becomes factorisable with the phase shift now being m dependent. The wavefunction for an atom initially is in a superposition of m states and after a weak magnetic field interaction, becomes

$$\begin{aligned} |\Psi\rangle_3 &= e^{i\phi(v_x)\hat{J}}\left(|\psi_{path}\rangle \otimes \left(\frac{1}{4}|-2\rangle - \frac{1}{2}|-1\rangle + \sqrt{\frac{3}{8}}|0\rangle - \frac{1}{2}|1\rangle + \frac{1}{4}|2\rangle\right)\right) \\ &= |\psi_{path}\rangle \otimes \left(\frac{1}{4}e^{-2i\phi(v_x)}|-2\rangle - \frac{1}{2}e^{-i\phi(v_x)}|-1\rangle + \sqrt{\frac{3}{8}}|0\rangle \right. \\ &\qquad \left. - \frac{1}{2}e^{i\phi(v_x)}|1\rangle + \frac{1}{4}e^{2i\phi(v_x)}|2\rangle\right). \end{aligned} \tag{2.36}$$

To observe $\phi(v_x)$, we must interfere the spin states. This is achieved by a second spin-flip occurring on exit from the weak magnetic field. This $\frac{\pi}{2}$

rotation re-projects each of the five states of $|\psi\rangle_{spin}$

$$
\begin{aligned}
|\Psi\rangle_4 &= D^2\left(\tfrac{\pi}{2}\right)|\Psi\rangle_3 \\
&= |\psi_{path}\rangle \otimes D^2\left(\tfrac{\pi}{2}\right)\left(\frac{1}{4}e^{-2i\phi(v_x)}|{-2}\rangle - \frac{1}{2}e^{-i\phi(v_x)}|{-1}\rangle + \sqrt{\frac{3}{8}}|0\rangle\right. \\
&\qquad\left. - \frac{1}{2}e^{i\phi(v_x)}|1\rangle + \frac{1}{4}e^{2i\phi(v_x)}|2\rangle\right).
\end{aligned} \tag{2.37}
$$

This results in a equation containing 25 terms (appendix A). To simplify, we focus just on the observation of a single m state. In this example, the final measurement is made on the $m = 0$ state so we take coefficients from the the central row of the Wigner matrix. With the values from an initial state $|J = 2, m = 2\rangle$ and by only observing $|J = 2, m = 0\rangle$ after the second projection, the wavefunction is

$$
\begin{aligned}
\langle 0|\Psi\rangle_4 &= |\psi_{path}\rangle\left(\frac{1}{4}\sqrt{\frac{3}{8}}e^{-2i\phi(v_x)} - \sqrt{\frac{3}{8}}\frac{1}{2} + \frac{1}{4}\sqrt{\frac{3}{8}}e^{2i\phi(v_x)}\right) \\
|\Psi\rangle_f &= |\psi_{path}\rangle\sqrt{\frac{3}{8}}\sin^2\phi(v_x).
\end{aligned} \tag{2.38}
$$

The atoms exit the weak stage field and then continue towards the detector to give a position measurement at x_f. The probability density is modulated by the phase shift for which many repeated measurements will build up a picture of the modulated probability density given by

$$
\langle x_f|\Psi\rangle_f = \langle x_f|\psi_{path}\rangle\sqrt{\frac{3}{8}}\sin^2\phi(v_x) \tag{2.39}
$$

which will reveal the phase shift $\phi(v_x)$ of atoms arriving at a given x_f position.

To model the expected signal modulation, we need to model v_x to calculate $\phi(v_x)$. The transverse velocity can be calculated from standard quantum mechanics as shown in [38], giving

$$
\begin{aligned}
v_x &= \frac{\nabla S}{m} \\
&= \frac{i\hbar}{2m}\frac{(\psi\nabla\psi^* - \psi^*\nabla\psi)}{\psi\psi^*}
\end{aligned} \tag{2.40}
$$

which contains the description of the wavefunction's probability current.

For the wavefunction $|\psi\rangle_{path}$, given in equation 2.5, the values of v_x, are calculated for a $50\,\mathrm{ms}^{-1}$ atomic beam using this experiment's geometry and a double slit grating (for simplicity). The observed, unperturbed interference pattern shown in figure 2.11(a), is modulated by an LSGI with width $w = 2\,\mathrm{mm}$, tilt angle $\theta_t = 15°$ and field strength $B = 60.75\,\mu\mathrm{T}$ and shown in figure 2.11(b). The spikes observed in figure 2.11(b) represent the kinks that appear

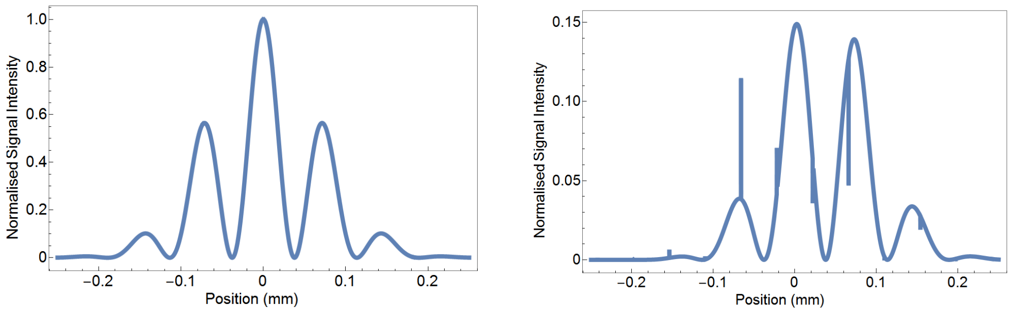

Figure 2.11: (a) A calculation of the probability density at the detector after passing through a 2 slit grating and (b) the probability density which has been modulated by passing through the weak stage measurement.

when plotting flow lines of the probability current.

In order to extract a simulated measurement of ϕ from the modelled data we compare the modulated signal $\langle x_f|\Psi\rangle$ (figure 2.11(b)) with that of the same interference signal, but without the LSGI perturbation, $\langle x_f|\psi\rangle_{path}$ (figure 2.11(a)). This gives a distribution of the phase shift for a range of positions on the detector. Since the phase is dependent on the transverse momentum we can rearrange equation 2.39 to give v_x (for $m = 2$ and $m = 0$ for the initial and final spin polarisations respectively).

$$\begin{aligned}\frac{g\mu_B B}{\hbar}\frac{\alpha(1+\beta v_x)}{v_0} &= \sin^{-1}\left[\sqrt[4]{\frac{8}{3}\frac{|\langle x_f|\Psi\rangle|^2}{|\langle x_f|\psi\rangle_{path}|^2}}\right] \\ v_x &= \left[\left(\frac{\hbar v_0}{g\mu_B B\alpha}\sin^{-1}\left[\sqrt[4]{\frac{8}{3}\frac{|\langle x_f|\Psi\rangle|^2}{|\langle x_f|\psi\rangle_{path}|^2}}\right]\right)-1\right]\frac{1}{\beta}.\end{aligned} \tag{2.41}$$

Using equation 2.40, we calculate the expected distribution of transverse velocity for the atoms for a fixed 'grating to weak stage' distance, shown in figure 2.12. This is ultimately what we would expect to experimentally measure via a measurement of the atom's phase shift. The vertical lines or spikes seen in the plot indicate sudden changes in the atom's transverse velocity which correspond to the kinks of the momentum flowlines. Thus we aim to be able to resolve and measure these spikes in the experiment.

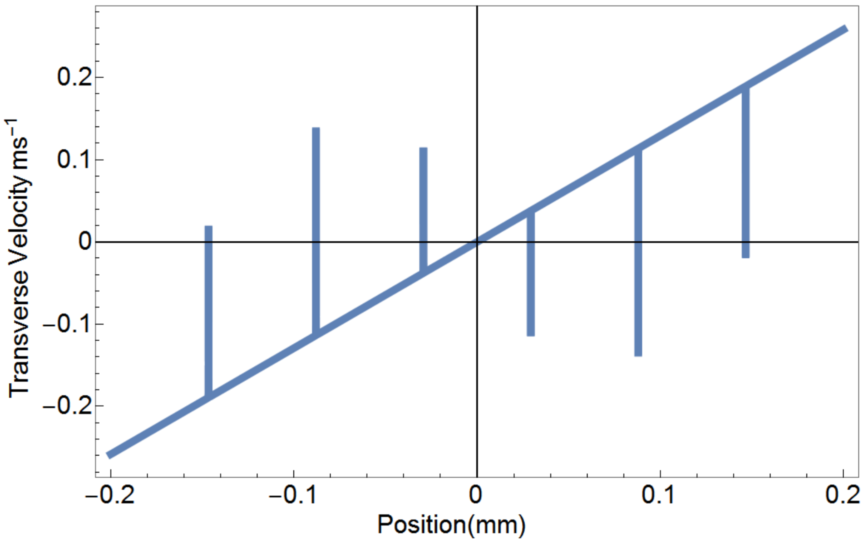

Figure 2.12: The transverse velocity of atoms which have passed through a multi-slit grating. The transverse positions in the plot covers the width of the interference pattern shown in 2.11(a).

2.3.2 Reconstructing flowlines

Thus far, in this simulation the values of v_x are plotted for one dimension with the tilted LSGI at a set distance, z, from the grating. Here, we map the transverse momentum across x and a range of z, in the near field in figure 2.13(a) and in the far field in figure 2.13(b). The variation of v_x in the near field can be seen to be finely detailed and is only detectable with high resolution mapping. The white areas of the plot indicate where the value of transverse momentum has exceeded the range of values on the legend.

If we choose a starting position for the atom, from anywhere across the widths of the grating slits, we can find the atom's expected position at some

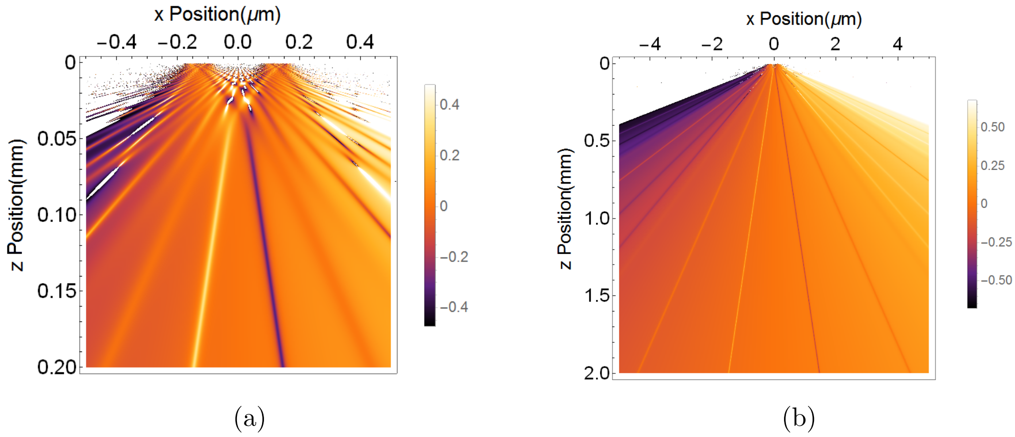

Figure 2.13: The calculated trajectories for a 2 slit grating. There are 200 evenly spaced starting points for each slit (a) The transverse velocity, v_x in ms^{-1} calculated from equation 2.40. This was calculated for atoms in a 2 mm region below the double slits. (b) The transverse velocity, v_x, in ms^{-1} from equation 2.40. This was calculated for atoms in a 150 mm region below the double slits.

time interval later based on the measured transverse momentum at that initial point. To determine how this position, evolves over time, providing it remains localised, we use an explicit Runge Kutta method to solve equation 2.40 for x.

The longitudinal velocity, $v_z(t)$, is dependent on the atom's initial thermal velocity leaving the trap, gravity and the spread of the Gaussian wave packet over time. In the z direction, the change in the wave packet size is negligible compared to the changing position due to the initial velocity, therefore the z position can be treated classically as

$$z(t) = v_0 t + \frac{1}{2} g t^2 + z_0 \frac{\sigma_z(t)}{\sigma_z} \tag{2.42}$$

where the final term, which describes the change in the width of the wavepacket can be neglected. With x and z computed for a range of values of t, we can plot, parametrically, a local momentum flow line, also described as a trajectory [30].

We present the results for the flow lines in the near field (2 mm) and far field (150 mm), for step sizes of 0.1 μm. If the step size is any larger, the plot does not account for the finer detail of the interference in the near field. For each plot, the starting positions are given for 100 evenly spaced x values, between the walls of each slit in the double slit grating. This is shown in figure 2.14

and agree well with previous work [38].

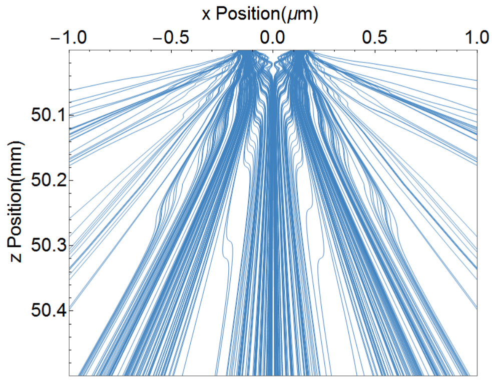

(a)

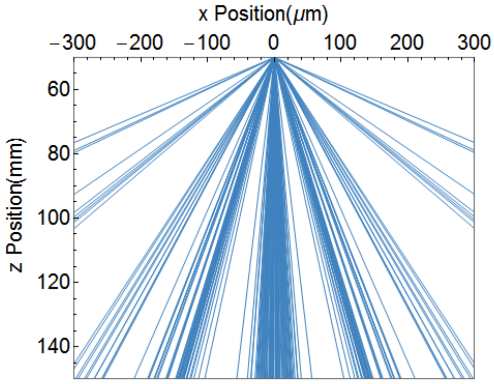

(b)

Figure 2.14: The calculated trajectories for a 2 slit grating. There are 200 evenly spaced starting points for each slit (a) shows the trajectories 0.5 mm below the slits and (b) over 100 mm below the slits. The values on the z axis are measure from the trap. The grating is positioned 50 mm below the trap.

These flow lines represent an ideal version of the expected results from this project's ultimate experiment. The feasibility of achieving such results depend on the capability and limits of the weak measurement design, the details of which make up the majority of this thesis.

Chapter 3

Creating a low velocity and tuneable, atomic beam

3.1 Introduction

To ensure the matter-wave interferometer produces well resolved interference fringes, it requires an atomic beam with a well-defined velocity and narrow velocity spread. Additionally, the beam must have a de Broglie wavelength of approximately 1-10 Å to achieve sufficient longitudinal and transverse coherence in our experimental setup.

An existing cold atom source in the form of a magneto-optical trap (MOT) was modified for this purpose. The MOT traps and cools metastable argon atoms and presents many convenient advantages over other atomic beam sources. For example, the metastable atoms are easily detectable and the low temperatures provide an initial de Broglie wavelength 10 times larger than typical effusive and thermal sources.

This chapter describes the construction and testing of the atomic beam used for the experiment, beginning with a review of cold atom beams. Following this is a description of the cold atom source and the atomic detection process used in this project. Finally, the atomic beam, which is created by accelerating the atoms, is characterised by measuring its time-of-flight (TOF) velocity, velocity distribution and atomic spin polarisation.

3.2 Conventional cold atomic beams

The supersonic atomic velocities produced by conventional atomic beams can be greatly reduced using optical manipulation of the atoms such as optical scattering and dipole forces. Applying counter-propagating cooling radiation to a typical effusive, high intensity beam in the form of a Zeeman slower has been achieved with Rb and Ne where an atomic beam velocity, v, in the region of 45-120 ms^{-1} is produced, with Δv=9 ms^{-1}. This velocity can be measured by either the time-of-flight method [41] or by spectroscopic techniques which measure the Doppler shift to infer the velocity [42].

To create very low energy, cold atomic beams the thermal or effusive sources are substituted with cold, trapped atoms [16]. The atoms can then be accelerated by applying controlled optical forces to the trap. While dipole forces, produced by off-resonant fields, have been used to create pulsed, low energy beams, it is more common to use the radiation pressure force of a resonant or near resonant optical field. By unbalancing the power of the trapping forces in a MOT, a low velocity intense source (LVIS) can be created. Velocities in the region of 14-18 ms^{-1} with a 3 ms^{-1} distribution [17, 43] can be created in this way.

To extend the velocity range, a laser beam separate from the trapping beams can be applied as a pulse. This extends the range over which the beam's velocity can be selected, achieving velocities of 10-150 ms^{-1} with a velocity width of 7 ms^{-1} [16, 44].

Finally the ability to characterise atomic beam properties is critically important for constructing an experiment to measure the transverse momentum-dependent phase in a multi-slit grating, matter-wave interferometer. The atomic beam velocity and velocity distribution have a direct effect on the fringe separation and fringe contrast of the interference pattern. Additionally, the spin polarisation of the atomic beam must be considered in order to measure the Zeeman phase shift in a spin-state interferometer.

3.3 Cold atom source

3.3.1 The magneto-optical trap

The magneto-optical trap (MOT) cools and traps a cloud of atoms in an ultra high vacuum. It uses a quadrupole magnetic field and three pairs of orthogonal laser beams to optically cool the atoms in all directions. The argon atoms are cooled by absorbing and scattering photons in a closed cycle transition [53]

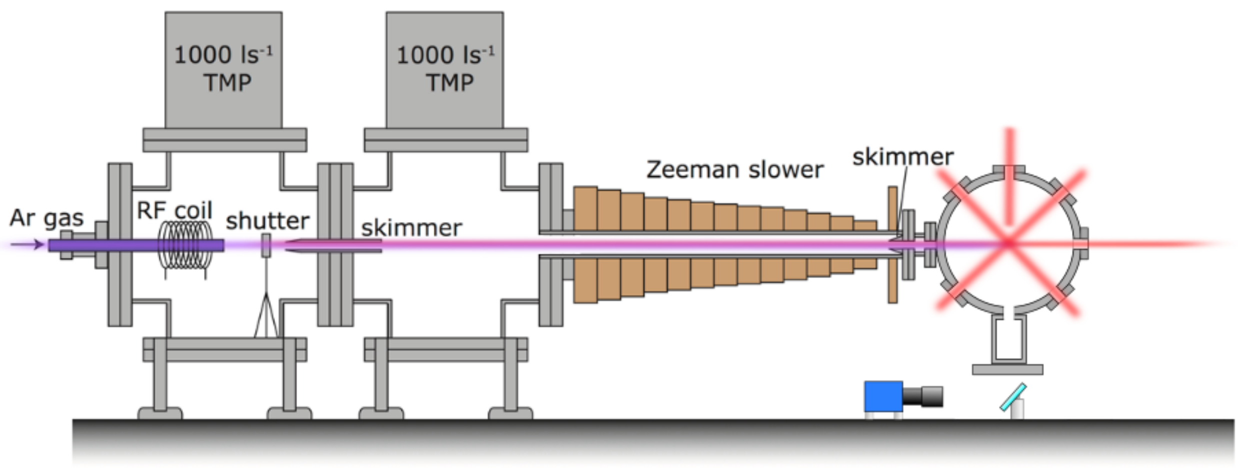

Figure 3.1: The vacuum setup used to create the metastable argon MOT. The gas passes through two, 200CF, 6-way cross chambers, including a skimmer between the chambers to collimate the beam. After the 2nd chamber, the Zeeman slower coils extend towards the spherical octagon MOT chamber, while the Zeeman beam counter-propagates the atomic beam. The MOT chamber contains the trapping and push lasers. Attached to the bottom of this chamber is the detector, upon which the camera is focussed. Not shown is a 200 ls^{-1} turbo molecular pump attached to the MOT chamber.

The atoms reach the intersection of the beams, where laser cooling takes place, via 4 steps. First, ground state argon is fed into the differentially pumped vacuum chamber creating an effusive atomic beam. A radio frequency discharge is created in the gas which produces the $4\mathrm{s}[3/2]_2$ metastable argon atoms. The metastable atoms with very low transverse velocity travel towards the trapping chamber and are cooled using a Zeeman slower. The atoms in the beam are slowed by the counter propagating Zeeman slower laser beam until they reach the intersection of the three MOT beams, where they are cooled from six directions and trapped as shown in figure 3.2. The MOT is then used as the source for the cold atomic beam.

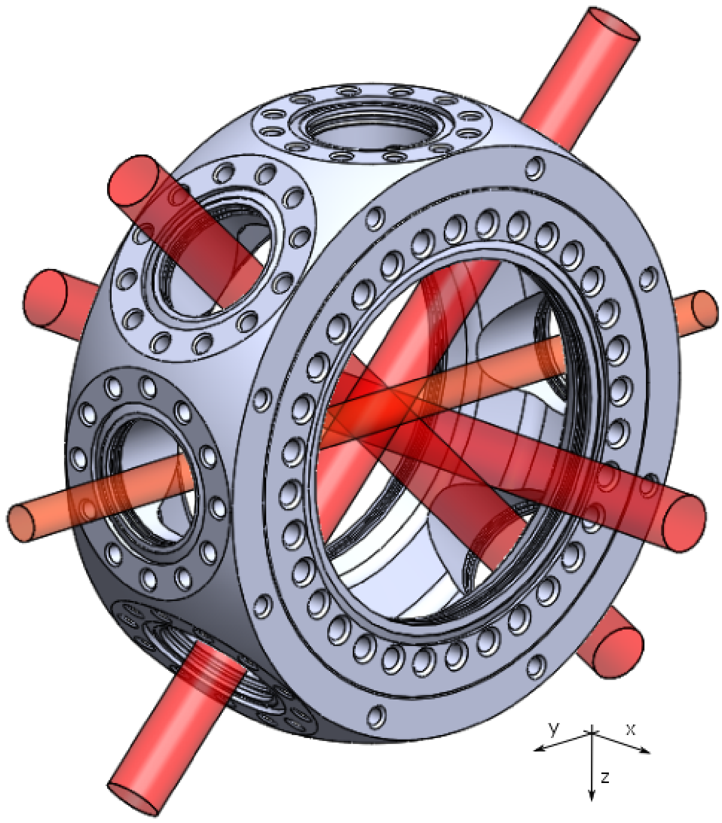

Figure 3.2: Main chamber showing paths of the orthogonal laser beams (red) and the Zeeman slower beam (orange). The axes show the co-ordinate system used throughout this thesis.

The cooling beams alone are not sufficient to trap the atoms. A single pair of counter propagating beams creates an optical molasses, which cools the atoms along the axis of the beams. However, they cannot keep the atoms localised. In order to create a trapping region, a magnetic field works in conjunction with the beams to create an optical force which is position dependent.

The necessary field is created by a pair of anti-Helmholtz (AH) coils. In our case, the coils are 160 mm in diameter and placed 76 mm apart. This creates a magnetic field with a small region of zero field strength in the centre of the chamber which then increases in field strength with the distance from the centre. The magnetic field shifts the frequency of the atomic cooling transition by an amount dependent on the atom's position. The frequency of the cooling beams is red detuned, such that the strongest interaction with the laser radiation will happen when the atoms reach a certain distance from the centre. This creates a spatial region within which the atoms remain trapped. Figure 3.3 shows the entire mechanism for a spin-state system of $m = -1, 0, 1$.

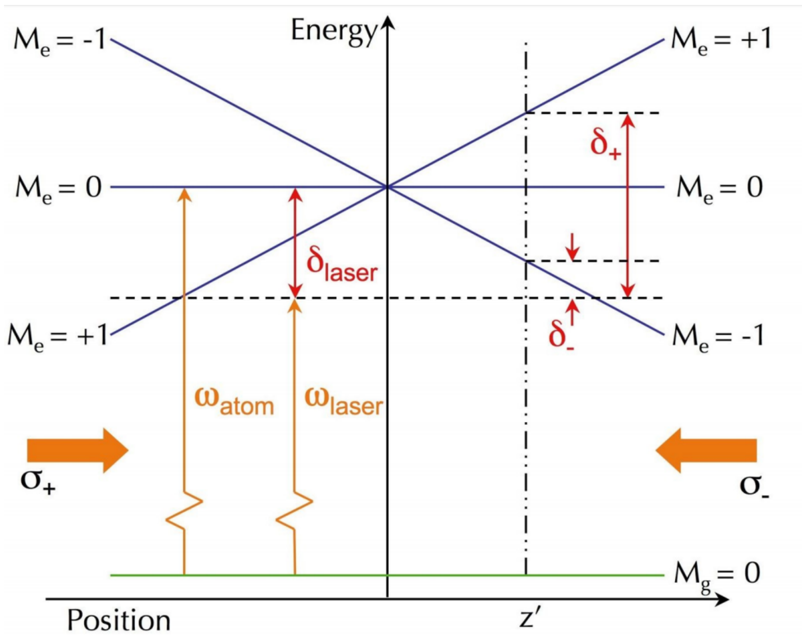

Figure 3.3: A 2D schematic of how a MOT works for a simpler 3 state system of J=1 and $m = -1, 0, 1$. This diagram indicates the interplay between the atom's resonant frequency ω_{atom}, the frequency of the laser, ω_{laser}, the detuning, δ_{laser}, and the shift in the atom's energy levels as a function of position. Also shown is how the radiative cooling effect is modified using polarisation such that even though any atom is constantly radiated by beams from both directions, the atoms only experience a force towards the centre of the MOT. This is achieved by using a different circular polarization ($\sigma^+\sigma^-$) for each beam and using a magnetic field to rotate the atom's quantisation axis so they will only absorb a particular polarisation of photon.

Optimising the MOT for an atomic beam source

Optimising the MOT as an atomic source for matter-wave interferometry generally involves adjusting the position and size of the MOT and maximising the density of the trap. It is also beneficial to minimise the temperature of the atoms.

The location of the zero magnetic field region, which determines the position of the MOT, is changed by adjusting the background magnetic field. This field can be controlled using a 'compensation cube' made up of 3 pairs of square Helmholtz coils arranged in a 600 mm x 600 mm x 600 mm cube. The MOT's position is generally kept in the centre of the chamber, but is adjusted for maximum throughput given the introduction of the push beam which directs the atoms through two collimation slits.

We use two collimation slits positioned below the MOT, therefore the fluctuating volume of the MOT does not have an effect on the beam density. The slits define the beam's effective source size and so the beam intensity is primarily determined by the slit width. The MOT is typically $\approx$1 mm wide, with the slits 10-50 μm wide, so any increase in MOT size does not have an equivalent increase in signal. Instead, to maximise the signal intensity, the atomic density of the MOT is maximised. This involves optimising the frequency, alignment and power of the Zeeman slower and cooling beam.

The MOT density has an upper limit due to the absorption saturation parameter for metastable argon and intra-trap collisions, so as the MOT volume decreases, the density remains constant at the upper limit, (provided the MOT is configured correctly). However, if we choose to expand the volume of the MOT, by reducing the trapping field strength and the detuning of the tuning beams, the density is reduced but can be compensated by higher beam power. A less dense MOT provides cooler atoms and a larger volume can help with alignment.

MOT characteristics

The cooling process causes florescence from the trapped atoms and this light can be used to estimate the number of atoms in the MOT via the equation for the photon scattering rate [53], equation 3.1

$$N_{Ar^*} = \frac{1 + 6s_0 + (2\Delta/\Gamma)^2}{6s_0(\Gamma/2)\Omega_d l} \frac{N_{counts}\eta}{t_{exp}} \tag{3.1}$$

where $s_0 = I/I_0$ and I is the power density of the cooling beams. I_0 is the absorption saturation intensity. Δ is the detuning from resonance, Γ is the natural linewidth, N_{counts} is the number of photons that the camera measures, η is the efficiency of the camera, Ω_d is the fraction of the total light emitted that the camera sees, l is a factor that accounts for attenuation from all the imaging optics and t_{exp} is the camera exposure time. Given that the MOT typically has a $\frac{1}{e^2}$ radius of approximately 500 µm, the calculation gives the MOT in our experiment a typical density of 1.7×10^6 atoms mm^{-3}, trapping approximately 9×10^5 atoms.

When atoms are released from the trap, a period of time must pass before the MOT can reload and return to its original size and density. This forces the experiment to use a pulsed operation (whether dropping or pushing). For efficient data taking, the time for one drop cycle should be minimised. Therefore, to maximise the atoms arriving at the detector, it is useful to know how long it takes for the MOT to fully load.

3.3.2 Laser system

The accessible closed cycle cooling transition for argon is between the $4s[3/2]_2$ and the $4p[5/2]_3$ metastable states, using light from an 811.5 nm laser beam. An external cavity diode laser (Toptica DL100) was used for the main optical source. However, this alone did not provide enough power as the optical requirements for this experiment meant dividing the laser power between cooling beams (approximately 4 mW per beam), the pump and probe beam for laser frequency locking (20 mW), the Zeeman slower beam (20mW) and the push beam (5 mW). As a result the output was sent through a tapered amplifier (Moglabs MOA) which could provide up to 1W of power if needed. Considering losses across the laser setup, the average total laser power needed for this experiment was in the region of 500 mW.

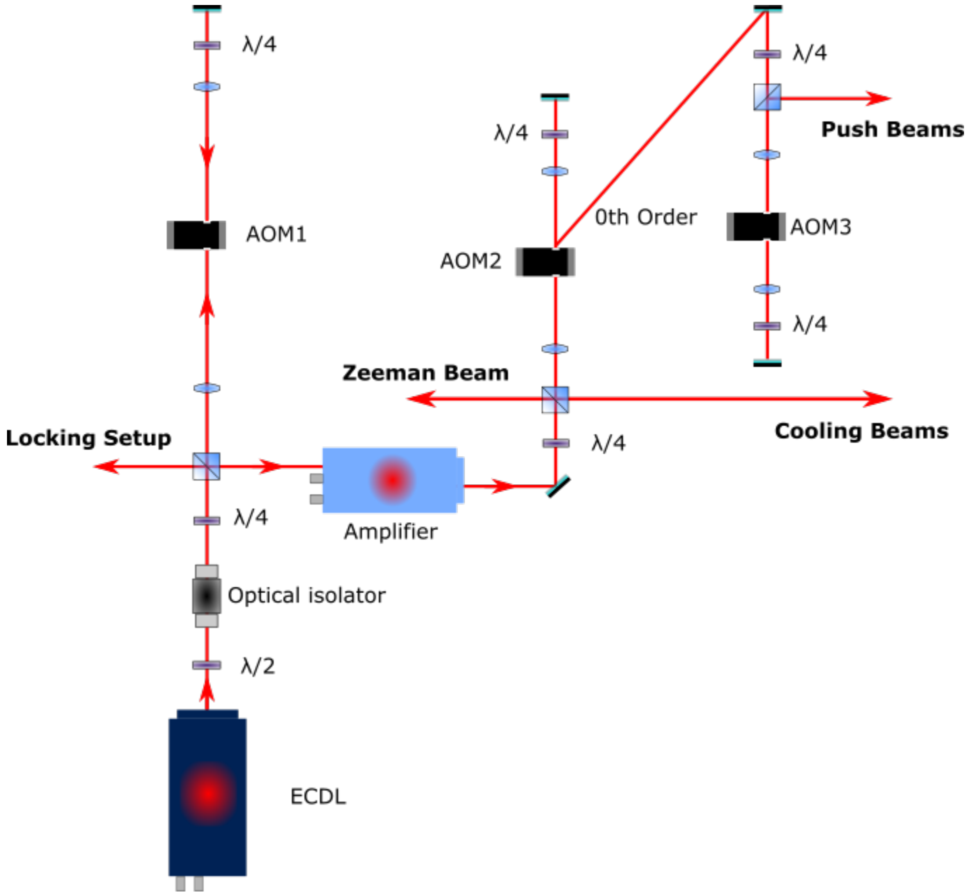

Figure 3.4: Schematic of the laser system. Lenses and polarizing beam splitters are unlabelled and coloured blue. In reality, the 0th order from AOM2 would actually be straight and the 1st order, which is retro-reflected, is emitted at angle.

The laser frequency was locked to the 4s$[3/2]_2 \rightarrow$4p$[5/2]_3$ transition frequency using the discharge from the RF source (see following section). The laser was then detuned by various amount depending on th application. It was necessary to detune the Zeeman slower beam by a much greater frequency than the MOT beams in order to match the Doppler shifted frequency as a result of the counter-propagating atomic beam. The Zeeman slower beam was red detuned by approximately 154 MHz. This was achieved with an acousto-optic modulator at 77 MHz in a double pass configuration (AOM1 in figure 3.4). The beam power is then amplified using a tapered amplifier. A fraction of the output was used for the Zeeman slower beam, while the majority of this red detuned beam is shifted back up by 138 MHz via a second AOM (AOM2 in figure 3.4) in a double pass configuration. The output from AOM2 was then used for the MOT beams. The final frequency was red detuned by 16 MHz from the natural resonant frequency of the cooling transition. This detuning can be adjusted by controlling the frequency of the RF signal sent to AOM2 and ultimately controls the temperature of the atoms in the trap. The push beam makes use of the discarded 0th order transmission from AOM2, as this can be directed into a third AOM (AOM3), which shifts the beam frequency back up by around 160 MHz. The frequency shift can be adjusted so the final frequency is then blue detuned between 4 and 15 MHz from resonance. The advantage of using a 3rd AOM is that the frequency of the push beam can be controlled independently from the cooling beams.

3.3.3 Metastable atom generation

The atoms can interact with the laser when they are excited to the metastable state, the excitation is achieved using a radio frequency (RF) discharge. This is also used as a reference cell with which to lock the frequency of the trapping laser via Doppler free absorption spectroscopy [52].

Argon gas passes through a leak valve and into one end of a quartz 10 mm diameter pipe. The pipe extends 200 mm into the entry chamber as shown in figure 3.1. A 40 mm diameter copper coil wraps around the pipe and is enclosed in a brass cylinder which acts as a RF resonator. A 30 W, 135 MHz RF signal is fed into the coil and is impedance matched into the coil using an antenna tuner (MFJ-924). The RF field accelerates free charges which initiates collision processes with argon atoms and result in excitation of the argon atoms. The discharge can be observed by a purple, fluorescent glow. One of the many excited states that are created is the $4s[3/2]_2$ metastable state used for laser cooling. This has a half life of 38 s and previous work has shown the efficiency of metastable production to be 1 in $1{\times}10^5$ [52]

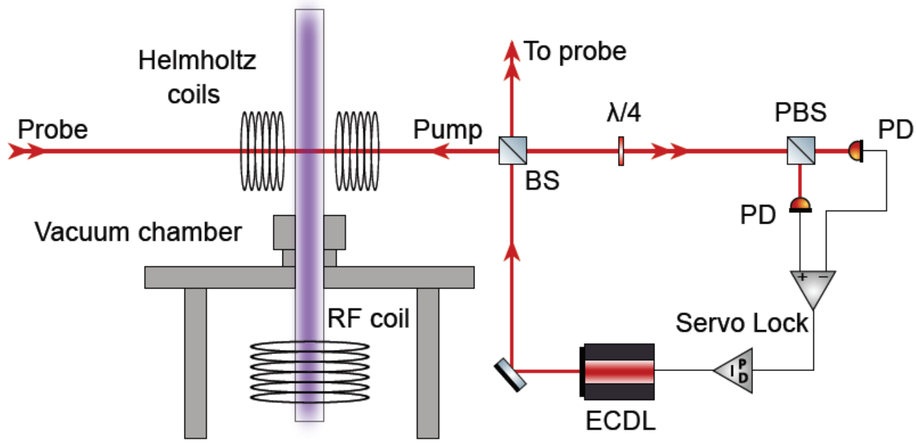

Figure 3.5: A schematic diagram of the laser locking setup. The RF discharge, which creates the metastable argon atoms, is shown in purple. This is used instead of a vapour cell typically used for frequency locking of the laser to the atomic transition.

The discharge extends away from the coil and out of the chamber. Just outside the chamber we perform saturation absorption spectroscopy to lock the frequency of the laser. We pass a π-polarised pump and probe beam through the gas as shown in figure 3.5, which provides a Doppler free absorption peak when we analyse the probe beam. Two coils placed either side of the discharge, create a magnetic field which causes a Zeeman shift in the spin states of the metastable atoms. This slightly shifts the transition frequency, in opposite directions for positive and negative m states, and an equivalent shift is observed in the absorption peaks. The probe beam output is separated into its horizontal and vertical polarisation components and the intensities are measured separately on 2 photodiode detectors.

The two signals are fed into a servo controller (New Focus LB1005) which subtracts one from the other to create a new error signal. The servo controller uses the error signal to output a feedback signal that controls the laser frequency via a piezo-electric transducer. The signal is sent to a piezo motor controlling the angle of a grating in the ECDL. Thus the servo controller can set the laser at the exact frequency of the transition and keep it there for long time periods, compensating for any drift in laser frequency due to temperature changes for example.

3.3.4 Vacuum system

The MOT vacuum system consists of 3 main stages. The entry chamber, the Zeeman slower and the trapping chamber as shown in figure 3.1.

The first stage, is split into two identical sections, each with a $1000\,\mathrm{ls}^{-1}$ turbo molecular pump. The argon enters the first chamber through a leak valve at a pressure of 6×10^{-2} mbar. As a result, the pressure in the second entry chamber is about 3×10^{-8} mbar. Between the two sections is an externally controlled shutter which can be closed to block the atomic beam. This is necessary when we want to detect atoms from the MOT since atoms in the atomic beam, which do not become trapped, create a large amount of background noise on the position detector and dominate the atomic signal from the MOT. The Zeeman slower connects the two entry chambers to the trapping chamber. The trapping chamber is a spherical octagon, which has 10 viewports in total, providing optimal optical access while keeping the overall volume small. One side of the trapping chamber connects to a $200\,\mathrm{ls}^{-1}$ turbo molecular pump where we measure a pressure of 1×10^{-8} mbar. Connected to the bottom of the octagon is the micro-channel plate and phosphor screen which observes the atom's positions. It is attached by a purpose built flange which maximises the distance between the trap and the detector.

3.4 Detection

An argon atom in the metastable state not only has an accessible transition frequency for commercially available NIR lasers at 811.5 nm, but is also easily detected via ionisation due to its high-lying outer electron (11.5 eV), which is close to the ionisation potential (15.8 eV).

Each push cycle can deliver anywhere between less than one and as many as 10,000 atoms to the detector, depending on the experimental configuration. For example, the narrow transverse velocity created using 2 collimating slits (10 μm and 50 μm) with an average atomic velocity of $14\,\mathrm{ms}^{-1}$ observes roughly one atom every 3 cycles. With one collimation slit and an average atomic velocity of $50\,\mathrm{ms}^{-1}$ (used for testing the spin-state interferometer) the detector sees roughly 300 atoms per cycle. The throughput could be improved with a further transverse cooling stage either with existing beams or a new beam.

Individual metastable atoms arrive at the detector, which in turn emits a packet of photons to indicate the position of the atom. The light reaches the sensor of a CCD camera, which produces a digital 2D image indicating the atoms' final position.

3.4.1 Micro-channel plate detector

The detector is a stack of two micro-channel plates and a phosphor screen. Each of the two plates have multiple 6 μm diameter tubes ('channels') coated in a secondary emissive material. When an ion or electron is incident on a channel, it will cause the surface of the channel to emit electrons. There is typically a potential difference of 1.7 kV between the top and bottom plates, so the electrons are accelerated down the channels. The channels are set at an angle of 5° from the vertical axis and the electrons repeatedly hit the tube surface causing a cascade of electrons down the 300 μm long tube. For increased gain, this process is repeated as the cascade hits the second plate, as shown in figure 3.6. The second plate is set at -5° to the vertical axis, creating a 'V' or ‘chevron’ stack overall. Finally the cascade of electrons are accelerated towards a phosphor screen, which is at a further 2.5, kV potential difference from the 2nd plate. The accelerated electrons cause the phosphor to fluoresce, and the photons are observed by imaging the phosphor screen on a CCD camera (PCO PixelFly).

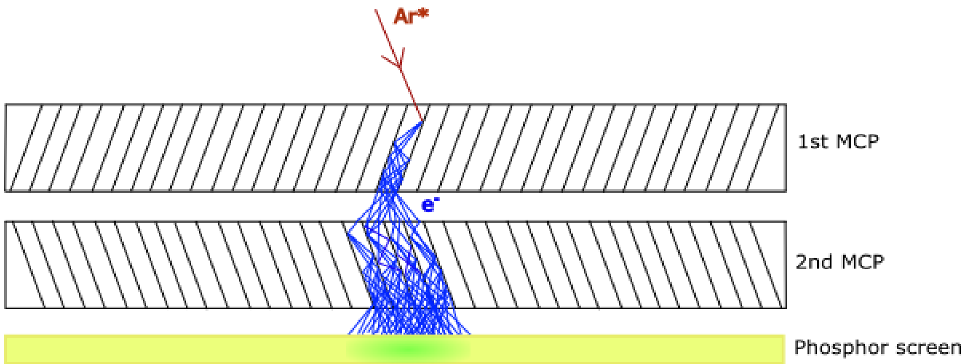

Figure 3.6: Schematic of the detection process within the MCP.

The spatial resolution of the detector is initially defined by the width of the channels. However, the channels emit a diverging cascade of electrons, so while the introduction of a second micro-channel plate increases the sensitivity, it also degrades the observed resolution. One micro-channel plate has an ultimate resolution, defined by the tube diameter, of 6 µm. The electron cascade exiting the 1st plate will spread to more tubes on the second plate, bringing the resolution to at least 12 µm. This increase in resolution will depend on the distance between the plates and the inter-gap voltage accelerating the electrons. The inter-plate distance is determined by the thickness of the ceramic spacer used to insulate one plate from the other and is 300µm, however the detector electronics can be developed to allow both plates to be in contact to improve the resolution. This wasn't required for this project, but may be useful for future designs. The same ‘distance-resolution’ dependency applies between the second plate and the phosphor screen. The actual resolution observed in the raw signal is harder to define for a number of reasons. The spatial distribution of photons from the signal of one atom is Gaussian so we consider the ability to separate two Gaussian peaks. This depends on the signal noise, overall stability of the apparatus, the size of the phosphor grains, the voltage on the plates and the spatial sampling given by the pixel size and camera-detector distance. However, the typical resolution for this detector setup is between between 40 and 60 µm. The average signal from one atom can be seen in figure 3.8. Further steps in processing the detection images to improve the resolution are described in section 3.4.3

The detector plates were changed a number of times during the course of the experiment. The high voltages make the plates very susceptible to arcing if there is any microscopic debris touching the plates. As a result of one MCP repair, the ultimate resolution of the plates was downgraded from 5 µm to 6 µm, since only 6 µm channel plates were available. Also, the replacement plates had a reduced gain factor since the only available plates were without a magnesium oxide coating (a secondary electron emission material) typically available for MCP detectors.

3.4.2 Camera/plate voltage exposure time

Considering a single digital image, the detector can provide information about the spatial distribution of the atomic beam, but does not give information about the velocity distribution. Only by taking images at different TOF arrival times can a time dependent picture of the atomic signal be constructed. For the data in figure 3.12, the camera only acquires photons for 10 ms, triggered to begin at a chosen arrival time. After 100 cycles, an average number of detected atoms can be calculated for that particular arrival time. The trigger time to begin the 10 ms exposure is increased in 10 ms increments.

This method does not provide enough temporal resolution if you reduce the exposure time below ≈1 ms. This is partly because the phosphor used to make the detector (P43) takes 1 ms for the intensity of the emitted photons to decay from 90% to 10% [54]. So for example, even if the camera sensor may only be exposed for 0.5 ms, the fluorescence from atoms which have arrived just before this period will still be emitting photons during the selected exposure window.

To overcome the problem the MCP voltage is gated. When gating the detector, the voltage on the top plate is kept at 1.5 kV instead of 1.75 kV. At this lower voltage, the plates do not accelerate the electrons enough to cause florescence on the phosphor screen. A TTL pulse is delivered to a switch in the MCP voltage circuit which causes 250 V to be added to the top plate. When this extra voltage is present, the detector can accelerate electrons enough for the resulting fluorescence to be observed by the camera. The length of the TTL pulse determines the period of time that any atoms impinging on the detector cause florescence. Any atoms arriving just before this window will not have initiated a significant electron cascade. Using this technique, a much finer time resolved plot of arriving atoms was achievable and is shown in figure 3.7. Knowing the atom's arrival time more precisely, allows a better measurement of the beam's velocity distribution.

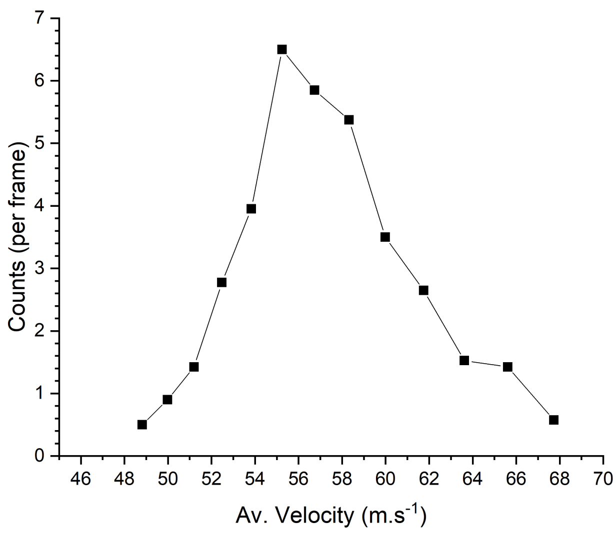

Figure 3.7: The velocity distribution of the MOT cloud, derived from TOF measurements. The beam was created with a push beam pulse length of 0.6 ms and push beam detuning of 20 MHz. This was measured using a gated detector allowing a time resolution of 0.5 ms.

It is also useful to think of the gating in terms of the portion of the falling atom cloud that the MCP will detect. The difference in velocity between the atoms that arrive first and last in figure 3.7 is about $19\,\mathrm{ms}^{-1}$. From this we can calculate that the MOT cloud will have stretched out to approximately 50 mm long by the time it reaches the detector. If we then gate the detector for 50 µs such that we only see atoms that arrive at the detector within this time period, the gating time will correspond to 2-3 mm of the total 50 mm atom cloud (depending on when you begin the gating since distance is inversely proportional to time). This is relevant as it provides the distance over which we need the magnetic field to act uniformly in the spin-state interferometer and weak measurement.

3.4.3 Image processing

Generally speaking, the signal from a single push cycle does not give enough useful information and an average of many push cycles is required. For example, depending on the configuration, anything between 50 and 50,000 frames are needed to build up an image of the distribution of positions where atoms are detected. From the averaged image we can then measure the spatial probability density distribution in space for a particular time-of-flight range.

The image of a single atom hit is pixelated, as shown in1 figure 3.9(a). With the camera at full zoom, each pixel from the camera can detect photons over a distance of 11.6µm on the phosphor screen. Figure 3.8 shows the average peak from 14 single atom detections. The pixel values are converted into a floating point format that MATLAB can process. A threshold operation is applied which selects all the pixels below a certain threshold value and reduces these pixel values to zero. At the same time all the pixels above that value are increased to 1, as shown in figure 3.9(b). This is called 'binarising'. During this operation, information about the peak shape is lost and a Gaussian shape in the raw signal is converted to a binary peak. This would reduce the ability to resolve between two overlapping peaks. However, in cases when ultimate

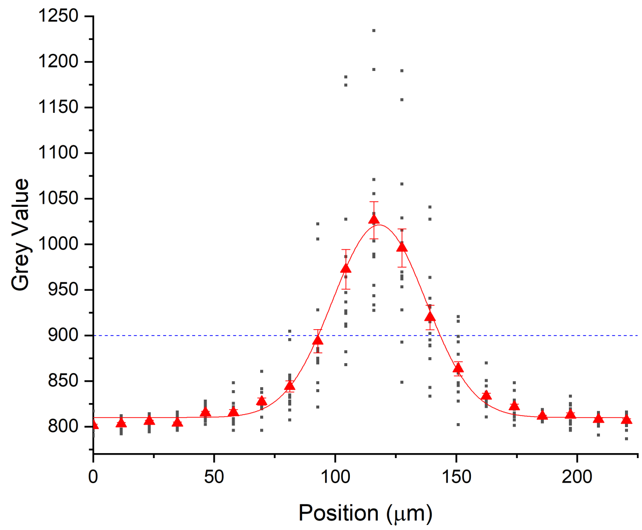

Figure 3.8: The profile of an average signal peak from the detection of a single atom. Here there are 14 peaks (black squares) and their average (red triangles). The grey value is the 16 bit value recorded by the camera.

resolution is not critical, the process gives the final image a higher contrast and allows MATLAB to easily count the number of atom hits. The processed image from each push cycle is averaged. The individual atom hits then begin to effectively form a 2D probability distribution.

Binarising also improves the temporal resolution of the detector. When one atom hits the detector, the decay time of the phosphor means photons from this event will be detected by the camera over a period of ≈1 ms. The signal intensity will vary over time as a result of the decaying florescence. If a threshold is set to only select the very brightest signals, the weaker florescence signal, originating from atoms that arrived in an earlier time frame is not included.

If we take the outline of the signal from a single atom hit, we can read an $\{x, y\}$ co-ordinate closest to the centre of the fluorescence signal. This acts as a good estimate of the atom's final position. This co-ordinate can be assigned to the nearest integer and hence pixel. Setting this pixel value to 1, improves the spatial resolution since the original signal width, a Gaussian peak covering

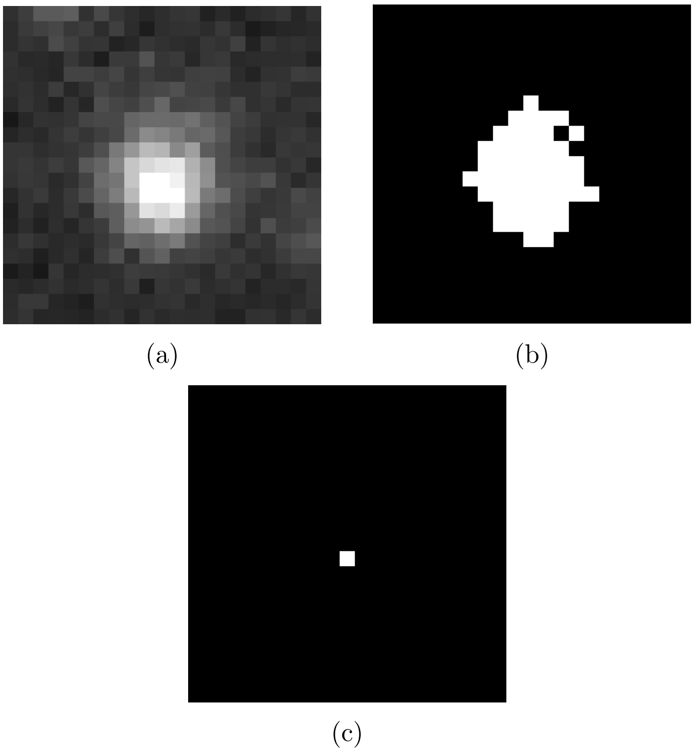

Figure 3.9: Three stages of the centroiding process. (a) Shows the pixel intensity of an image of a detector image zoomed in to a single atom hit. (b) Shows the same data after it has been binarised according to a chosen threshold and (c) shows the single pixel calculated as the approximate centre of the position signal.

multiple pixels, has been reduced to a single pixel. The detector's spatial resolution is now limited to the distance over which one pixel is observing on the detector which in our case was 11.64 μm. This technique is known as 'centroiding' and an example is shown in figure 3.9(c). While it is useful to know how to push the detector's resolution to it's maximum, there are some limitations to consider. The centre of the signal in figure 3.9(a), does not necessarily relate to the exact position that the atom arrived at the detector. The initial angle of incidence of the atom, the angled channels and the resulting emission angles of the cascading electrons all contribute to the shape and spread of the detector signal. The 'un-binarised' signal conveniently incorporates the uncertainty of the atom position into the signal. Additionally, in practice, images using the centroided signal require a much greater overall atom count to clearly see the shape of the atomic beam or interference, so the centroiding method was not often used.

3.5 Gravity accelerated atoms

The spherical octagon chamber, shown in figure 3.2, was chosen to fit a cooling beam configuration that allows the atoms to fall unobstructed towards the detector. The atom cloud is dropped by turning off the cooling lasers and the AH coils. Turning off just one of the two components results in additional forces on the atoms, which either restrict or completely inhibit atoms travelling from the trap position to the detector.

When both components are turned off, atoms will travel in all directions, with a mean velocity, v_0 determined by the trapped atoms' mean temperature, T.

$$v_0 = \sqrt{\frac{k_b T}{m}} \tag{3.2}$$

where m is the atomic mass and k_b the Boltzmann constant. All the atoms fall under gravity, but those with a larger velocity component in the xy plane, have a higher probability of hitting the chamber wall before they reach the detector. In a collision, the metastable atom will ionise. The greater the x or y velocity, the more likely it is to hit the wall before the detector. The number of atoms reaching the detector was counted for different TOF arrival times. The arrival time gives a value for the average velocity using simple kinematic equations. This was repeated for different trap temperatures, as shown in figure 3.10. The initial velocity was converted to an initial temperature using equation 3.2. The area under the curves represent the approximate total number of atoms reaching the detector from the MOT, which slowly decreases for higher temperatures.

Initially without this atom detector, a complicated method was used to estimate the trap temperature consisting of taking a snapshot image of the MOT expansion immediately after the trap is turned off. However, this method would only give a single average value of the temperature. Here, with this TOF method, we can observe an average velocity and the distribution of ve-

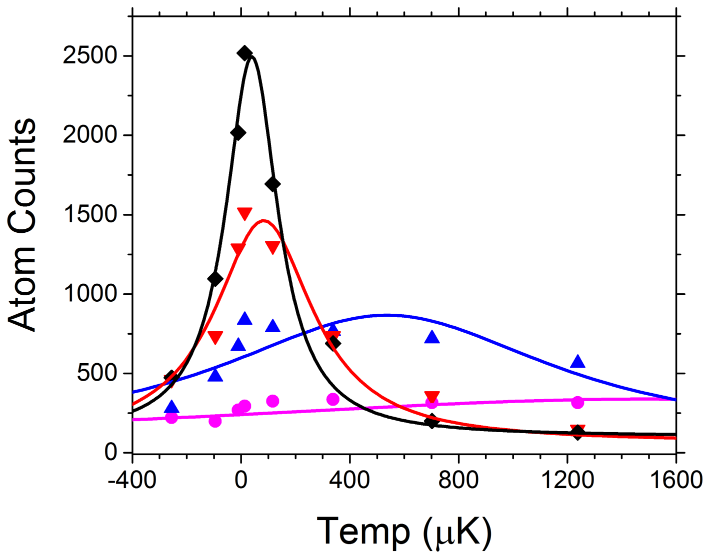

Figure 3.10: A plot of the temperature distribution in the MOT for different cooling beam detuning frequencies of 6 MHz (magenta), 10 MHz (blue), 14 MHz (red) and 22 MHz (black) where the laser is red detuned from the $4s[3/2]_2 \rightarrow 4p[5/2]_3$ transition frequency. The temperature is taken from the TOF distribution after releasing the atoms by turning the trap off. The signal intensity is a measure of how many atoms arrive at the detector at a particular time and hence have a particular velocity which then can be used to determine the temperature.

locities together. The data shows that as the detuning of the cooling beams is increased, the average temperature of the atoms reduces.

To achieve sufficient transverse coherence for the interferometry experiments, it was necessary to select a narrow range of transverse velocities using collimation slits. There was little success in using the gravity acceleration method with collimation slits for 2 main reasons. Firstly, it was difficult to completely block out atoms with high transverse velocities, once they leave the trap they can bounce all around the chamber, often ionise along the way, but many atoms still make it to the detector, contributing to excessive noise in the signal. Secondly, the metastable state is deflected by magnetic fields present in the chamber. The compensation cube is effective at creating a zero or extremely low field, in a small region within the centre of the chamber, but this condition is not maintained along the whole path of the falling atoms. This effect was modelled and shown to introduce a significant element of transverse

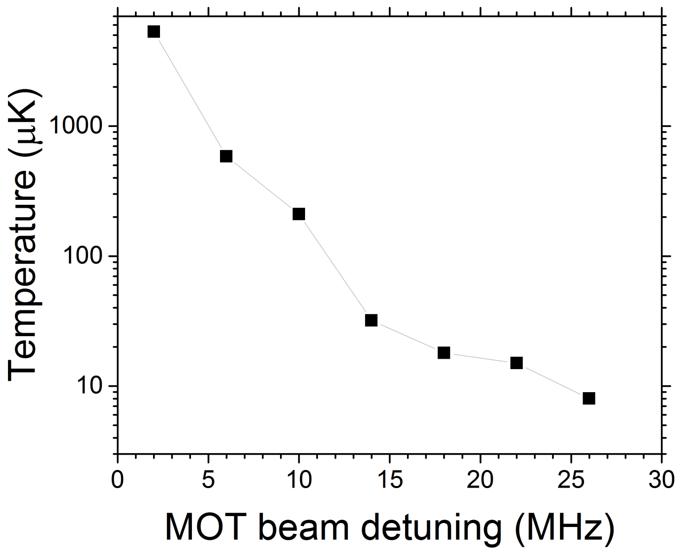

Figure 3.11: The peak MOT temperature as a function of the cooling beam frequency detuning. This data was derived from the TOF distributions shown in figure 3.10.

velocity since the atoms travel so slowly. This could potentially be overcome by using the 801 nm laser to quench the atoms and only detect the magnetically neutral $m = 0$ state (see section 5.2.4), but this would also reduce the signal by 80%. As a result, other methods were explored to direct the atoms from the trap to the detector, without being strongly affected by the experiment's magnetic field.

3.6 Push beam

The push beam is equivalent to a single additional MOT beam. This creates an unbalanced accelerating force acting on the atoms in one direction. The interaction between the push beam and the atoms is determined by the laser intensity, frequency, polarisation and pulse length of the push beam.

While there are multiple parameters with which to control the resulting atomic beam velocity and spin polarisation, we aim to only use the controls which are the easiest to adjust and monitor. In order to decide which parameters to test and which to keep constant, we consider how precisely and accurately we can measure the small incremental changes in the parameter as we adjust it. For example, measuring the push beam power density is done using a power meter placed in the path of the beam. The power is adjusted using power density filters, which limits the number and size of power increments. Additionally, the power would need to be regularly monitored using a power meter which is more disruptive than measuring one of the other parameters. The push beam frequency (controlled via the acousto-optic modulator and measured precisely using an RF meter) or the pulse length (set with high precision using a TTL pulse generator) can both be constantly monitored without blocking the beam.

The push beam power density was measured once and maintained above the saturation level for metastable argon ($1.4\,\mathrm{mWmm^{-2}}$), while the push beam pulse length, frequency and polarisation was adjusted to control the beam's average velocity and velocity distribution. The initial push beam tests focussed around controlling the atomic velocity. However, given that that a right or left circular photon polarisation will pump the atoms to either the $m = -2$ or $+2$ state respectively, the spin polarisation of the atomic beam could also be controlled. This became very useful for later experiments, since the spin-state interferometer initially requires a spin polarised atomic beam. This is discussed in chapter 3.6.4

The push beam alignment was adjusted using mirrors, with a camera focussed on each collimation slit to monitor the alignment. The transmitted laser light diffracts after the first slit and this diffraction reduces the precision with which one can discern the centre of the push beam on the second slit. It becomes increasingly difficult to align the push beam for a narrower transverse velocity selection, due to the requirement for narrower slit. For the beam to be properly aligned, it should pass through the centre of 2 slits and then hit the centre of the detector. In reality it was very difficult to make sure these three components were perfectly aligned, as a result the push beam could either be well aligned through both slits, but then not hit the centre of the detector, or it may hit the centre of the detector, but not transmitted efficiently through the two slits. In this case, the profile of the atomic beam on the MCP detector would not be symmetrical. To help with alignment, particularly for the narrower slits, a vacuum compatible piezo stage was introduced to move the 2nd slit in steps of 10nm. This was only necessary when using a 25 μm or less, second collimation slit.

3.6.1 Pulse length

The push beam pulse length was controlled by a TTL pulse sent to a switch on an RF circuit. The RF signal feeds into acousto-optic modulator, shown as AOM3 in figure 3.4. Since the push beam is taken from the 1st order diffracted beam from AOM3, switching the input RF signal also switches the push beam on and off with durations as low as 30 ns.

The majority of the push beam testing was done without any collimation slits unless stated otherwise. Without the collimation slits, the signal intensity is very large and reduces the necessary acquisition time.

The TTL pulse, which starts the push beam, is synchronised with the TTL pulse which turns off the cooling beams. The atoms begin to see the push beam at the same moment they stop being radiated by the cooling beams. If the atoms experience a significant delay between the turn-off of the trapping beams and the turn-on of the push beams, they rapidly disperse due to their thermal velocity spread and are lost from the push beam region. Even at low temperatures, this reduces the MOT density and hence the number of atoms that are pushed towards the detector.

A longer pulse length results in faster atoms and a narrower longitudinal velocity distribution. This changes with the introduction of the collimation slits because single slit diffraction reduces the laser power density by a factor of approximately 2 every millimetre below the slit. The 12 mm MOT-first slit distance therefore gives an upper limit to how long the push beam will significantly interact with the atoms. This problem also determines how effectively

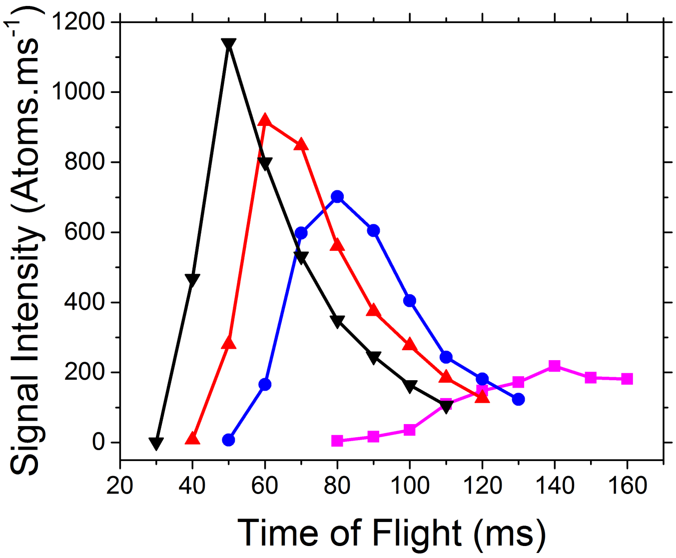

Figure 3.12: The distribution of TOF taken for the atoms to reach the detector for push beam pulse lengths of 7ms (black), 4 ms (red), 5ms (blue) and 2ms (magenta). A low power push beam was used, so even for the longest pulses, the average TOF is only approximately 45 ms.

the atoms can be spin polarised by the push beam. When working without the slits, the spin polarisation occurs easily due to the much longer interaction times. The extra interaction time makes up for any losses from detuning or polarisation which has not been optimised. However, since the final experiment has the 1st slit 12 mm below the chamber centre, we disregard this idea and work with a push beam that stops interacting 12 mm below the MOT.

3.6.2 Frequency & magnetic field effects

Understanding the effect of the push beam frequency on velocity, velocity spread and atom polarisation is a little more complicated than the pulse length since the atom's transition frequency also depends on the magnetic field present. The effect of the magnetic field and frequency need to be considered together.

Consider a change in the push beam frequency such that it is shifted away from the atom's cooling transition frequency (increasing the 'detuning' of the push beam). The laser-atom interaction strength will decrease. If a magnetic field is then introduced, the transition frequency will be shifted as $\Delta E \propto B$. In a spatially varying magnetic field, as in the MOT coils, the interaction with the push beam will be dependent the atom's position. The maximum interaction strength will occur when the frequency of the photons matches the shifted absorption frequency of the atom. Therefore, in some cases, detuning the push beam frequency can increase the accelerating force of the push beam.

For the push beam and the MOT, the length over which the interaction takes place, will depend on the the laser frequency and the field from the AH coils, which Zeeman shifts the atomic cooling transition frequency. Therefore, there can be a maximum interaction strength at zero, high or low detuning, depending on the magnetic field strength present. Figure 3.13 shows the effect of changing the push beam frequency on the atomic velocity, for a AH coil current of 5 A and hence a fixed magnetic field gradient.

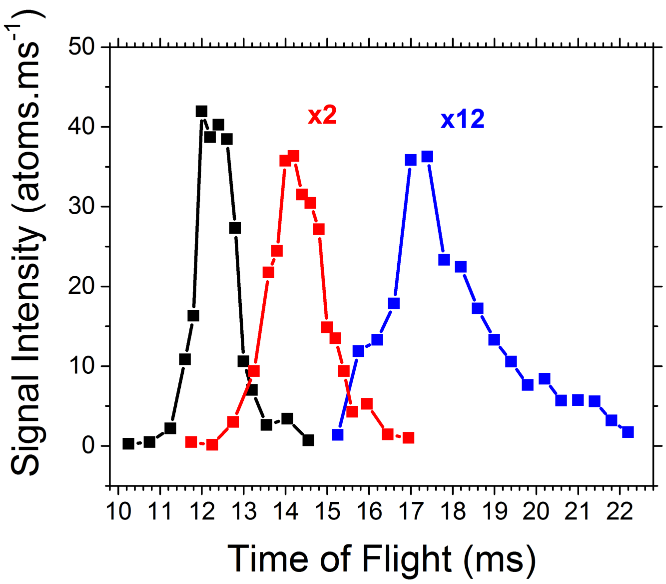

Figure 3.13: The distribution of time taken for the atoms to reach the detector, hence the atomic velocity distribution, for detunings of 2.4 MHz (blue), 3.2 MHz (red) and 6.4 MHz (black). Here, the scaling factor of the peak heights are shown.

When the push beam frequency is close to the resonant frequency, for example $\Delta = 2\,\mathrm{MHz}$, the atoms in the trap receive a strong momentum kick in the direction of the push beam. As they fall downwards, they enter a stronger magnetic field from the AH coils. The coils Zeeman shift the atomic energy levels and, as a result, the resonant frequency of the cooling transition is shifted away from the frequency of the beam. If the frequency is blue detuned from resonance, the push beam can still weakly interact with the atoms enough to give them an initial kick away from the trap centre. As they travel further into the stronger magnetic field region, the field keeps the atom's transition frequency close to the Doppler shifting laser frequency. This increases the overall interaction time and hence increases the average velocity and observed signal. If the detuning is taken too far from resonance, for example $\Delta = 40\,\mathrm{MHz}$, the atoms require an even larger magnetic field to maintain the atom-laser interaction. There is very little momentum imparted to the atoms from the laser in the central trapping region. In this region the magnetic field strength is low and the atomic transition frequency is not shifted enough to match the laser. In this case only atoms that reach the highest areas of magnetic field strength (through their own thermal velocity), while staying in the line of sight of the push beam, will continue to interact with the push beam and eventually reach the detector.

The Doppler shift of the laser frequency that the atoms experience as a result of travelling away from the push beam must also be considered. This is similar to the magnetic field in that a small detuning gives a good initial kick, but is less effective as the atom speeds up. Again, if the detuning is larger, there is less of an initial kick but more interaction when the atom speeds up.

The final experiment uses 3 very weak magnetic fields, for interferometry and the weak measurement. Therefore it seemed sensible to turn off the AH coils as soon as possible in the push cycle, to avoid the strong AH coils field interfering with the other weaker fields. As a result, the total background magnetic field, originating predominantly from the compensation cube, is of the order of 50 μT. At these field strengths the Zeeman shift is much lower compared with the Zeeman shift induced from the AH coils field. In the case of turning the AH coils off, the range of control of the velocity via frequency detuning is reduced, but not eliminated. The optimal choice of frequency for pushing and for atomic beam polarisation is detailed in section 3.6.4.

3.6.3 Transverse Coherence

The transverse coherence of the atomic beam determines the contrast of the interference fringes seen when the beam passes through a multi-slit grating. As described in section 2.1.2, the atomic velocity, source size and the source to grating distance determines the transverse coherence. Due to the need for a long grating to detector distance, in order to spatially resolve the fringes, the distance between the source and the grating was limited to approximately 50 mm. The source size was then minimised to optimise the transverse coherence.

The source size (diameter of the MOT) can be reduced by increasing the trap's magnetic field strength. This will reduce the overall number of atoms per push cycle and the average atomic beam width would be increased by any small changes in the MOT position. A more robust solution is to place a slit immediately below the MOT. The slit was positioned 17 mm beneath the MOT, which was as close as possible without the slit material blocking the MOT cooling beams. A quartz slide with a hole in the centre, shown in figure 3.14, was used to hold the slit secured using Kapton tape. This slit now defines the source size and hence the transverse coherence length. For atoms travelling at $12\,\mathrm{ms}^{-1}$, a 10 μm wide slit gives a transverse coherence length of 1.8×10^{-6}m which would cover ≈ 7 slits of the grating.

This should be sufficient to observe interference fringes providing the coherence length occupies enough of the beam width. To minimise the beam

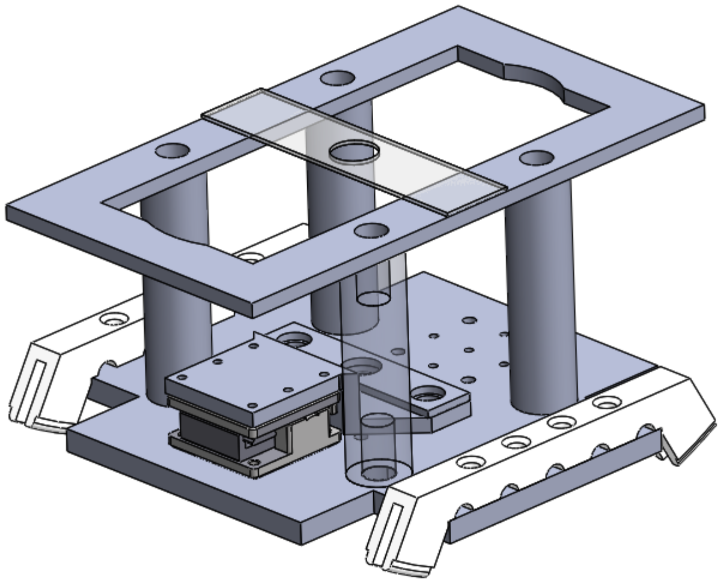

Figure 3.14: A CAD drawing of the slit housing. The nearest of the 4 pillars holding up the top plate is made transparent to show the holding plate for the 2nd collimation slit. In this particular configuration, the second slit would be precisely positioned using the piezo stage seen next to the translucent pillar.

width further and ensure the degree of coherence is good, a second collimation slit was introduced. To calculate what proportion of the atomic beam will be coherent at the grating, we look at the beam divergence angle given by

$$\theta_d = 2\tan^{-1}\left[\frac{w_s + w_{s2}}{2L_{ss}}\right] \tag{3.3}$$

where w_s/w_{s2} are the widths of the 1st slit and the 2nd slit, while L_{ss} is the distance between the 1st slit and the 2nd slit. For a combination of a 10 µm slit and a 50 µm slit, the width of the signal when it reaches the grating is $\approx$ 73 µm making the transverse coherence length 2% of the total signal width. This is likely to produce observable fringes, albeit with poor contrast.

The collimation slits were fitted to the experiment on a purpose built slit housing frame, figure 3.14. The slits were laser cut into 12 µm thick molybdenum foil and clamped or stuck onto aluminium plates which fit onto the frame. The range of atomic transverse velocities is selected by collimating the beam using this apparatus. The resulting atomic beam width at the detector is shown in figure 3.15. The width of the prominent peak is determined by the combination of collimating slits used (10 µm and 50 µm, separated by 30 mm). Significantly, the width of this peak is unaffected by the velocity of the atoms. It is useful to know the width when modelling the contrast of the interference fringes in matter-wave interferometry. Therefore, the transverse velocity range that is selected, v_x, depends on the TOF velocity v_z. From this data we measure $v_x = \pm 0.027\,\mathrm{ms^{-1}}$ for $v_z = 11\,\mathrm{ms^{-1}}$, $v_x = \pm 0.020\,\mathrm{ms^{-1}}$ for $v_z = 15\,\mathrm{ms^{-1}}$ and $v_x = \pm 0.017\,\mathrm{ms^{-1}}$ for $v_z = 18\,\mathrm{ms^{-1}}$.

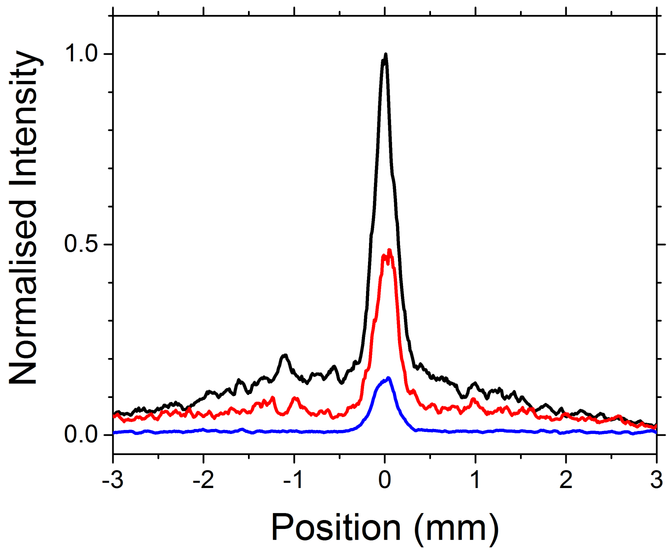

Figure 3.15: Measured atomic beam width profile for the three velocities that are used for the matter-wave interferometry (approximately $11\,\mathrm{ms^{-1}}$ (blue), $15\,\mathrm{ms^{-1}}$ (red) and $18\,\mathrm{ms^{-1}}$ (black)). This beam width was narrowed using a 10 µm slit and a 50 µm for the initial and second collimating slit respectively.

The wider, less intense peak which appears as a background signal is a result of scattering off the collimating slit walls and thus the properties of this background peak are affected by the thickness of the foil used for the collimating slit.

3.6.4 Spin polarisation

The absorption and emission of photons that happens during the acceleration of the atom by the push beam can, under certain conditions, spin polarise the atoms to either stretched state, $m = 2$ or $m = -2$, depending on the laser polarisation and the magnetic field direction. While the atoms are in the MOT, they are cycling between the m states since they are constantly being radiated by both right and left circularly polarised photons, as shown in figures 3.3 and 3.16.

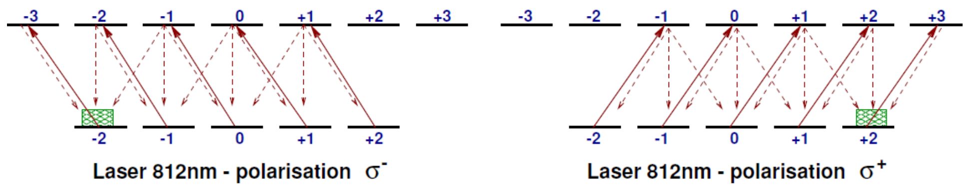

Figure 3.16: Possible state transitions between the $4s[3/2]_2$ and the $4p[5/2]_3$ energy levels for Ar* when radiated with either right σ^+ or left σ^- circular polarisation. The atoms in the MOT are illuminated by both types of light, therefore, while in the trap, atoms are constantly being pumped between all states.

The push beam is switched on at the same time that the MOT cooling beams are switched off. If the push beam is set at right circular polarisation, σ^+, or left circular polarisation, σ^-, relative to the atoms quantisation axis, the atoms are pumped towards a stretched state, $m = 2$ or $m = -2$, respectively. The quantisation axis of the atoms is set by the external magnetic field. In this case, the field is a quadrupole field created by the anti-Helmholtz MOT coils. This conveniently creates a central column of approximately uniform field direction, at least across the width of the atomic beam, from the centre of the chamber outwards.

The polarisation of the atomic beam was tested using a Stern-Gerlach (SG) wire, which is discussed in more detail in section 5.2.4. The magnetic field induced by a current in the wire imparts a spin-state dependent force on the atomic beam. The five m states arrive at different locations on the detector

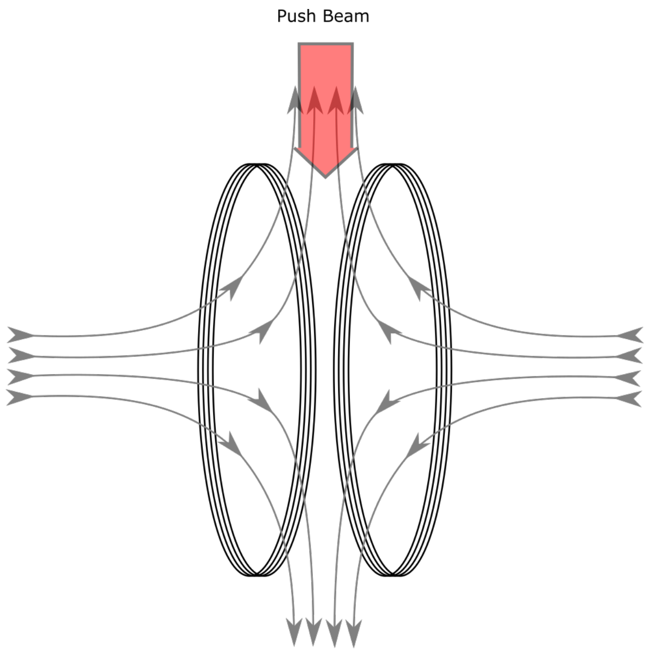

Figure 3.17: Approximate field directions around an anti-Helmholtz coil pair. The field direction is approximately constant when moving from the centre outwards, along the x or z axis.

and the relative areas of each signal peak effectively indicate the polarisation of the atomic beam. To ensure adjacent peaks are resolvable, the deflection of the atoms is maximised by positioning the wire at the bottom of the slit housing, 150 mm from the detector, as shown in 3.18.

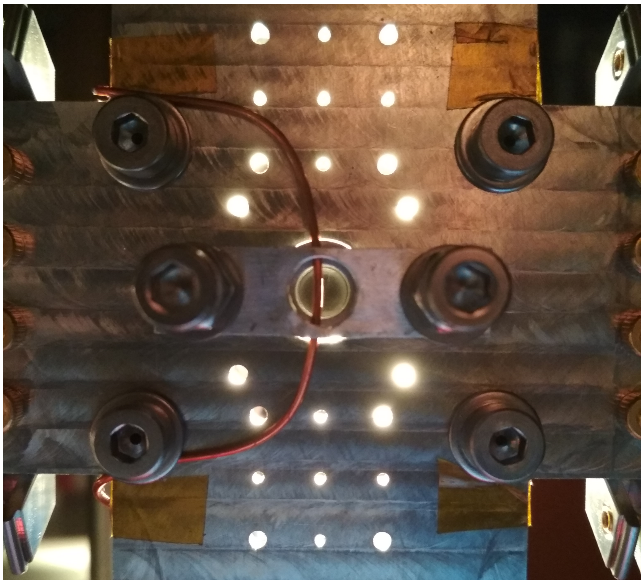

Figure 3.18: View of the SG wire positioned be 150 mm above the detector when installed. The second collimation slit is visible behind the wire.

The push beam laser is initially linearly polarised and passes through a quarter-wave plate which transforms the polarisation to left or right circular polarisation (σ^- or σ^+) when rotated 45° or -45° from the vertical axis. As a result, we see an atomic beam polarisation of $m = -2$, for σ^- light polarisation and $m = 2$, for σ^+ light. When the wave-plate kept at 0°, the push beam remains linearly polarised (π) and we see a mixture of $m = 0, \pm 1, \pm 2$ in the atomic beam. This control of the atomic beam polarisation is shown in figure 3.19, where the pulse length of the push beam is set at 0.6 ms and the detuning at 15 MHz. If there is not sufficient push beam interaction time or interaction strength, the push beam will not successfully spin polarise the atomic beam.

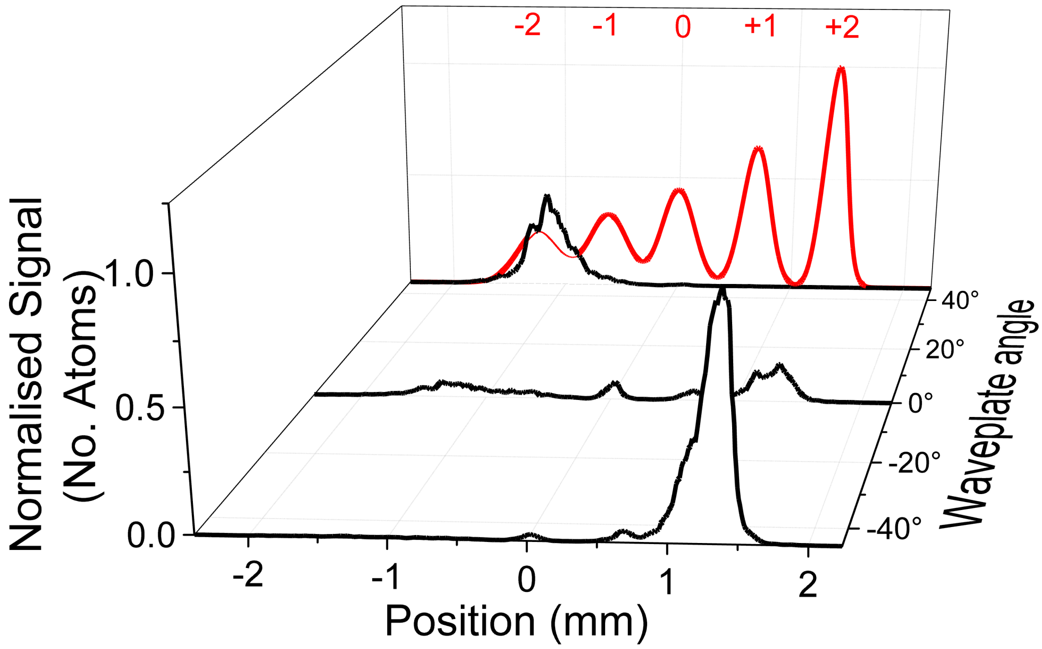

Figure 3.19: The atom signal after being pushed past the SG wire, which spatially separates the m states. The push beam is circularly polarised using a $\frac{\lambda}{4}$ waveplate. When set to 0°, the light is a linearly polarised, at 45° and $-45°$ it is σ^+ and σ^-. Simulated peak positions are shown in red.

This description of the tunable, cold atomic beam provides an initial step towards estimating the atomic velocity, which has a direct effect on the atom's de Broglie wavelength. This defines the contrast and separation of the matter-wave interference fringes, which can then be used to further characterise the beam.

3.7 Conclusions

This chapter has demonstrated the production of a low velocity and tuneable atomic beam. The beam was formed by applying radiation pressure in a push beam to a MOT. The atom's position and TOF were then observed on a micro-channel plate detector below.

The range of the longitudinal velocities that can be produced was shown to be $1 - 52\,\mathrm{ms}^{-1}$. The velocities could be controlled primarily by adjusting the detuning frequency of the push beam. However, the push beam pulse length and beam power could also be used. Transverse velocities were selected using 2 collimation slits and were shown to be between $0.017 - 0.027\,\mathrm{ms}^{-1}$ for longitudinal velocities of $18 - 11\,\mathrm{ms}^{-1}$. The cooling transition used by the laser to accelerate the atoms also spin polarises the atoms in the beam. An atomic beam of $m = 2$ or $m = -2$ atoms with high purity was produced.

The beam's transverse coherence was sufficient to perform matter-wave interferometry using a multi-slit grating, while the atom's spin polarisation provided a suitable beam for a longitudinal Stern-Gerlach interferometer.

Chapter 4

A multi-slit matter-wave interferometer for metastable argon atoms

4.1 Introduction

This chapter describes the construction of the matter-wave interferometer which utilises the velocity-tunable atomic beam described in chapter 3. This interferometer is one component of the weak measurement of transverse momentum, but it was also used to characterise the velocity of the atomic beam with greater detail than typical time-of-flight (TOF) methods.

Matter-wave interferometry with atomic beams typically involve coherently manipulating the motion of the atoms to simultaneously create two or more paths such that when the paths recombine the difference in path length results in a phase shift in the atom's spatial wavefunction. It has been shown that the atom's centre-of-mass motion can be efficiently manipulated through momentum kicks from photon interactions in a Ramsey-Borddé interferometer. Here, momentum transfer from photon absorption places the atom in a superposition of two momentum states and two internal states [55].

Alternatively, diffractive interferometers, which are closely analogous to optical diffraction through a material slit, put the atom's centre-of-mass in a spatial superposition without any changes to the internal states. This type of interferometer allows subsequent manipulation of the spin states which is more conducive to making a weak measurement of momentum using the spin states of atoms. Importantly, it is exactly analogous to the Kocsis experiment [30] with which we wish to compare our results. In diffractive interferometers, a nanostructured, material mask or a standing light wave (Kapitza-Dirac interferometer) is used to diffract the atoms. A standing wave can act in the same way as a material grating by prohibiting certain paths of the atom between the source and the detector. This can be achieved with the optical dipole force used to channel [13] or scatter [57] the atoms. It can also be achieved by quenching [56] or ionising [14] such that the atoms do not interact with detector.

Unlike that of material slits, an optical grating which uses channelling has a much higher transmission efficiency, since all the incoming atoms are diffracted. However, the choice of optical grating width and separation is limited to the range of accessible laser wavelengths that will interact with the atoms. In addition, optical gratings also require other equipment to monitor the state of the standing wave. In contrast, material nanostructured gratings are small, stand-alone, stable objects which are much simpler to implement. Additionally, a wider range of slit geometries can be used which provide a greater flexibility to the experiment design. The stability, size and ease-of-use of the material gratings compensates for the problematic atom-surface interactions and reduced transmission efficiency and so we decided to implement them in this work.

Material masks have been successfully used in matter-wave interferometers using both double [15] and multi-slit gratings. The number of paths determines the total throughput of the interferometer, but more paths increases the need for a narrow transverse velocity selection in order to achieve sufficient interference fringe contrast. The narrow velocity selection of the atomic beam can impose enormous constraints on the throughput, in which case, a set of gratings in a Talbot-Lau configuration [58] can be used instead. This removes the need for the initial narrow transverse velocity selection, but limits the applicability to the near field regime, which does not leave enough space to design a weak measurement using a magnetic field based spin-state interferometer.

In this project, the interferometer must be able to spatially resolve interference fringes using an atomic beam $\approx 200\,\mathrm{mm}$ long, while leaving enough space between the grating and the detector to implement a spin-state interferometer. We therefore decided to use conventional diffractive interferometer using a single nanostructured mask.

4.2 Constructing the interferometer

The required slit separation of the grating depends on the necessary interference fringe separation for the particular experiment. The fringe separation is determined by the atomic momentum, mv, and the distance between the grating and the detector, L_{gd}. In our case L_{gd} is limited to $\approx 0.15\,\mathrm{m}$. The detector's ultimate resolution is $\approx 12\,\mu\mathrm{m}$, meaning that for a perfectly optimised experiment, the interference fringes would need to be separated by a minimum of $24\,\mu\mathrm{m}$ to be resolved on the detector. In reality, to account for poor beam coherence while the equipment is being initially optimised, the fringe separation needs to be at least 5 times higher than this. The fringe separation for a matter-wave Δx, is

$$\Delta x = \frac{h}{mv}\frac{L_{gd}}{d} \tag{4.1}$$

where d is the grating period, h is Planck's constant and m is the atomic mass. The velocity range of the atomic beam is $1 - 52\,\mathrm{ms}^{-1}$, so to achieve a fringe separation of at least $120\,\mu\mathrm{m}$, the grating period must be at narrower than

186 nm for an atomic velocity of 52 ms^{-1}, 466 nm for an atomic velocity of 21 ms^{-1} and 4656 nm for 2 ms^{-1}.

The etching resolution of laser micro machining only reaches as low as $\approx$ 3µm due to the limitations of the objectives that focus the laser. To machine below such lengths, techniques such as focussed ion beam etching and optical or electron lithography must be used, at a much greater financial cost.

4.2.1 A Si_3N_4 diffraction grating

We obtained two Si_3N_4 gratings from Prof. Markus Arndt of the University of Vienna. Records from the batch fabrication indicate that the grating structure has a periodicity of 257 nm and a slit width of 90 nm. The grating has a cross bar support structure where the cross bars are spaced $\approx$ 1.5µm apart. The structure gives the grating an open fraction of 66% parallel to the slits and 38% orthogonal to the slits. The overall transmission is therefore 25%. The profile of the grating bars was described by the supplier as having a thickness, t, of 160 µm and a wedge angle, β of 7° as shown in figure 4.1

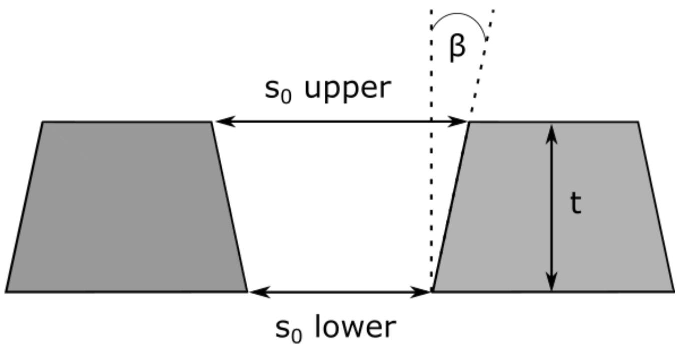

Figure 4.1: Diagram showing the profile of the slits. This indicates that the given slit width of 90 nm is probably an average value of the top and bottom slit widths.

SEM images of the grating slits are shown in figure 4.2. They were used to confirm the given dimensions of the slits. The pixel calibration, which indicates the length in the focus plane that one pixel of the SEM image observes (shown in the bottom left corner of each image) is used to extract the necessary dimensions. While the slit width and slit separation could be directly measured from the image, the profile dimensions could not. Instead, this measurement was made by measuring the slit width from above the grating 'looking down', s_u, and below the grating 'looking up', s_l. This gives the thickness of the grating if the wedge angle is known or vice versa. The image measurements are based on the microscope calibration which could not be validated. It was also difficult to know if the plane of the grating and the microscope beam axis are sufficiently perpendicular. The slit separation was measured as d =252 nm, however if the calibration is taken to be incorrect, then comparing the measured width with the manufacturer's value $d = 257.4$ nm provides a ratio which with to calibrate other measurements. In this case, t was measured to be 132.5 nm assuming $\beta = 7°$, or assuming $t = 160$ nm, $\beta = 5.8°$.

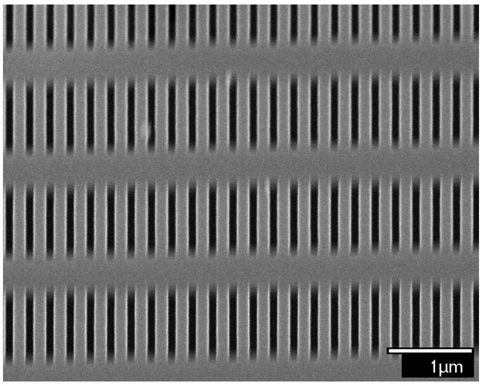

(a)

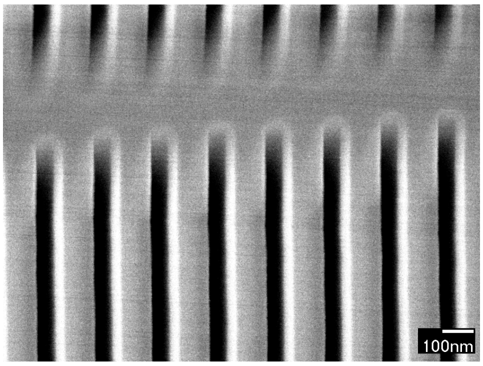

(b)

Figure 4.2: SEM images of the grating slits (a) a wide angle view showing the aspect ratio of the slits (b) close angle and tilted to give an idea of the thickness of the grating.

The grating covers a 5×5 mm window within a 10×10 mm frame of 1 mm thickness. The frame is fixed to the slit housing as shown in figure 4.3(a) and sandwiched between two aluminium plates. The orientation of the grating is optimised using a 633 nm HeNe laser on a benchtop.

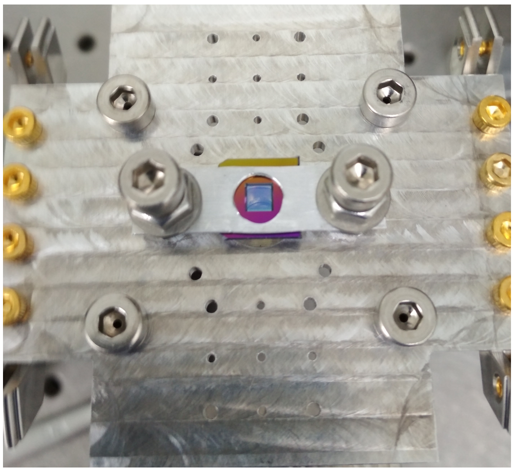

(a)

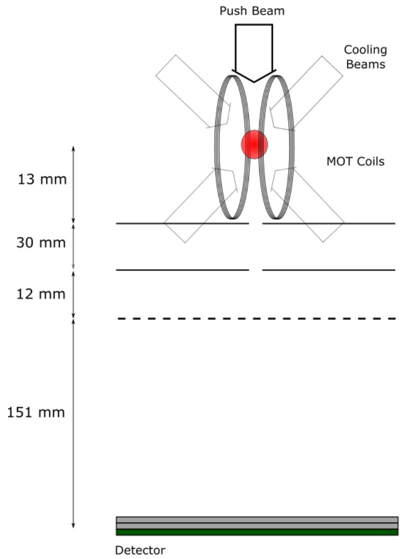

(b)

Figure 4.3: (a) An image of the grating that was used fitted to the underside of the slit housing. (b) A schematic of the full experimental setup including the push beam source (the MOT) and the transverse velocity selection via 2 collimation slits as well as the grating itself.

4.3 Interference using a multi-slit Si_3N_4 grating

4.3.1 Fringe contrast

The observed interference pattern created by a source of width, w_s, can be considered to be a combination of interference patterns from a number of point sources positioned across the extent of w_s. To describe the pattern from a point source, consider a plane wave of wavenumber $k(v) = \frac{2\pi}{\lambda_{DB}(v)}$, incident on a grating of N slits. The signal intensity, I_0, as a function of transverse position, x, and atomic velocity, v, observed at the detector is given by [46]

$$I_0(x, v) = \left(\frac{\sin(\frac{1}{2} N\, k(v)\, d\, \sin(\frac{x}{L_{gd}}))}{\sin(\frac{1}{2}\, k(v)\, d\, \sin(\frac{x}{L_{gd}}))} \right)^2 |f_{slit}(x, v)|^2. \tag{4.2}$$

The signal is a product of a grating function (1st term) and a slit function (second term). The grating function describes the interference pattern, while the slit function describes single slit diffraction, hence the envelope of the pattern. The slit function is derived from the description of the diffracted wavefunction due to Huygens principle and also accounts for the interaction between the atoms and the slit walls [46]. For a slit width, s, we have

$$f_{slit}(x,v) = \frac{2\cos(\frac{x}{L_{gd}})}{\sqrt{\lambda(v)}} \int_0^{\frac{s}{2}} d\zeta \cos\left[k(v)\ \sin(\frac{x}{L_{gd}})(\frac{s}{2}-\zeta)\right]\tau(\zeta,v) \qquad (4.3)$$

where L_{gd} is the distance between the grating and the detector, τ is the transmission function for a single slit (equation 4.8) and ζ is the transverse position across the width of the slit. Equation 4.2 describes the interference pattern for a point source positioned at $x = 0$ in the transverse plane. This is shown in figure 4.4 for the dimensions used in this experiment, where $s = 90\,\text{nm}$, $d = 257\,\text{nm}$, $L_{sg} = 0.156\,\text{m}$, and $v = 12\,\text{ms}^{-1}$. The number of slits illuminated by the atomic beam is chosen as $N = 30$. In the experiment the number is ≈ 180. However, with this value the fringes are too narrow to be clearly seen for the available resolution of the position axis.

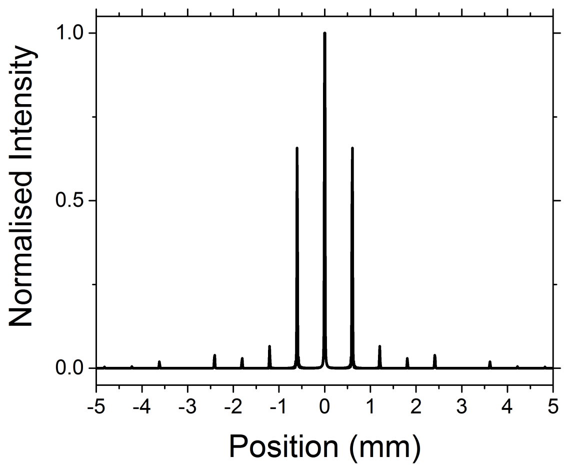

Figure 4.4: The calculated interference pattern for a point source positioned at $x = 0$ transmitted through 30 slits.

We develop this model to describe the full extent of the source, by considering the possible paths an atom can take from any point on the source to the detector. These paths are dependent on the transverse velocity selection of the atomic beam. For a non point-like initial thermal source, the transverse velocity distribution is generally too wide to achieve sufficient coherence and resolve the interference fringes, so we introduce two collimation slits before the grating as shown in figure 4.5.

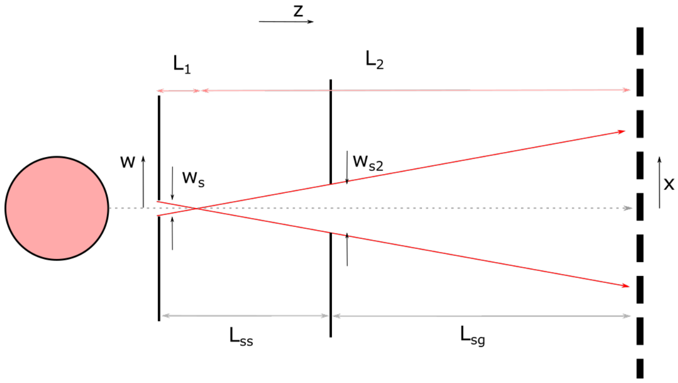

Figure 4.5: The extent of the possible paths for an atom travelling between the source and the grating, via two collimation slits. This assumes negligible diffraction through the slits. L_{ss} is the distance between the two collimation slits and L_{sg} is the distance between the last slit and the grating. w_s is the width of the source (the 1st slit) and w_{s2} is the width of the second slit.

If the probability density at the detector is $I_0(x_c, v)$, for a point source positioned in the centre of the actual source distribution is x_c $(x = 0)$, then the overall pattern, $I(x, v)$, as a result of the distribution of point sources across the actual source width, w_s is given by

$$I(x,v) = \int_{-w_s/2}^{w_s/2} dw I_0(x_c + \Delta x(w), v) \tag{4.4}$$

where $\Delta x(w)$ is the shift in the centre of the interference pattern for each position of the point source. For a two collimation slit configuration as used in this experiment, the shift is given by

$$\Delta x(w) = \frac{w}{2} \frac{L_{sd} + \frac{w_{s2} L_{ss}}{w_s + w_{s2}}}{L_{ss} - \frac{w_{s2} L_{ss}}{w_s + w_{s2}}} \tag{4.5}$$

which produces the signal seen in figure 4.6.

Since the source intensity varies across its width, a suitable function $A(x, w)$ is included which describes the source intensity distribution that is seen at the detector as seen experimentally in figure 3.15. In this example a simple

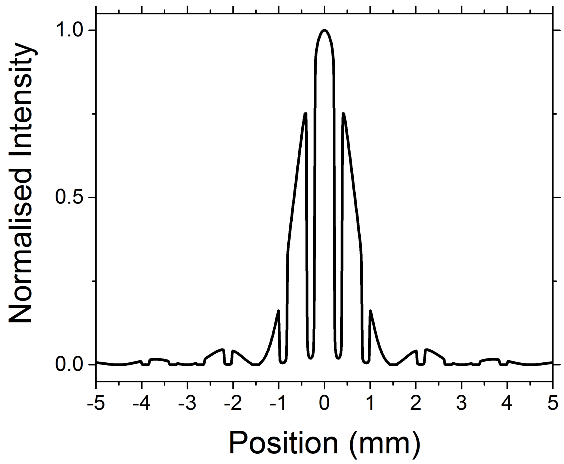

Figure 4.6: The calculated interference pattern for a source of a finite width and two collimation slits of width w_s and w_{s2}.

Gaussian curve is used. The intensity is now given by a convolution of $I(x, v)$ with $A(x, w)$.

$$I(x, v) = \int_{-w_s/2}^{w_s/2} dw A(x, w) I_0(x_c + \Delta x(w), v). \tag{4.6}$$

The initial function shown in figure 4.6 (equation 4.2), convolved with $A(x, w)$ is shown in figure 4.7

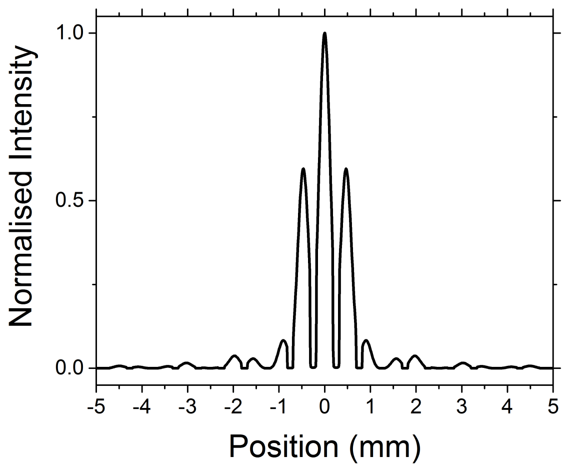

Figure 4.7: The calculated interference pattern for a collimated source which has a spatially dependent intensity described by $A(x, w)$.

The previous plots are for a single value of v. In reality, atoms from a range of longitudinal velocities, Δv, are being detected across the chosen detector exposure time. The distribution of the longitudinal velocity, or the temporal coherence is incorporated into the model by integrating the interference pattern over the longitudinal velocity spread that is acquired during the detector's exposure time. This is shown in figure 4.8 and the signal is now given by

$$I(x, v) = \int_{-\Delta v/2}^{\Delta v/2} I(x, v) dv. \tag{4.7}$$

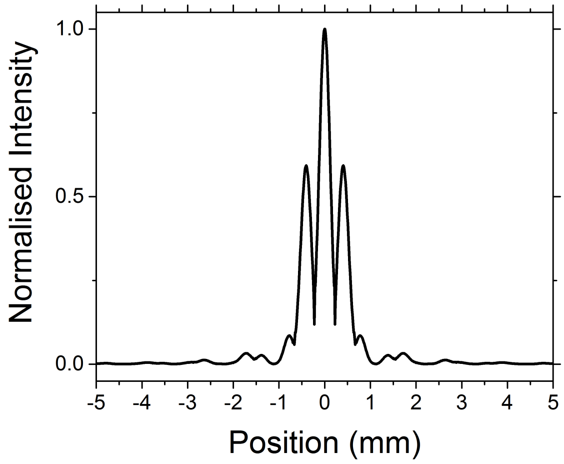

Figure 4.8: Interference pattern for a range of longitudinal velocities, from a collimated source which has a spatially dependent intensity described by $A(x, w)$.

4.3.2 The effects of Van der Waals interactions on diffraction

As the atoms pass through the slits of the grating, the Van der Waals (VdW) potential between the Si_3N_4 grating and the atoms can influence the motion of the atom and effect the interference pattern. The potential is given by $V_{VdW} = C_3/l^3$, where l is the distance between the atoms and C_3 is the strength of the interaction. The interaction strength is dependent on the grating material and the type of atom used for diffraction. This is an attractive force with causes further divergence of the atomic beam after passing through the grating slit.

The VdW interaction changes the slit function which is observed as a change in the envelope of the diffraction pattern. This change was used to determine C_3 more accurately than previous measurements [46, 47]. The increased polarizability of metastable atoms means that the VdW constant C_3 is much larger compared to that of ground state atoms, which has been shown previously for helium and neon [48]. In an experiment with a metastable argon beam diffracting from a nanometer scale Si_3N_4 grating, the resultant slit function was compared with calculated C_3 values [49].

To include the effects of the VdW interaction, the overall slit function, given by equation 4.3, is now modified [46] so that

$$\tau(\zeta, v) = \exp\left[i\frac{t\cos\beta}{\hbar v}\frac{C_3}{\zeta^3}\frac{1+\frac{t}{2\zeta}\tan\beta}{(1+\frac{t}{\zeta}\tan\beta)^2}\right] \tag{4.8}$$

where t is the thickness and β the wedge angle. This interaction effectively reduces the slit width as C_3 increases and modifies the envelope of the interference pattern. The envelope is shown in figure 4.9 when using a Si_3N_4 grating with atoms at $11\,\mathrm{ms}^{-1}$. The slit function that is used to model the expected interference pattern is then given by equation 4.7 with the C_3 modified slit function and the grating function taken from previous work [46]. For the source intensity distribution, $A(x, w)$, we use a Gaussian peak fitted to the observed source image (the signal without the grating) at the detector. The resulting equation is evaluated numerically using the trapezoidal method.

4.3.3 Other factors affecting the interference pattern

There are a number of other factors that can affect the shape and intensity of the interference pattern. We have chosen to omit them here as their effect is negligible when included in the modelling of the interference pattern. This includes;

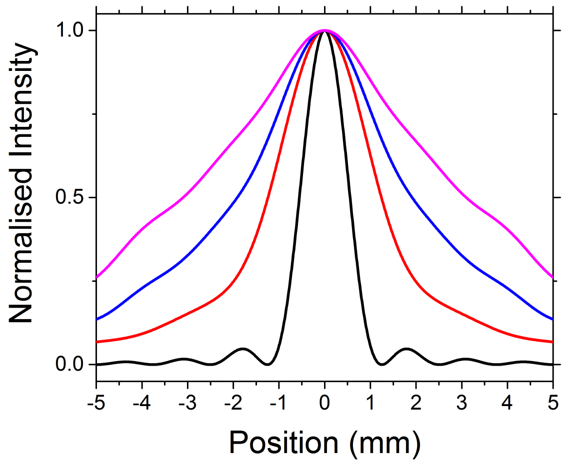

Figure 4.9: The effect of the VdW coefficient on the diffraction pattern. The data shows the slit function equation 4.3 for $C_3 = 0$ (black), $C_3 = 0.78\,\mathrm{a.u.}$ (red), $C_3 = 1.55\,\mathrm{a.u.}$ (blue), $C_3 = 2.33\,\mathrm{a.u.}$ (magenta).

- Slit disorder. This is a variation in the width of the slits which causes a decrease of the relative peak height of the higher order interference fringes. The disorder can also differ between the leading edge of the slits and the trailing edge. A difference in the disorder between the leading and trailing edge causes an asymmetric slit function [46]

- Disorder in grating periodicity. This is a variation in the centre to centre separation of the slits. This also causes a decrease in the relative peak height.

- Surface roughness. A variation in the surface roughness averages to an equivalent slit width disorder and so is an additional decrease of the relative peak heights for higher order peaks.

- Scatter. Atoms that collide with the slit walls and are elastically scattered gaining a new transverse momentum. This creates an incoherent background underneath the interference fringe pattern

4.4 Spatial matter-wave interference of Ar* atoms

The atoms in a magneto-optical trap are accelerated by radiation pressure, towards the detector to create a cold atomic beam, as described in the last chapter. Positioned 17 mm below the MOT is a 10 μm wide collimation slit. A further 30 mm below is a 50 μm wide collimation slit. Both slits ensure that only atoms with very low (negligible) transverse velocities reach the multi-slit, Si_3N_4 grating, placed 59 mm below the MOT and 147 mm from the detector. This arrangement is shown in figure 4.3(b). The atoms diffract through the slits and create an interference pattern on the 2D detector below the grating.

The interference fringes were observed for a range of de Broglie wavelengths (determined by the atomic velocity). Data for one atomic velocity setting typically took around 360,000 push beam pulses, which at a pulse cycle length of 0.5 s equates to $\approx$ 50 hours of continuous data acquisition. The velocity of the atomic beam was measured using the interference fringe spacing and compared with the typically used TOF velocity measurement method. An estimate of the velocity can be determined from the TOF and is given by

$$v_{TOF} = \frac{s - \frac{1}{2}at^2}{t} + at \tag{4.9}$$

where t is the TOF and s is the source to detector distance which is measured as 206.5 ± 0.5 mm. This distance is taken from the CAD drawings from the centre of the MOT chamber to the face of the detector with an uncertainty due to the MOT position. The uncertainty in v_{TOF} is also due to the initial spatial and velocity spread of the atoms. The velocity spread, due to the MOT temperatures, is distributed further given the spread in the accelerating force of the push beam on the atoms.

Interference with a $v_{TOF} = 12\,\mathrm{ms}^{-1}$ atomic beam

For this experiment, the push beam was blue detuned by 4.76 MHz from resonance with a pulse length of 0.6 ms to remove the atoms from the trap. The velocity range was selected by setting the camera exposure to 1.5 ms beginning 17 ms after the atoms are pushed from the trap. Equation 4.9 gives the TOF velocity as $v_{TOF} = 11.72\,\mathrm{ms}^{-1}$ and TOF velocity distribution as $\Delta v_{TOF} = 0.49\,\mathrm{ms}^{-1}$. The interference fringes from this TOF velocity group are presented in figure 4.10. Equation 4.7 is fitted to match the fringe spacing

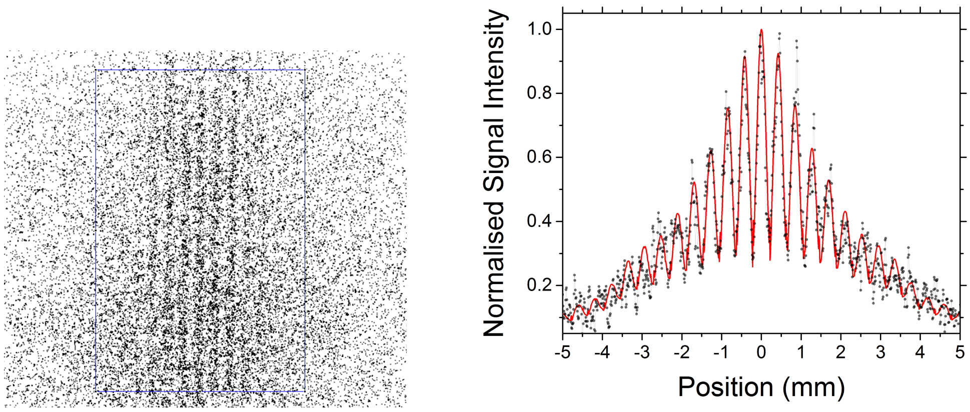

(a) (b)

Figure 4.10: (a) The detector image showing the average of 350,000 frames. For a TOF of 17.75 ± 0.75 ms and averaged 1 atom count for every 12 cycles. (b) The averaged profile of the blue boxed region in (a), the red line shows the modelled optical interference pattern for the same apparatus dimensions.

in figure 4.10. The fixed parameters are taken from the experimental setup described in this chapter. The number of slits N is now given as 181, which is the number of grating slits illuminated by the beam width. Fixed parameters N, m and $\hbar$ contribute with negligible uncertainty. Other fixed parameters such as distances L, d, slit and grating dimensions d, w, s, β, t and the longitudinal velocity spread Δv all have some associated uncertainty. However, for an initial simplified measurement the uncertainties were omitted. Only v is left as a free parameter for the software to fit. This gives a measurement of the average atomic velocity at the grating as $\bar{v} = 12.85 \pm 0.55\,\mathrm{ms}^{-1}$. The measurement is an average over the detector exposure time where the uncertainty in the parameter is calculated via a 'variance-covariance' matrix during the Levenberg-Marquardt fitting algorithm in OriginPro.

Interference with a $v_{TOF} = 14\,\mathrm{ms}^{-1}$ atomic beam

This experiment was adjusted to acquire a signal from a slightly faster set of atoms. The push beam pulse was blue detuned by 8.01 MHz from resonance, but the 0.6 ms pulse length was maintained. The camera was triggered 14 ms after the atoms were pushed from the trap and the exposure time was again 1.5 ms giving $v_{TOF} = 14.07\,\mathrm{ms}^{-1}$ and $\Delta v_{TOF} = 0.71\,\mathrm{ms}^{-1}$. The data is presented in figure 4.11. Again, equation 4.7 was fitted with the same conditions as the last velocity measurement to match the fringe spacing, giving $\bar{v} = 15.15 \pm 0.55\,\mathrm{ms}^{-1}$.

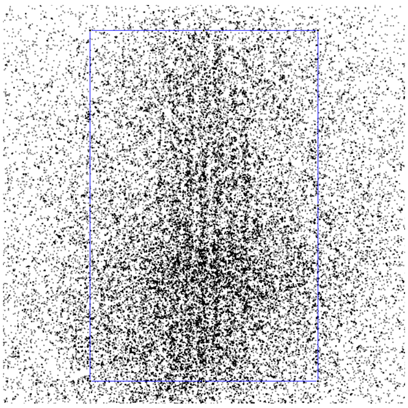

(a)

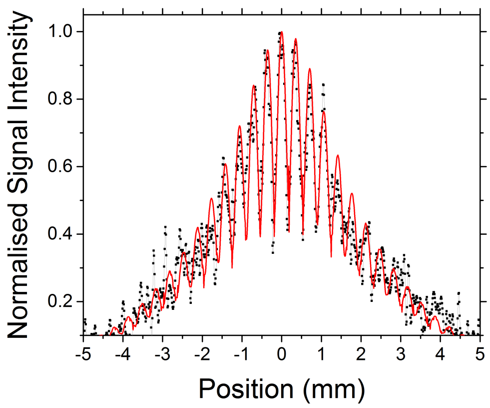

(b)

Figure 4.11: (a) The detector image showing the average of 350,000 frames. For a TOF of 14.75 ± 0.75 ms and averaged 1 atom count for every 13 frames. (b) The averaged profile of the blue boxed region in (a), the red line shows the modelled optical interference pattern for the same apparatus dimensions.

Interference with a $v_{TOF} = 17\,\mathrm{ms}^{-1}$ atomic beam

To complete this data set, the atomic velocity was increased again. The push beam was blue detuned by 11.31 MHz from resonance and a 0.6 ms duration push beam was again used. The camera exposure time was reduced to 0.8 ms and was triggered 12 ms after the atoms were pushed from the trap. This gives $v_{TOF} = 16.71\,\mathrm{ms}^{-1}$ and $\Delta v_{TOF} = 0.54\,\mathrm{ms}^{-1}$. Figure 4.12 shows the fringe contrast has significantly decreased as a result of a shorter de Broglie wavelength giving a less coherent beam. We can see the result of this in the larger uncertainty in the fit which gives the average atomic velocity at the grating as $\bar{v} = 18.65 \pm 1.15\,\mathrm{ms}^{-1}$.

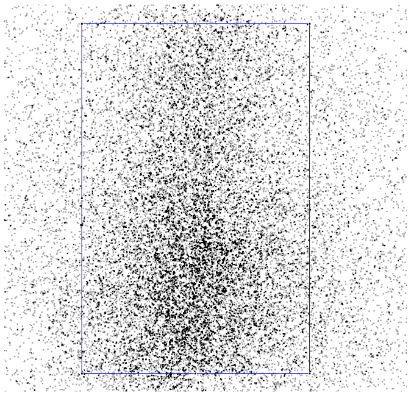

(a)

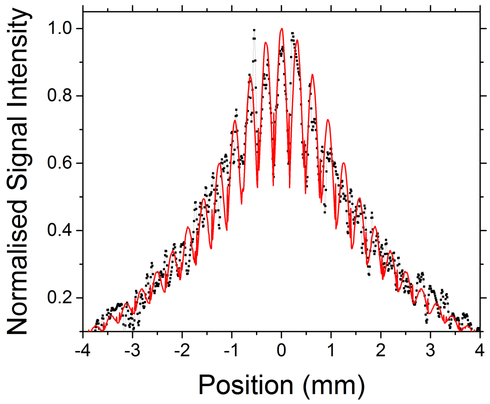

(b)

Figure 4.12: (a) The detector image showing the average of 350,000 frames. For a TOF of $12.4 \pm 0.4\,\mathrm{ms}$ and averaged 1 atom count for every 5 frames. (b) The averaged profile of the blue boxed region in (a), the red line shows the modelled optical interference pattern for the same apparatus dimensions.

Comparing the 3 data sets, we observe that the slower atoms have a longer de Broglie wavelength, which produces a wider interference fringe separation and increases the interference fringe contrast, as a result higher orders fringes are more visible. Averaging the ratio between the two velocity measurements across the data sets gives $v_{TOF} = 0.91\bar{v}$. The average uncertainty in $v_{TOF} = 2.4\%$ and in $\bar{v} = 4.7\%$. This shows the velocity measurement using the interference pattern gives a slightly higher value than the velocity measured using the TOF method.

This difference in the measured velocities is understandable given that the TOF method over simplifies the acceleration of the atomic beam. The acceleration of the atomic beam is not well characterised and is expected to have some variation given the number of parameters that determine the push beam interaction strength, as discussed in 3.6. The velocity measurement made using the interference pattern is much more accurate since it is only affected by the velocity range from the grating to the detector, where the acceleration is a=9.8 ms^{-2} for all atoms and is negligible.

Measuring an accurate value for the average atomic velocity below the grating is extremely important for the weak measurement of transverse momentum. The weak measurement allows the transverse momentum to be extracted from the total velocity, therefore the accuracy of the transverse momentum measurement will rely on the accuracy of the velocity measurement.

A new measurement for the Van der Waals coefficient

The diffraction pattern is strongly dependent on the strength of the Van der Waals interaction between the atoms and the slit walls. This attractive force increases the width of the envelope of the signal and simultaneously increases the intensity of the tails of the peak as shown in figure 4.9. With this, we can fit equation 4.7 to the data by eye to determine the Van der Waals coefficient, C_3, shown in figure 4.13. For $\bar{v} = 12.85\,\mathrm{ms}^{-1}$, $C_3 = 1.97 \pm 0.19\,\mathrm{au}$,

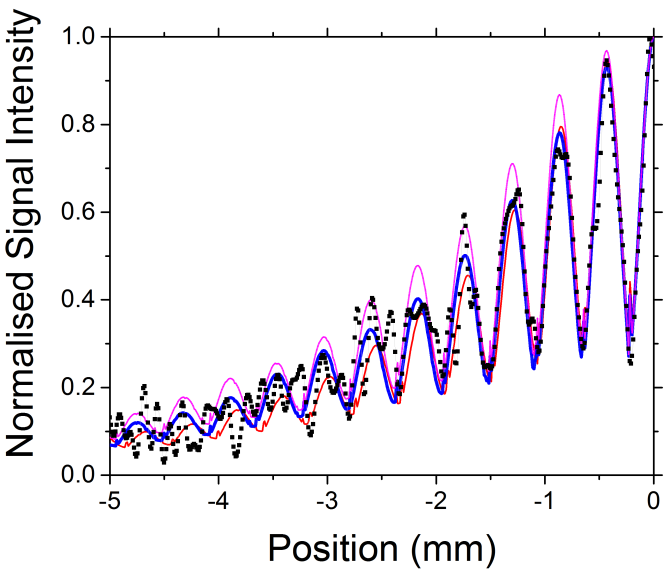

Figure 4.13: A comparison of the fit different values of C_3 corresponding to 1.78 au (red), 1.99 au (blue) and 2.15 au (magenta) for the 12 ms^{-1} atomic velocity matter-wave interference.

$\bar{v} = 15.15\,\mathrm{ms}^{-1}$, $C_3 = 2.02 \pm 0.16\,\mathrm{au}$ and $\bar{v} = 18.65\,\mathrm{ms}^{-1}$, $C_3 = 2.71 \pm 0.23\,\mathrm{au}$. Here the uncertainty is estimated from the difference between the upper and lower C_3 values that plausibly fit the data. The previous free parameter v was fixed at the measured value from the previous velocity measurements and all other fixed parameters were kept the same with the same uncertainties. This is not including C_3 which was then changed to a free parameter. This is the first measurement of C_3 for the interaction between metastable argon and Si_3N_4. Two of the measurements agree with previous simulations for the interaction [49]. The atoms travelling at $\bar{v} = 18.65\,\mathrm{ms}^{-1}$ produced a low contrast interference pattern due to the poor beam coherence. This is a possible explanation of why the measured value is much higher than the other two approximately equivalent values.

More accurate and varied characterisation of the atomic beam would be possible with improved data sets that show higher order interference peaks. The longitudinal velocity distribution can be extracted by more accurately by fitting equation 4.7, but rely on the higher order fringes for an accurate fit. Additionally, the simulations in figure 4.14 show that not only C_3 nut also Δv affect the diffraction profile and should be fitted parametrically. For a more accurate measurement of Δv and C_3, higher interference fringe orders could be resolved with better transverse and longitudinal coherence of the atomic beam.

4.5 Conclusions

This chapter shows the construction of multi-slit matter-wave interferometer. The interferometer demonstrates a spatial superposition of atoms in the atomic beam as a result of diffraction through a nanostructured Si_3N_4 grating. The resulting interference pattern was used to measure the velocity of the atoms at the position of the multi-slit grating. The velocities were consistently higher than the TOF velocities indicating the discrepancy between v_{TOF} and the true

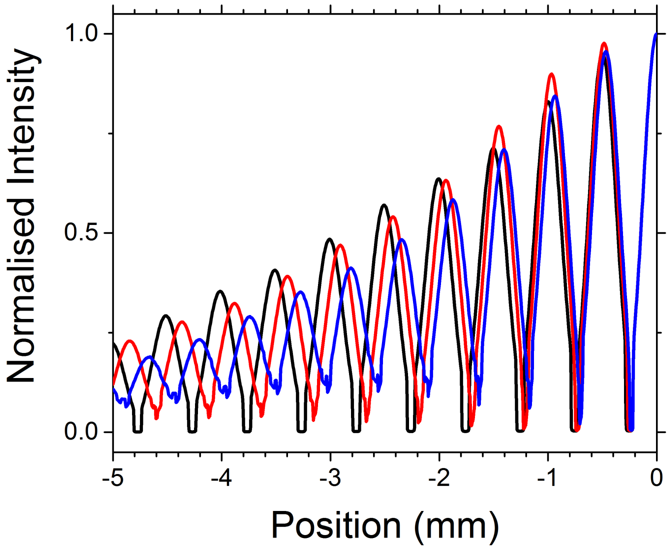

Figure 4.14: A simulation of the interference pattern for the 0-8th order fringes. The plot shows the fringes for Δv=0 ms^{-1} (black), Δv=0.5 ms^{-1} (red) and Δv=1 ms^{-1} (blue).

v. Additionally, the envelope of the interference pattern was used to measure a Van der Waals coefficient for the interaction between the atoms and the grating. To our best knowledge, this was the first time this has been measured.

Chapter 5

A longitudinal Stern-Gerlach interferometer for metastable argon atoms

5.1 Introduction

A fundamental characteristic of a weak measurement is the coupling of an observable to a pointer. Our observable is the transverse momentum of an atom in an matter-wave interferometer, which is described in detail in chapter 4. The pointer must be an internal state of the atom, which changes depending on the atom's transverse momentum during the weak measurement interaction. Importantly, the interaction must not significantly perturb the centre-of-mass motion of the atom. For the pointer we use the magnetic spin states of the metastable argon atom ($J = 2$, $m = 0 \pm 1 \pm 2$) since a uniform, magnetic field induces a spin-state dependent phase shift of the atom's wavefunction. We therefore need a device which can measure the phase shift induced in metastable argon spin states by a magnetic field. We also require the phase shift to be dependent on transverse momentum.

Such a device is known as a longitudinal Stern-Gerlach interferometer(LSGI)

[37] and a schematic outline of this process is displayed in figure 5.1

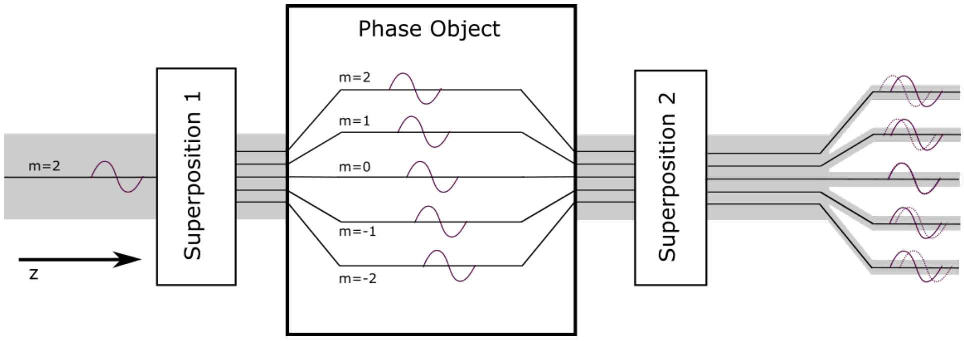

Figure 5.1: A schematic of the stages of an LSGI for an atom in a metastable state with five Zeeman sublevels, m. When the individual m states are individually observed, the interference appears as modulations in the intensity of the signal.

The operating principles of an LSGI for metastable argon can be broken down into the following sections. First, a linear superposition of m states is created by a spin-flip of a spin polarised atom. A spin-state dependent phase shift then occurs due to a magnetic field (phase object) followed by another spin-flip which builds a new coherent superposition. The last flip interferes the phase-shifted m states and when then the individual spin states are isolated from one another, the interference is observed.

We consider using spin polarised metastable argon atoms in the 4s$[3/2]_2$ state. Their magnetic spin state is described by the wavefunction $|\psi\rangle_0 = |J = 2, m = 2\rangle$ where the atom is quantised along the magnetic field B_z. It is then prepared in a superposition of spin states by a spin-flip which projects the initial state along the x axis. This process is represented using the Wigner rotation matrix $D^J(\phi, \theta, \chi)$ where $\theta = 90°$, giving a new wavefunction

$$\begin{aligned} |\psi\rangle_1 &= D(0, \tfrac{\pi}{2}, 0)|\psi\rangle_0 \\ &= \frac{1}{4}|-2\rangle + \frac{1}{2}|-1\rangle + \sqrt{\frac{3}{8}}|0\rangle - \frac{1}{2}|1\rangle + \frac{1}{4}|2\rangle. \end{aligned} \tag{5.1}$$

A magnetic field induces a spin-state dependent phase shift, ϕ, given by

$$|\psi\rangle_2 = e^{-2i\phi}\frac{1}{4}|-2\rangle + e^{-i\phi}\frac{1}{2}|-1\rangle + \sqrt{\frac{3}{8}}|0\rangle - e^{i\phi}\frac{1}{2}|1\rangle + e^{2i\phi}\frac{1}{4}|2\rangle. \tag{5.2}$$

The states are re-projected back along the z axis by another spin-flip, such that the wavefunction is then given by

$$|\psi\rangle_3 = D^2(0, -\tfrac{\pi}{2}, 0)|\psi\rangle_2. \tag{5.3}$$

This causes interference of the spin states and an encoding of the spin dependent phase into the probability density. The populations of the individual spin states are then observed by optically filtering or spatially separating the atoms in a magnetic field gradient. For the case of $m = 0$, the probability density is given as $|\langle 0|\psi\rangle_3|^2$, where the probability density is

$$\langle 0|\psi\rangle_3 = \frac{1}{4}\sqrt{\frac{3}{8}}e^{-2i\phi} - \frac{1}{4}\sqrt{\frac{3}{2}} + \frac{1}{4}\sqrt{\frac{3}{8}}e^{2i\phi}. \tag{5.4}$$

In this chapter we describe and test an LSGI which allows us to measure a time dependent phase shift in the spin states of metastable argon atoms. This in itself is not a weak measurement of the transverse momentum since the time dependence is not related to the transverse momentum. However, as discussed in the theory chapter, tilting this system with respect to the transverse axis will allow a weak measurement of transverse momentum.

5.2 Experimental method

The atomic beam enters a mu-metal, magnetic shield which encloses the LSGI. The LSGI is a copper plate connected to a current supply and a switch. At either end of the plate is a double loop 'guiding coil'. The coils and the atomic beam are concentric and parallel to the resultant magnetic field direction, B_z. The atoms fall through the centre of the first coil which sets the quantisation axis to z. The atomic beam must be initially prepared in a spin polarised state ($m = 2$), as outlined in chapter 3. From the source the atoms fall 0.2 m towards the MCP detector, where the position of the atom is observed. The constructed LSGI is shown in figure 5.2

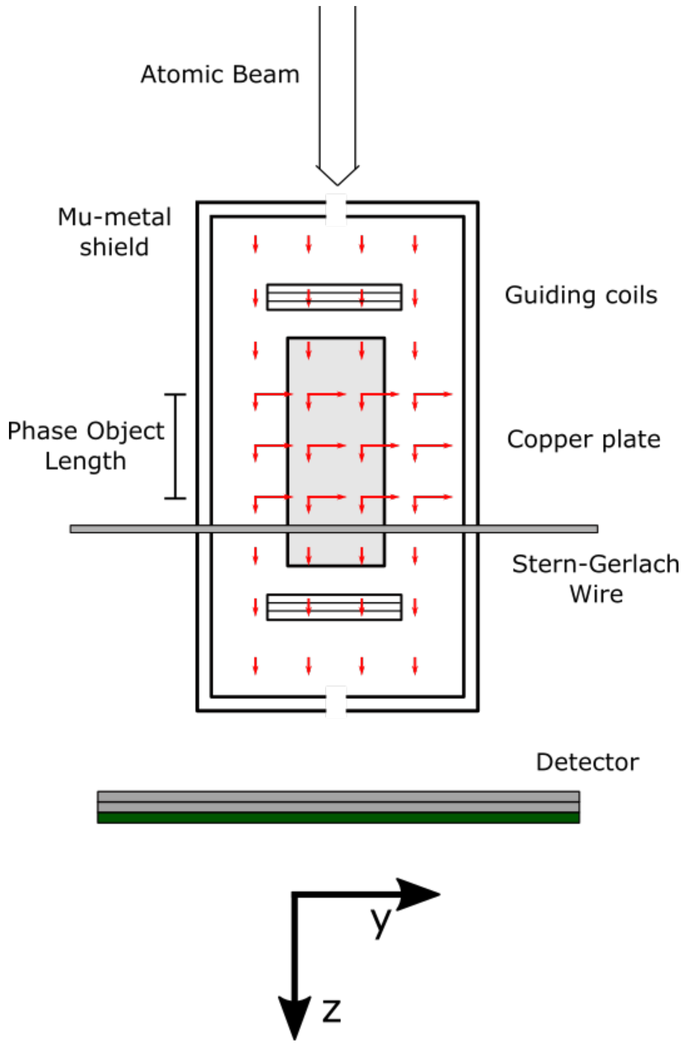

Figure 5.2: A schematic diagram of the LSGI. The magnetic field produced by the guiding coils and the phase object are shown in red. The current in the copper plate is pulsed on, rotating the overall magnetic field vector direction. The Stern-Gerlach (SG) wire spatially separates the spin states which are observed on the detector below. The field from the SG wire is not shown.

The interference process is initiated when the current in the copper plate is switched on, creating a new magnetic field direction perpendicular to the guiding coil's field. This quantisation axis rotation causes a non-adiabatic rotation and re-projects the atoms into a superposition of spin states.

Once the atom is in a superposition, the magnetic field induces two effects. During the transition into the magnetic field, the resulting gradient imparts a state dependent force on the atoms and spatially separates the spin states.

Additionally, over the length of the phase object, the uniform magnetic field induces a time dependent evolution which induces a spin-state dependent phase shift of the atom's wavefunction.

The current applied to the copper plate is rapidly switched off which again produces two effects. The quantisation axis is rotated to re-align with the field direction of the second guiding coil. In doing so the spin states are re-projected along the z axis, encoding the acquired phase shift into the new spin-state population probabilities. Secondly, the magnetic field gradient longitudinally deflects the atoms exiting the field and spatially recombines the paths of the spin states.

To observe the populations of the individual spin states, the atoms are spatially separated due to a magnetic field gradient created by a current carrying wire (SG wire). The wire is positioned within the mu-metal shield only to allow enough distance between the wire and the detector so that the spin states can be spatially resolved.

5.2.1 Spin-state superposition

The spin polarised atoms enter the LSGI where the $m = 2$ state is put into a linear superposition of the five possible m states through a re-projection of the initial state. This is induced by a rapid rotation of the external magnetic field, which causes an abrupt non-adiabatic rotation of the atom's quantisation axis.

Within the constricted spatial limits of this experiment, we rotate the external magnetic field by switching between two perpendicular magnetic fields. Since the LSGI is contained within a mu-metal shield, the overall field direction does not include any contributions from the geomagnetic field or any other magnetic field sources in the experiment. Therefore, we use two conductors with perpendicular current directions, the guiding coils and the copper plate (which also acts as the phase object). The currents are chosen so that the resulting magnetic field strength from the coils is much weaker than the field strength from the copper plate, as shown in figure 5.2. By applying the current to the copper plate, the external magnetic field direction switches from the direction set by the coils to the approximate field direction set by the copper plate. It is approximate since the direction is actually the combined coil and plate vectors. This then defines the quantisation axis rotation angle as the angle between these two field directions.

The equipment was designed such that the superposition process is repeated as the phase object ends, which in this case is when the current on the plate is switched off. This second re-projection process is achieved with an approximate 90° abrupt rotation of the spin axis. As before this is achieved by a rotation of the overall magnetic field direction. The direction is initially transverse, set by the plates and rotates to the longitudinal field direction, determined by the guiding coils.

There are two key aspects of this process that determine the nature of the resulting superposition. The quantisation axis rotation rate and the angle of rotation.

Rotation rate of the quantisation axis

To achieve a spin-state superposition via re-projection, the rotation rate/angular velocity, ω_B, of the atomic quantisation axis must be much faster than the Larmor precession caused by the external magnetic field, ω_L. The modelling suggested that a maximum magnetic field strength of the order of 10 μT should be used. Exceeding this causes phase shifts that are greater than 2π. At this field strength, the Larmor precession frequency is $\omega_L \approx 1.3 \times 10^6\,\mathrm{rad\,s^{-1}}$. For the spin-flip condition $\omega_L < 0.1\omega_B$, a 90° rotation we requires a rotation rate that is faster than $\approx 120\,\mathrm{ns}$. To achieve this we rapidly switch the current in the copper plate, the speed of which depends on the circuit inductance and the rise time of the transistor used. Here we use a power MOSFET (IRF320) which is specified to have a 90 ns rise time. This gives $\omega_B = 1.7 \times 10^7\ \mathrm{rad\,s^{-1}}$

which is more 10 times greater than the Larmor precession frequency at 10 μT.

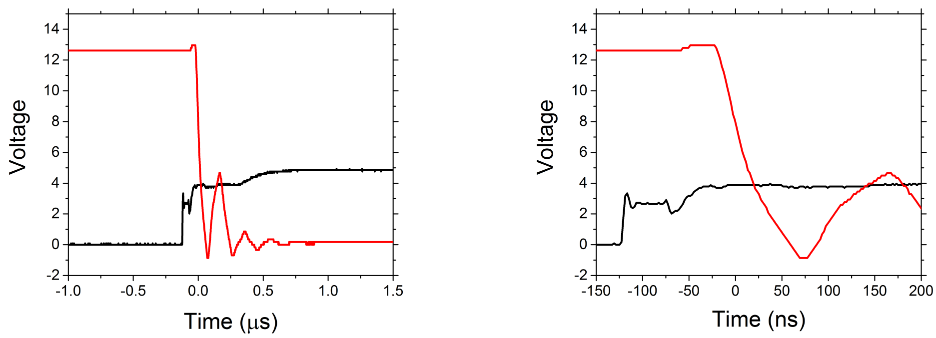

(a) (b)

Figure 5.3: Oscilloscope traces showing the voltage supplied to the MOSFET switch (black) and the voltage associated with the current through the copper plate (red). A small amount of ringing is shown in (a) which is plotted across 2.5 μs. The effective current switching time can be estimated as 75 ns from graph (b) which is plotted over 350 ns.

In reality the time it takes for the quantisation axis rotation isn't simply the switch rise time. A more accurate model would include the relative strengths of the initial external magnetic field and the phase object magnetic field. If the phase object field is much stronger than the background field the new field direction, given by the phase object field plus the background field, begins to dominate the magnetic field direction early on during the rise time and a 90° rotation would be achieved some time before the end of the 90 ns.

Rotation angle of the quantisation axis

We define the quantisation axis rotation angle as the angle between the atom's initial and final quantization axes before and after the phase object is turned on. The rotation angle, θ, determines the fractional population probabilities of each m state of the superposition which are given by the Wigner rotation matrix $D^J(\phi, \theta, \chi)$. Ultimately, when the final signal is observed, θ affects the contrast of the m state population interference fringes. The maximum contrast is achieved with a $\theta = \frac{\pi}{2}$ rotation.

The mu-metal shield does not entirely block out all the magnetic fields. A small magnetic field, of the order of 10 nT originating from the experiment, will always leak into the shield defining an unwanted direction of quantisation. In order to have a well-defined quantisation axis inside the shield, a magnetic field is created by a pair of identical coils, named ‘guiding coils’ and are centred on the beam axis. The double loop coils have a 13 mm radius, set 70 mm apart from each other and the pair can be positioned at any height within the shield.

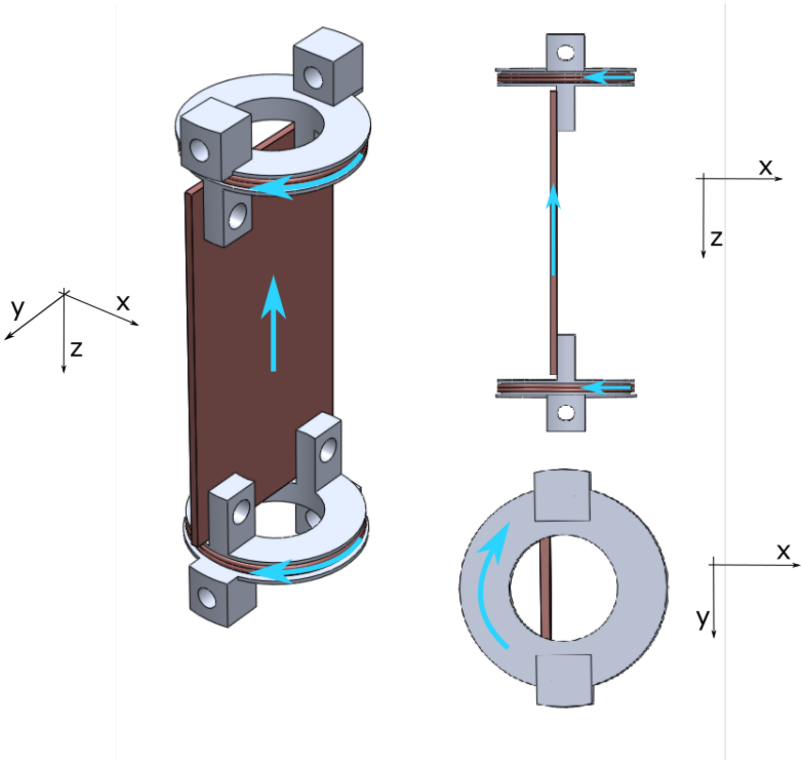

Figure 5.4: A CAD drawing of the formers used to build the guiding coils and how they attach to the copper plate. The current directions are shown in blue.

The mu-metal cylinder attenuates the background magnetic fields to at least 10 nT. With a current of 1 A through the coils, a field of 10 μT is created at the midpoint of the coils and the resulting magnetic field direction is parallel or anti parallel (depending on current direction) with the direction of the falling atoms along the z axis.

The phase object is a 1 mm thick copper plate measuring 50 x 25 mm, with the long edge set parallel to the atomic beam. The plate provides a relatively uniform magnetic field strength required for a weak measurement of transverse momentum. The plate is connected to a current source using a wire fixed at

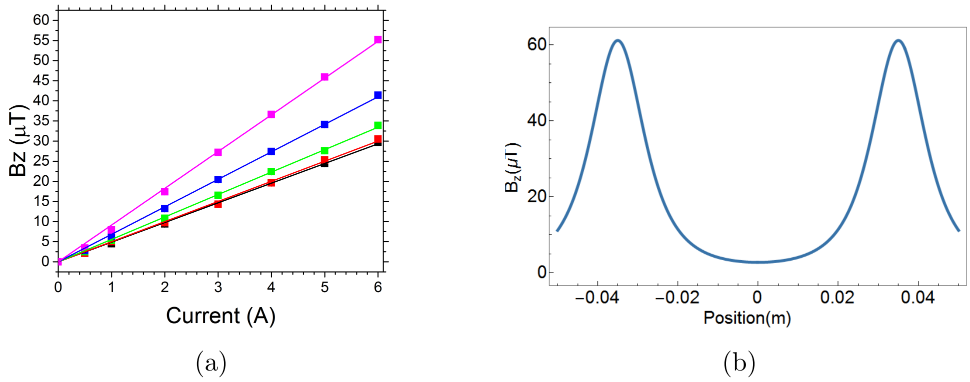

Figure 5.5: The magnetic field created by the guiding coils. (a) Shows the field measured using a Gaussmeter, at 0 mm (black), 3 mm (red), 6 mm (green), 9 mm (blue) and 12 mm (magenta) from the midpoint of the coils along z for a range of wire currents. The errors for each data point are too small too resolve in the graph. (b) The simulated field strength from 1 A in the the guiding coils along a z axis passing through the centre of the coils.

both top corners and a wire fixed at both bottom corners. The current travels either parallel or anti-parallel to the atomic beam depending on the current direction. The resultant magnetic field direction is then always 90° to the background field set by the guiding coils provided the plate's field strength is much greater than the coil's field strength. This provides the necessary rotation angle for an optimised superposition of the five m states.

The guiding coil field strength varies with z position, see figure 5.5(b). Therefore, for the packet of atoms that are detected, the total field strength B will be different depending on the atom's position when the phase object is turned on and off. Subsequently, the timing of the current pulse determines the rotation angle (and more importantly, the success of the spin-flip via the spin-flip condition, $\omega_L \ll \omega_B$). This creates a field-strength-dependent limit of when the current in the copper plate can be switched on/off.

5.2.2 The phase object

The phase object of the LSGI is a weak magnetic field created by passing a current through a copper plate. Section 2.2.2 derived the equation for phase shift, ϕ, due to the interaction between the atom and the magnetic field and is given by

$$\Phi = m\frac{g_f \mu_B}{\hbar} B(z) t_{ws}. \tag{5.5}$$

This is dependent on the m state of the atom and two properties of the phase object; the magnetic field strength and the interaction time. With the atom in a superposition of states, the phase shift differs between each m state. Comparing this with the refraction of light through a bi-refringent medium, we are presented with a multi-refringent atomic-optical system of five polarisation states rather than two in the optical case.

To help extract meaningful data from the observed phase shift, we need to change the magnetic field strength, while keeping the interaction time constant, or vice-versa. When the LSGI is implemented in a weak measurement scheme, the magnetic field strength must be kept constant and the interaction time is measured. However, for a simple initial step the LSGI is tested independently by keeping the interaction time constant and measuring the average magnetic field strength from the phase shift. Here the interaction time is well-defined and controlled, therefore the LSGI can be well calibrated and optimised before using it to observe the small changes in the atom's transverse momentum for the weak measurement.

Interaction strength between the atoms and the magnetic field

The phase object magnetic field is pulsed on and off during each atomic beam pulse, therefore the LSGI interaction time is controlled by setting the TTL pulse width, which switches the MOSFET controlling the current in the copper plate. The total interaction strength is dependent on t_{ws} and B so any increase in one can be compensated by a decrease in the other.

To select an appropriate interaction time of the phase object, the overall magnetic field strength and shape must be considered. The field of the guiding coils, given in figure 5.5(b), and the copper plate, figure 5.6, make the field strength of the phase object dependent on where the atoms are when the current pulse is switched.

If the field is too strong, the temporal separation of the m states' interference fringes can become too small to resolve on the detector for the achievable gate times, this relationship is modelled and shown in figure 2.7. Additionally, a strong field gives rise to an unwanted B field gradient in the y direction whereby the signal, separated by m states in x direction, again loses resolution of the interference fringes for a given phase object length. This is investigated in section 5.3.3 as the 'Magnetic gradient parallel to the plate'.

The field strength also affects the spin-flip process. For the spin to be re-projected at all, the field strength must be low enough to meet the spin-flip condition. Additionally, the spin-flip rotation angle will determine the contrast of the LSGI's interference fringes. Therefore, it is often useful to visualise the phase object duration as the length of the region that the atoms traverse, while exposed to the phase object. This also becomes increasingly relevant for the weak measurement design using the LSGI concept.

To test the LSGI we incrementally adjust the phase object duration between 1 and 100 µs. For atoms travelling at 50ms^{-1} this corresponds to a length of 0.05 - 5 mm. This change from the atomic velocity used in the matter-wave interferometer (12 - 17 ms^{-1}) is due to the increased signal intensity achieved with faster atoms. For each data point, the phase object length is kept constant, therefore any change in the observed phase shift at that point is due to changes in the magnetic field strength.

Characterising the magnetic field of the phase object

The current used to induce the phase object magnetic field, is controlled by a power supply (TTi, EX1810R) with a range of 0 - 10 A. Given that the MOSFET and copper plate are the only components of the circuit, no more than 1 V is required. Since the magnetic field strength is spatially varying, it must first be characterised. We can then select a current value to create a suitable magnetic field strength in the vicinity of the atomic beam. The suitable range of values are ones which do not cause the interference to over-modulate the atomic signal (estimated in section 2.2).

The magnetic field strength, parallel to the plates, for positions along the y axis, is given in figure 5.6(a). The current was increased from the typical operating currents of 1-2 A up to 6 A, in order to resolve the small changes in field strength given the Gaussmeter's resolution of 0.3 µT. The shape of the gradient does not significantly vary as the current is reduced, so the field magnitude is measured for a variety of currents at the same fixed position. The probe of the Gauss meter has a sensor area, and hence a spatial resolution, of 0.3 mm. The magnetic field gradient was measured by moving the Gaussmeter away from the plate along the x axis, as shown in 5.6(b). The measurements are repeated for different currents.

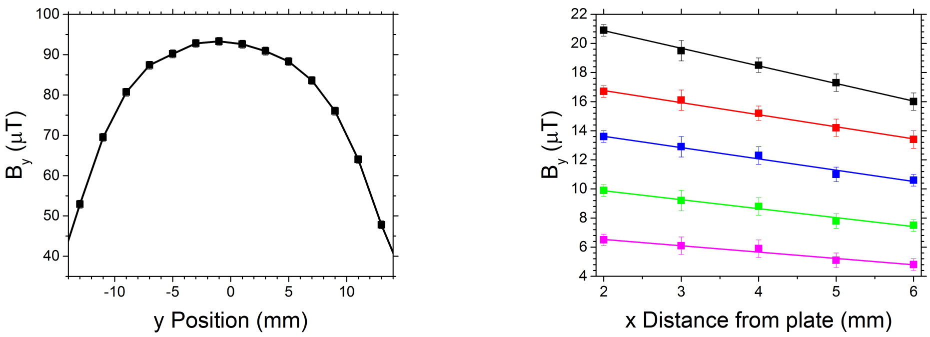

(a) (b)

Figure 5.6: The magnetic field strength created by a current passing through a single copper plate of 50x25x1 mm, as shown in figure 5.4. In (a) the probe was scanned across the 25 mm width of the plate (along the y axis in figure 5.4), for a 2 mm distance in x, between the probe and the plate, which is the distance between the atomic beam and the plate, for 6 A. In (b) the probe was kept at $y = 0$ and incrementally moved further away from the plate, along the x axis. This was repeated for 5 current settings; 1.2 A (black), 1.0 A (red), 0.8 A (blue), 0.6 A (green) and 0.4 A (magenta).

Combining the two data sets shown in 5.6(a) and 5.6(b), it was possible to extrapolate or interpolate to estimate the field strength, in a the region near the plate for any current setting. Figure 5.7 shows how, for any current, you can estimate the slope and intercept of the fit in figure 5.6(b) in order to estimate field strength at some position.

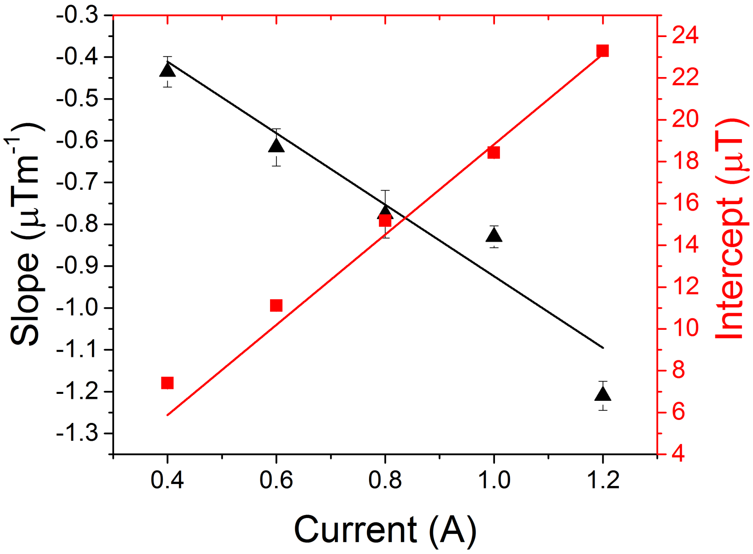

Figure 5.7: The values of the gradient (black triangles) and the intercept (red squares) for each measured magnetic field strength curve in figure5.6(b). Mapping out the values this way allows the magnetic field strength from any current, at any position in the local area, to be well estimated.

Each measurement was taken with the plates set up outside the vacuum chamber. The background magnetic field strength was measured and subtracted to give each data point a value solely due to the current on the plate. In practice, with the plates positioned inside the experiment we need to find a way to eliminate, or at least attenuate, the natural background field so that we can be sure the field strength matches the reference measurements from outside the experiment.

5.2.3 Mu-metal shielding

Earth's geomagnetic field measured by the National Oceanic and Atmospheric Administration, is on average 20 µT, 8 µT and 44 µT [59] for the experiment's x, y and z axes respectively, at the lab's latitude and longitude. Discounting any other field sources in the lab, the Earth's field alone is enough to increase the atoms' Larmor frequency such that the spin-flip condition is difficult to meet. Additionally, the field will dominate over the phase object's field, distorting the rotation angles. These key obstacles lead us to design and build a mu-metal shield to attenuate the natural background field strength.

The shield had to be cylindrical with a diameter no wider than 37 mm in order to fit through the viewport of the chamber. Additionally, cylinders are the optimum shape for mu-metal shields. The thickness of the shield was limited to approximately 5 mm, any greater and it would start to restrict the available volume to contain the phase object. Cylindrical mu-metal shields have a stronger attenuation effect using multiple thin layers rather than one thick layer [60], therefore two concentric cylinders of 2 x 1.5 mm thick walls with a 2 mm gap were designed. The cylinders are closed ended to attenuate the field in the z axis. The end caps were welded on to the bottom of the cylinders and left loose on the top to allow the phase object to be inserted into the shield. Slots were made on each end cap to allow the atomic beam to pass through.

When positioned in the vacuum chamber, the cylinder blocks the path between the detector chamber and the turbo molecular pump for atoms to escape when the chamber is pumped down. To address this, the cylinders were designed with holes in the end caps and the inner cylinder. The holes, if too large or many, reduce the effectiveness of the cylinder's attenuation. Simulations were again used to demonstrate this effect and find the largest possible hole size without reducing the attenuation of the shield.

The simulation of the field attenuation achieved with the final design is shown in figure 5.9. With a natural background field strength of $\sqrt{3}\,\mathrm{mT}$, whose direction is 45° from the x, y and z axis, the internal field reduces to $\approx 10\,\mathrm{nT}$. The simulation did not include fields entering from different directions, which may permeate by different amounts through the holes. However, the degree of attenuation shown by the model for the given field strength was strong enough to suggest that typical fields from any other direction, which would likely be

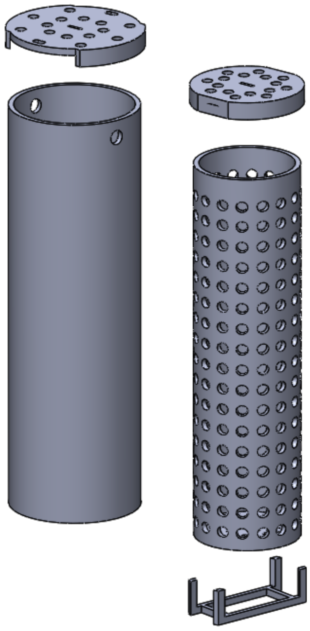

Figure 5.8: The exploded diagram of the mu-metal shield. The inner and outer cylinder here are shown side by side with exploded parts. The design also includes a spacer that sits at the bottom between the 2 cylinders.

much weaker, would not significantly contribute to the field within the shield.

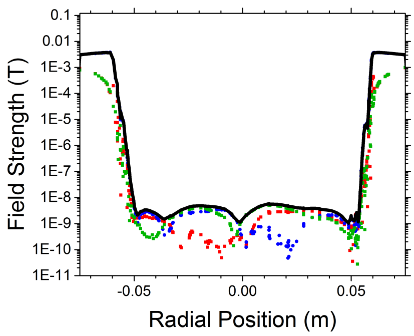

(a)

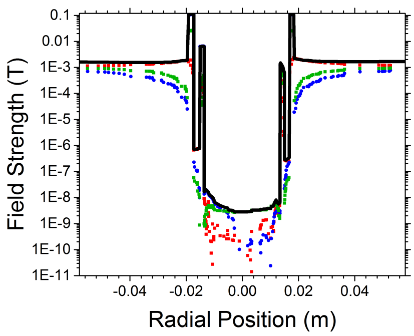

(b)

Figure 5.9: The magnetic field strength along (a) the cylinder's axis and (b) across the diameter of the mu-metal shield, modelled in COMSOL, with a 1mT external field in the x, y and z directions. The plots show the field strength of B_x (red), B_y (blue), B_z (green) and the total field, B (black).

5.2.4 Observing individual states

Key to observing the phase change in the m states is the ability to observe the signal from individual m states. Since the detector does not discriminate between these states, it is necessary to either spatially separate the m states using a magnetic field gradient or to isolate the $m = 0$ state using a 'quench' laser beam. Both were used while testing the experiment.

Spatial separation

The ideal solution for observing the m states is to spatially separate them using a magnetic field gradient, as in a traditional Stern-Gerlach experiment. This method measures the population of all the m states simultaneously and allows a direct comparison of the phase shift between the m states. The easiest design for this gradient was to run a wire along side the copper plate, which was parallel to the slit orientation and very close to the atomic push beam, as shown in figure 5.10. The wire was connected to a 60 V battery and a MOSFET switch (Crydom D5450) that essentially short circuited the battery when the switch was open. By keeping the switch open for only a few milliseconds, the battery would momentarily carry a very high current of around 240 A, but not have enough time to overheat and melt the circuitry. The resulting field created was enough to resolve the 5 states on the detector despite the relativity short distance between the detector and the wire of about 100 mm.

We only observe a fraction of the atoms of each push beam pulse due to the exposure time set on the detector. The current switch is activated when the atoms, which are later observed on the detector, are at a position level with the wire. Modelling the wire's magnetic field switch on time and subsequent deflection of the atomic beam is shown in figure 5.11 and 5.12. This shows that only a very momentary current pulse is needed for an efficient m state separation.

Spatially separating the states using a wire requires a narrow transverse

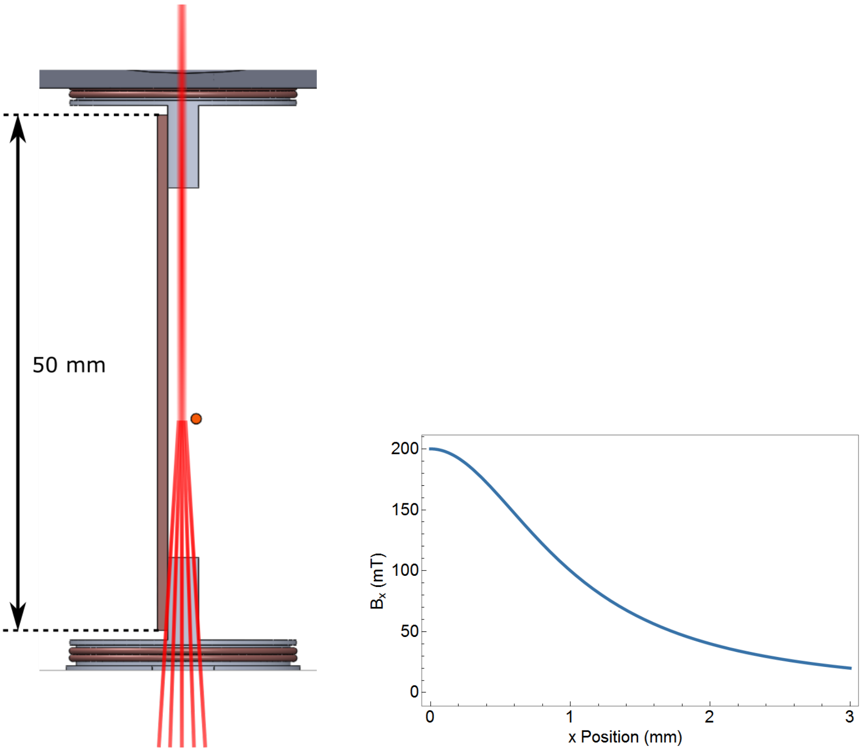

(a) (b)

Figure 5.10: (a) A CAD drawing showing the location of the Stern-Gerlach wire in relation to the phase object (copper plate) and guiding coils. The approximate position of the atomic beam is shown with the m states being deflected by the wire's magnetic field gradient which is shown in (b). The x axis indicates the radial position from the wire. The gradient of this field is proportional to the transverse force that separates the m states.

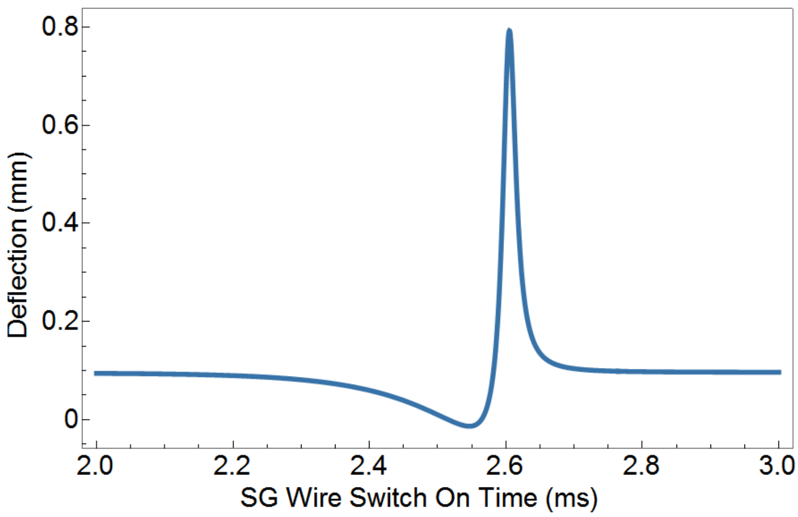

Figure 5.11: The atomic deflection of a $m = 2$ atom after a TOF of 4 ms (v=50 ms^{-1}). The switch-on time of a 0.5 ms current pulse through the SG wire is varied.

velocity distribution of the atomic beam. If the distribution increases, it requires a greater magnetic field gradient to be able to resolve the signal peaks from each m state. The transverse velocity can be selected using the collimation slits. The transverse velocity spread needed to resolve the m states will depend on the z position of the wire, the current on the wire and the atom's velocity. For atoms travelling at $50\,\mathrm{ms}^{-1}$ and when the wire is 100 mm from the detector, the transverse velocity selection should be better than $\approx \pm 0.12\,\mathrm{ms}^{-1}$.

The spread in the atom's final transverse position is not only dependent on the slit's transverse velocity selection. There is also a spread observed due to the m state dependent interaction with the wire's field gradient. Atom's with $m < 0$ will be deflected towards the wire and $m > 0$ are deflected away, so $m < 0$ state atoms will experience a larger gradient and hence a larger deflecting force due to the shape of the gradient from the wire, as shown in figure 5.12. This results in a defocussing effect, which is stronger for the lower m states.

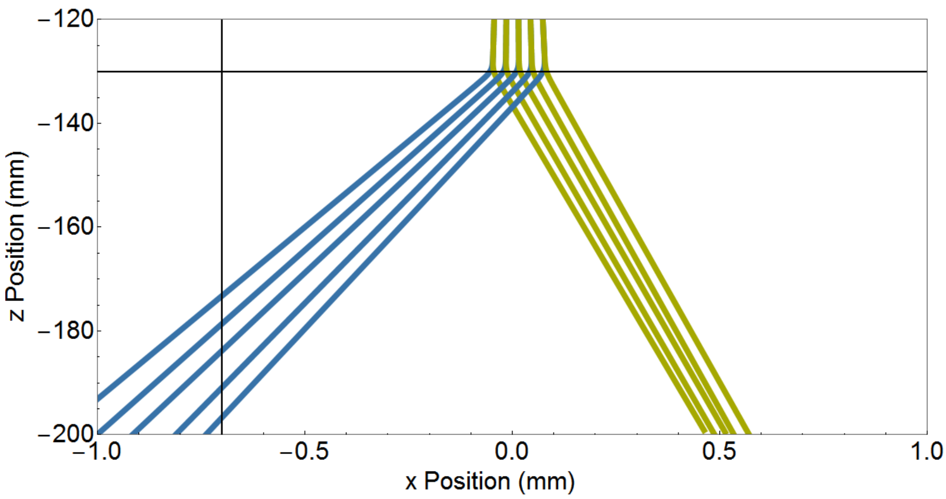

Figure 5.12: A simulation of trajectories for five transverse initial velocities, between -0.1 and $0.1\,\mathrm{ms}^{-1}$. These are plotted as they pass through the magnetic field from a current carrying wire centred on the black cross-hairs. Each velocity selection contains the paths for the $m = -2$ (blue) and $m = 2$ (green) spin states. The focussing of $+m$ states and the defocussing of the -m states can also be seen.

Filtering

In some cases, spatially separating the atoms introduced further problems. Firstly, there is uncertainty whether or not another spin-flip occurs when the

SG wire turns on. Secondly, for very fast atoms or a poorly collimated beam, the large SG wire current that is needed to achieve acceptable resolution between the states is too high for safe use of the equipment. Lastly and most importantly, when considering the final weak measurement setup, the matter-wave interference fringes will be distributed in the transverse direction (x axis). The spin-state separation would then need to be distributed in the perpendicular direction (y axis). This would again need collimating in the y axis and hence would require pinholes to sufficiently collimate the beam in both the x and y axes, thus massively reducing the signal. As a result, alternative methods were considered to observe individual states. One of which involves using an 801 nm laser to 'quench' 4 of the 5 m states, such that only the $m = 0$ state is present.

As described in section 3.3.1, laser cooling of metastable argon uses the closed cycle transition $4s[3/2]_2 \rightarrow 4p[5/2]_3$, where the excited state always decays back to the same J state. However, there is also a $4s[3/2]_2 \rightarrow 4p[5/2]_2$ transition that decays to the ground state (via the $4s[1/2]_1$ and $4s[3/2]_1$ state).

The quenching process can be stimulated in any of the five m states. However, selection rules allow particular states to be unaffected by the quench beam. If the quench laser is polarised parallel to the quantisation axis of the atom, the $m = 0$ state cannot absorb the photons. This will filter out the $m = \pm 1, 2$ states by sending them to the ground state. A similar process can be used to isolate the $m = \pm 2$ states using circularly polarised light, indicated in figure 5.14.

It is necessary to use a magnetic field to define the quantization axis, but care must be taken to use the correct field strength. If the field is too strong, it will shift the energy of the transition via the Zeeman effect. This will shift the transition frequency away from the frequency range of the quench laser. Similarly as the atoms are travelling at a speed of approximately $50\,\mathrm{ms}^{-1}$ in z, the quench beam must be perpendicular (in the yz plane) to the atomic beam

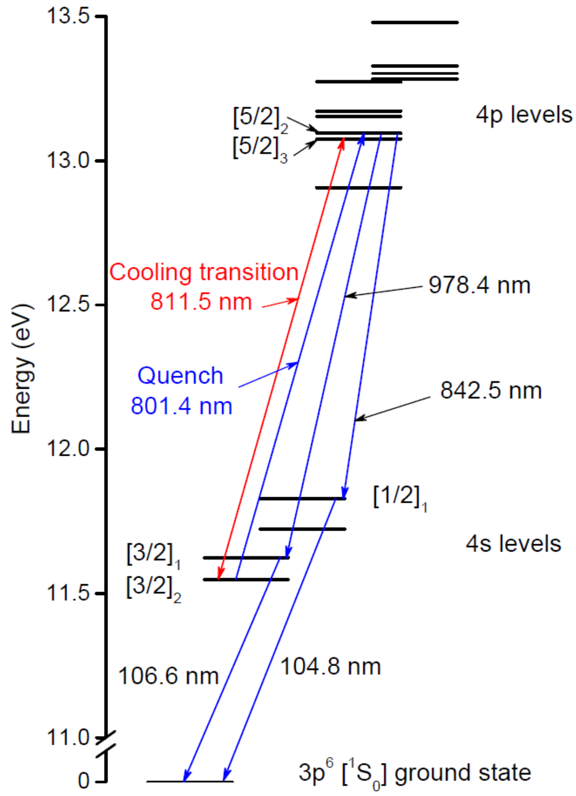

Figure 5.13: Grotrian energy level diagram for this experiment's relevant Argon transitions.

to avoid a change in the relative frequency due to the Doppler effect.

The quench beam source was produced by a 9 mm laser diode which was designed to operate at 808 nm. However, since not all these diodes operate at exactly 808 nm, it was hand picked by the manufacturer to be as close as possible to 801 nm. The diode was operated using a current and temperature controller (Thorlabs LDC220C and TED200C respectively) and laser frequency was monitored using a wavemeter (High Finesse WS-u 30).

The lab's ambient temperature was controlled by an air conditioning system, using a built in PID-servo control. This control causes the lab temperature to oscillate at a level that affects the laser's temperature, which could not be corrected by the laser's temperature controller. Diode lasers change frequency at about 0.3 nm per degree Celsius and the laser temperature controller could only maintain a constant temperature to within $\pm 0.1°C$. As a result, the laser frequency slowly oscillates throughout the day. With the quench beam

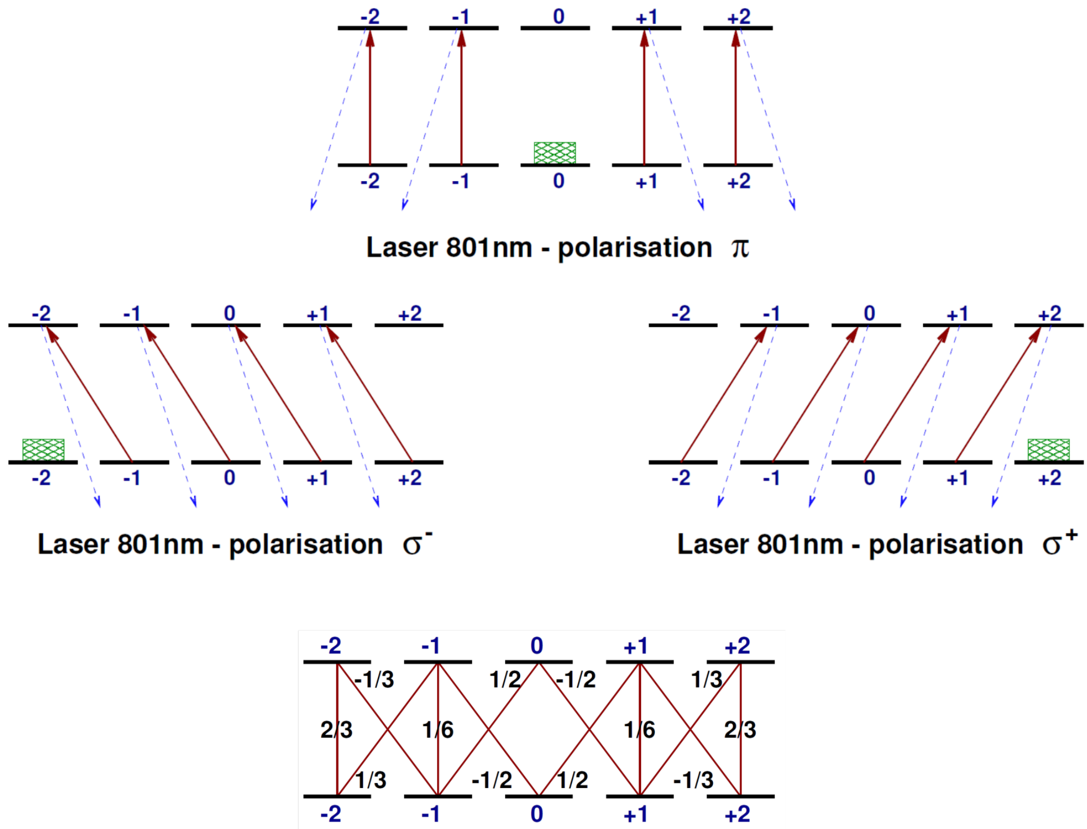

Figure 5.14: The excitation and decay schemes for various laser beam polarisations for the 4s$[3/2]_2 \rightarrow$4p$[5/2]_2$ transition. At the bottom is the Clebsch-Gordon coefficients for transitions between the states.

pointed directly at the MOT, we can get an idea of the range over which the quench beam will interact with the atoms. This was about 200 MHz and is indicated by the dotted line in figure 5.15(a)

To combat this, another PID-servo controller was introduced. The controller was built in LabView and uses the output of the wavemeter as a feedback signal to send a voltage to the laser current controller via an Arduino Uno. The plot of the Arduino controlled 801nm laser frequency can be seen in figure 5.15(b). It stays well within the 200 MHz necessary for efficient quenching. There are random spikes in the plot where the required voltage signal for the laser current falls out of the immediate range of the Arduino output. The Arduino output range is automatically adjusted and the output voltage returns to the chosen setpoint.

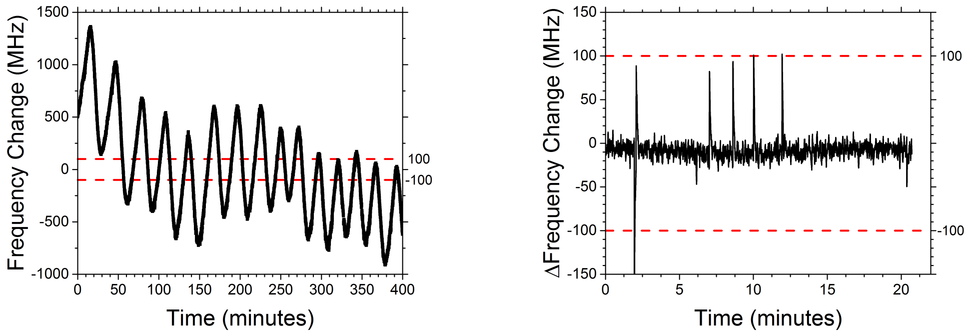

(a) (b)

Figure 5.15: The 801 nm laser frequency measured through the wavemeter over time. (a) Over the course of the day, with no laser frequency stabilisation, the oscillations occur due to small temperature changes in the laboratory, driven by the lab's air conditioning unit. (b) The same setup, but now with the Arduino PID-servo control adjusting the laser current to compensate for the temperature oscillations.

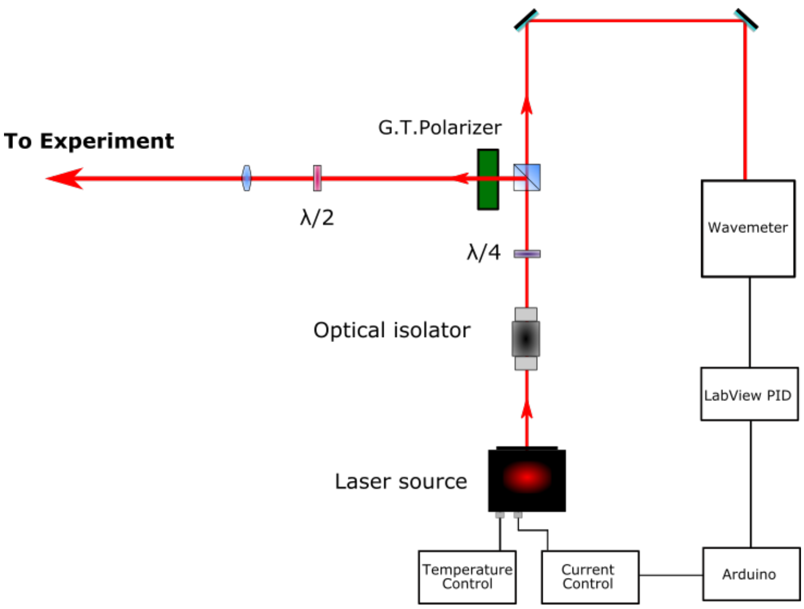

Figure 5.16: A schematic diagram of the quench laser system.

The quench beam is passed through the atomic beam just before the the atomic beam reaches the detector. Optical access via two parallel viewports on a purpose made rotatable adapter, allow the beam to be retro reflected and double the power density at the point of interaction, figure 5.17. The rotatable adapter allows the quench beam to perpendicularly cross the atomic beam. This is important since a small deviation from the perpendicular axis can reduce the efficiency of this type of filtering. If there is a reduction in the orthogonality of the quench beam and the atomic beam (i.e. the beam makes an angle from the xy plane), the atoms will see slightly Doppler shifted photons as a result of the atom's velocity in z. The shift brings the relative laser frequency away from the transition frequency and hence reduces the interaction with the atoms.

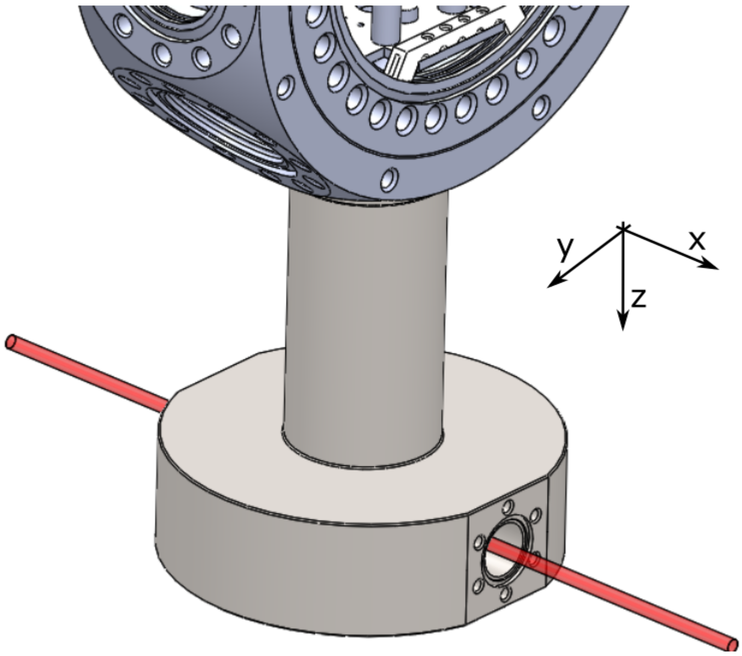

Figure 5.17: A CAD drawing showing how the quench laser is introduced into the experiment, perpendicular to the atomic beam.

The quench beam is linearly polarised, the angle of which should be parallel to the atoms' quantisation axis in the region of interaction with the atomic beam. The angle is optimised by rotating a half-wave plate to match the quantization axis in the interaction region. This optimisation only works if the magnetic field direction has no strong x component. The field direction is estimated by measuring the x, y and z component using a Gaussmeter. For settings used in this chapter, the field was measured as $B_x = 1 \pm 0.4\,\mu\mathrm{T}$, $B_y = 1 \pm 0.4\,\mu\mathrm{T}$ and $B_z = 14 \pm 0.4\,\mu\mathrm{T}$.

The data in figure 5.18 shows the optimisation of the quench beam polarisation. It is clear that even with the optimum polarisation angle, there is still some atoms in the $m = \pm 1$ states that are not being filtered out. This inability

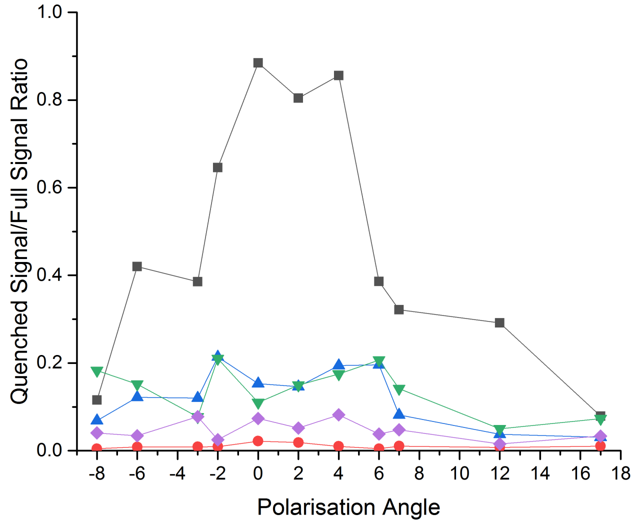

Figure 5.18: Data showing the average atomic signal intensity for each m state as the angle of the half-wave plate controlling the quench beam polarisation is rotated, $m = -2$ (black), $m = -1$ (red), $m = 0$ (blue), $m = 1$ (magenta) and $m = 2$ (green). At 0° the half-wave plate is transmitting light which is polarised in the z axis.

to completely quench the $m = \pm 1$ states is unlikely to be due to an incorrect quench beam frequency, since the stretched states, $m = \pm 2$, which are even further away from the central transition frequency than the $m = \pm 1$ states, are still quenched efficiently. It is more likely to be caused by poor optimisation of the polarisation angle, which allows some $m = 0$, excited states to be populated and then spontaneously emit from the $m = 0$ state back down the $m = \pm 1$ states.

5.3 Results

5.3.1 Spin polarisation of the atomic beam

The atomic beam, constructed in chapter 3, demonstrated a $m = 2$ spin polarised source of metastable argon atoms. During the construction of the LSGI, the mu-metal shield was introduced with the SG wire now positioned roughly 100 mm from the detector (figure 5.10). The atomic beam spin polarisation was tested again. The results showed that the beam does not maintain its spin polarisation when the atomic beam passes through the shield. It was initially thought that switching the current in the SG wire was causing a spin-flip and hence a re-projection of the spin states. It was also considered that the low field strength in the field and the deforming effect that the mu-metal has on the magnetic field could cause regions of rapidly changing field direction in the narrow entry slot of the cylinder. Either or both of these hypothesis could be correct. The problem was overcome with the introduction of the guiding coils.

The guiding coils set the background field strength and direction. The coils provide a constant quantisation axis that would dominate any small, stray fields. Additionally, the direction of the guiding coil magnetic field is the same direction as the SG wire magnetic field (in the moment that the SG wire field is turned on). The guiding coils address both concerns of the loss of spin polarisation that were introduced by the mu-metal shield. The atomic beam polarisation was tested using the SG Wire for various guiding coil currents, figure 5.19(a).

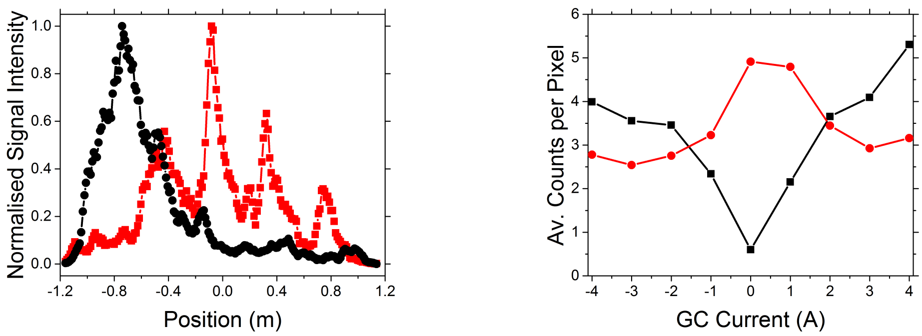

(a) (b)

Figure 5.19: (a) The atomic beam signal which has passed by a SG wire to spatially separate the m states. The atoms were initially polarised in the $m = 2$ state and travel through the mu-metal shield. With 0 A (red) passing through the guiding coils, a spin-flip is observed, but with 4 A (black) the guiding coils maintain the background magnetic field direction, hence maintain the spin polarisation. (b) Using a quench beam to isolate the states, the changing populations of the $m = -2$ (black) and $m = 0$ (red) states as the current on the guiding coils is varied. When there is no current, the loss of a well-defined quantisation axis allows a spin-flip that causes the initial $m = 2$ polarisation to be lost.

The result shows the spin polarisation of the atomic beam is not perfectly pure, so even when the stretched states are maximally populated, there are always some atoms in the remaining m states. In order to investigate any effect of a possible spin-flip from the switching-on of the SG wire, the atomic beam was quenched to measure the population in $m = 0$. Comparing the results from the two methods also highlights the value of the extra information gained by spatially separating the atoms.

5.3.2 Spin-state re-projection

Superposition

Initially we test the spin-flip re-projection by looking at the populations of each m state after a single rotation of the the quantization axis. Comparing the results to equation 2.16 we can determine the success of the spin flip and the angle of rotation.

To initiate the spin-flip, the current on the copper plate is switched on when the atoms pass by the copper plate. The push beam and detector is configured to only observe atoms with a TOF velocity of $51.5 \pm 0.1\,\mathrm{ms}^{-1}$ which equates to approximately 1 mm of the falling atom packet. This means the rotation angle calculated from this data is correct for a longitudinal region of 1 mm. At this velocity the majority of the atoms pass by the copper plate between 1.8 and 2.7 ms after the atoms were pushed from the trap. Comparing the results with the model, we can determine the angle between the quantization axes set by the guiding coils and the quantisation axis set by total field (guiding coils plus the phase object).

The current through the copper plates remained switched on until the atoms reached the detector. This meant that there was no abrupt switch off of the magnetic field and hence no second superposition due to a spin-flip. As a result the populations observed at the detector were due to a single spin-flip re-projection only. The signal intensity peaks for each m state are shown in figure 5.20. Here the guiding coil current was set at 1 A and the phase

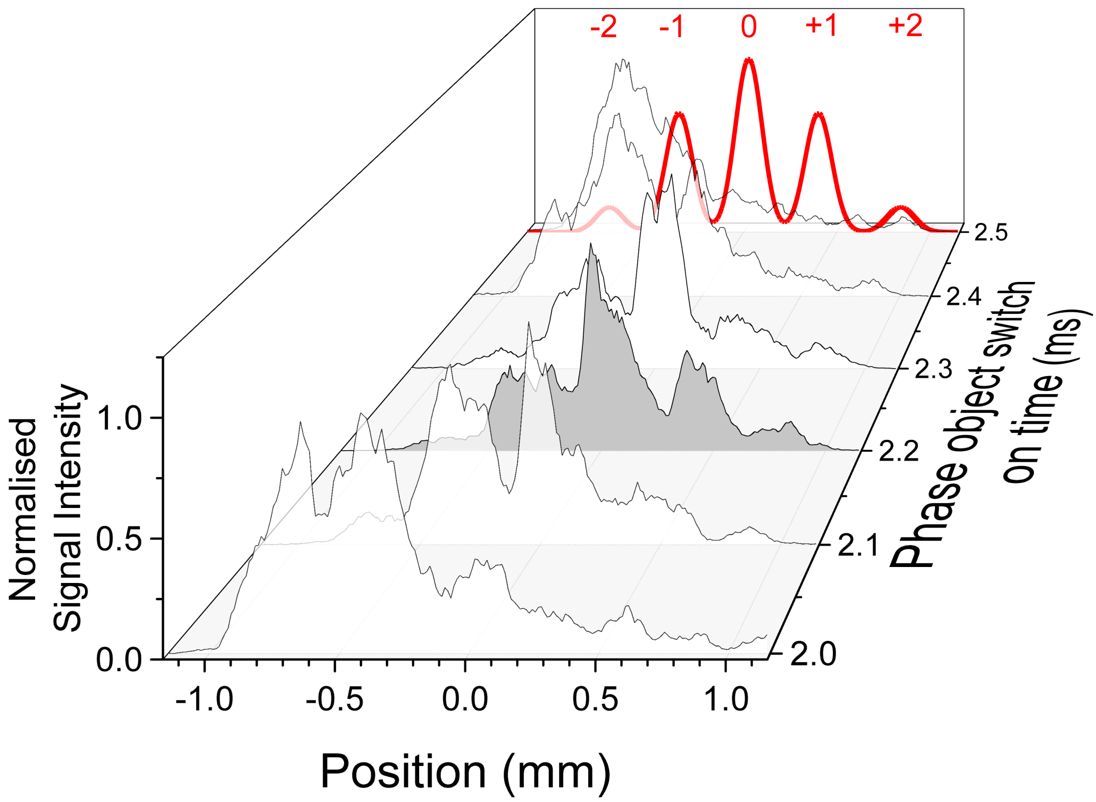

Figure 5.20: The atoms' m state populations after experiencing a spin-flip due to switching on the current in the copper plate. The z axis shows the time between the start of the push beam pulse and when the current is switched on. Peaks with areas equivalent to the expected m state populations, for a $\frac{\pi}{2}$ spin-flip rotation angle, are shown in red.

object (copper plates) current was set at at 15 A. This meant the phase object magnetic field easily dominates the guiding coil field and the rotation angle was very close to 90°.

The second spin-flip

A similar procedure was carried out to test the rotation of the quantization axis when the phase object field was switched off, as shown in figure 5.21. The rotation angle in this case is between the field direction of the total magnetic field (the phase object plus the guiding coil) and the guiding coil field alone. The phase object was switched on before the atoms were pushed from the trap. This way the atoms adiabatically align with the quantisation axis set by the phase object as they fall through the apparatus. No re-projection happens yet since the atom's quantisation axis rotation happens much slower than the frequency of the Larmor precession. When the phase object field is switched off, the rotation rate is much quicker than the Larmor precession frequency. The spin-flip condition is therefore met and the populations of the m states are determined by the angle of rotation.

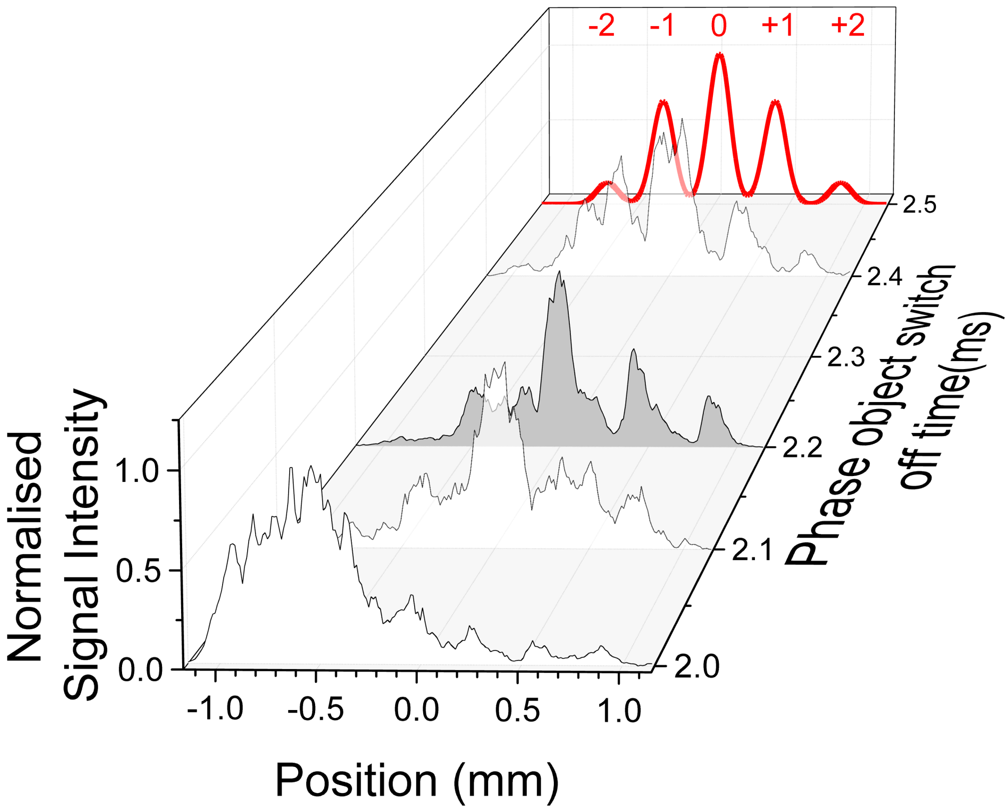

Figure 5.21: The atoms' m state populations after experiencing a spin-flip due to switching off the current in the copper plate. The z axis shows the time between the start of the push beam pulse and when the current is switched off. Peaks with areas equivalent to the expected m state populations, for a $\frac{\pi}{2}$ spin-flip rotation angle, are shown in red.

These projections were achieved with 2 A current (12.56 V/6.3 Ω) on the single copper plate and 1 A on the guiding coils. The data for figures 5.20 and 5.21 were obtained using constant push beam parameters, so the atom velocities are consistent between the data sets. At these velocities, the atoms are level with the top of the copper plate after 1.8 ms from the atoms being pushed from the trap and are level with the bottom of the copper plate after 2.7 ms. In figure 5.21 we see that at 2.0 ms after the atoms are pushed, the spin-flip condition is not met, even though by 2.0 ms the atom would be 1 cm ($0.2\,\mathrm{ms}\times 51\,\mathrm{ms}^{-1}$) lower than the top of the plate. It is only until 0.3 ms after passing the top of the copper plate that the condition is met. This could be explained by the fact that the region above the plate is close to the centre of the top guiding coil. This increases the magnetic field strength, hence a higher Larmour frequency would be produced and a faster axis rotation would be necessary to meet the spin-flip condition. In addition, having a stronger background field makes it harder for the phase object field to dominate the overall direction and rotate the quantisation axis quickly enough or by a large enough angle.

5.3.3 The phase object

To create the interferometer, switching on and switching off the phase object magnetic field is now done in the same push cycle. The phase change acquired between each spin-flip is encoded in the resulting interference. After this process, the spin states are spatially separated by the SG wire and the interference is observed as oscillations in the m populations. To change the acquired phase shift, adjustments can be made to either the magnetic field strength or the phase object length (the TTL pulse width).

Varying the phase object length with a high field strength

Here we use a phase object duration of $t = 1.4 - 4.0\,\mu\mathrm{s}$ which is equivalent to a 70-200 μm phase object length, for atoms travelling with an average velocity of $\approx 51\,\mathrm{ms}^{-1}$. The phase object duration is changed by increments of 0.1 μs and the changes in the m state populations are observed and compared with the model. This comparison is shown in figure 5.22 where the current supplied to the plate was again 2 A. The model of the m state populations was fitted to the experimental data using equations 2.23 and 2.26. Since t was given by the pulse generator with a negligible uncertainty, the magnetic field strength B was

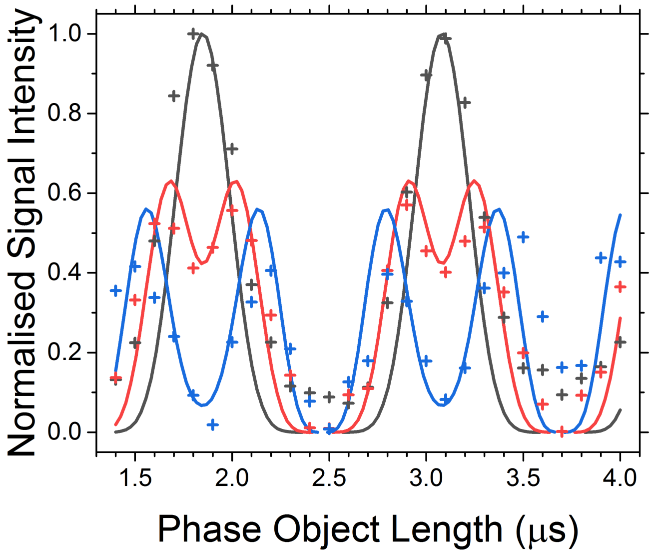

Figure 5.22: The $m = 0$ (blue), $m = 1$ (red) and $m = 2$ (black) populations as the length of the phase object is increased from 1.4-4 μs. The model was fitted using 2 parameters, the magnetic field strength, B, which determines the oscillation period and the spin-flip rotation angle θ_1 $(= \theta_2)$, which affects the relative peak heights. The data is normalised to clarify the relative peak heights.

left as a free parameter. From this, B was calculated to be 38.56 ± 0.22 μT with the uncertainty given in the parameter calculated with a 'variance-covariance' matrix during the Levenberg-Marquardt fitting algorithm in OriginPro. This gives a measurement for the average magnetic field strength through the phase object and is consistent with the calculated field strength from section 5.2.2. It is an average value since the total field magnitude will slightly change across the phase object due to z dependent contributions from the guiding coil.

The relative peak heights of each m state are dependent on the quantization axis rotation angle for the first and second spin-flips, θ_1 and θ_2. The data was compared with the model (section 2.2) and indicated a rotation angle of approximately $\frac{2\pi}{5}$. This is in broad agreement with the angles presented in section 5.3.2, which suggested that $\theta_{1,2} \approx \frac{\pi}{2}$.

Varying the phase object length with a low field strength

The measurement was repeated for a lower magnetic field strength, which was achieved by inserting a larger resistor in the phase object circuit. At 7.5Ω, the current was 1.7 A. The magnetic field strength was calculated to be $33.41 \pm 0.35\,\mu$T by again fitting to the data in figure 5.23. The switch-on time of the phase object (or the atoms' z positions during phase object interaction) was slightly later than the previous data. This means they are in a different field strength due to the guiding coils. This will contribute to a different overall field strength and also a different rotation angle for the spin-flip process and can be seen in the data as the maximum peak height ratios between the m states. The value for the rotation angle was estimated to be $\frac{3\pi}{7}$.

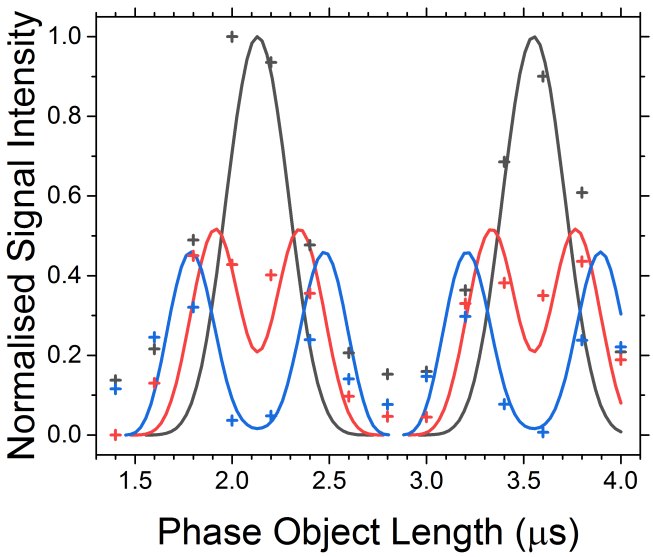

Figure 5.23: The $m = 0$ (blue), $m = 1$ (red) and $m = 2$ (black) state populations as the length of the phase object is increased with 1.7 A passing through the copper plate.

Magnetic field gradient parallel to the plate

So far the LSGI has only been tested with a phase object interaction time, t, of up to $4\,\mu$s, which is approximately an atom packet of length $200\,\mu$m, for atoms with a velocity of $51\,\mathrm{m\,s^{-1}}$. In order to develop the LSGI for a weak measurement, the phase object length needs to be of the order of millimetres, irrespective of the atomic velocity.

Testing was carried out with incrementally longer phase objects. When t was extended to 10 µs and beyond, a secondary m state oscillation begins to emerge. This secondary oscillation is along the y axis, across the length of the individual m state's signal, as shown in figure 5.24. When the phase object length is set so that the interference phases cause the $m = 2$ state to be maximally populated, you would expect the entire length of the $m = 2$ signal area to be illuminated. However, we can see in the detector signal that while the top section is illuminated, the bottom part isn't. As t increases, the bottom part becomes illuminated as the signal in the top part decreases. As t continues to change the $m = 2$ signal in the y axis, where the spatially separated $m = 2$ state atoms land, has an oscillating intensity.

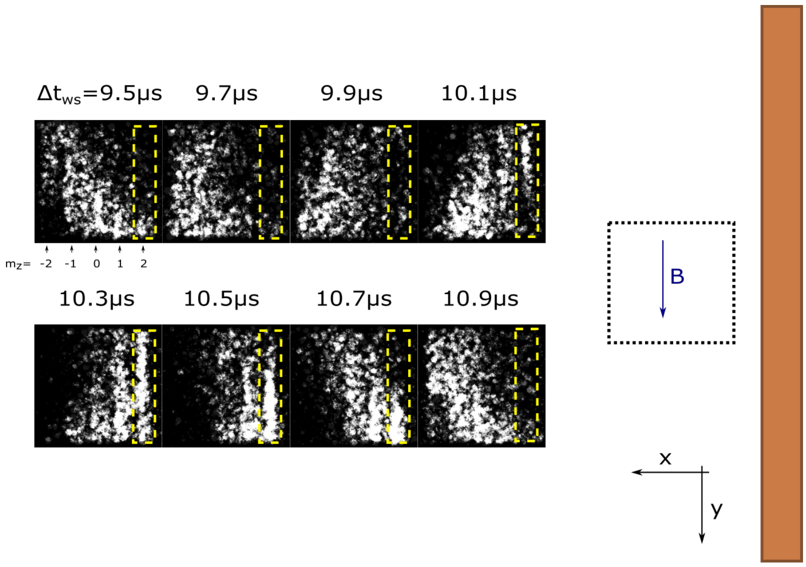

Figure 5.24: Raw data of the atomic beam signal on the detector. The beam has been split by the SG wire into five spatially separated m states. The empty box indicates where the atomic beam passes in relation to the copper plate and the direction of the associated B field. The signal is approximately 2 mm tall and wide. As the phase object pulse length is extended from 9.5 to 10.9 µs, the population of the states oscillate. The oscillation can be seen in the y direction due to a gradient in B_y.

This oscillation shows that the interaction strength was not uniform along the y axis i.e parallel to the copper plate. Since the interaction time is well-defined and fixed, the oscillating signal parallel to the plate must be due to a gradient in the y direction of the total magnetic field strength, B. This non-uniformity in B doesn't dominate the phase difference, ϕ, when using a short phase object length, t, as in the previous section, but slowly becomes more and more significant as t increases. The dependency of ϕ on B is exaggerated if t is increased since $\phi \propto Bt_{po}$

Testing of $\frac{\partial B}{\partial y}$ was done with a phase object pulse duration of $t = 10\,\mu\text{s}$. Much higher values of t induced a gradient too high to clearly observe the oscillation frequency. A quantitative analysis of this oscillation is in figure 5.25. For this data, the signal was measured for a 0.4 x 2.4mm region at the top and bottom of the signal.

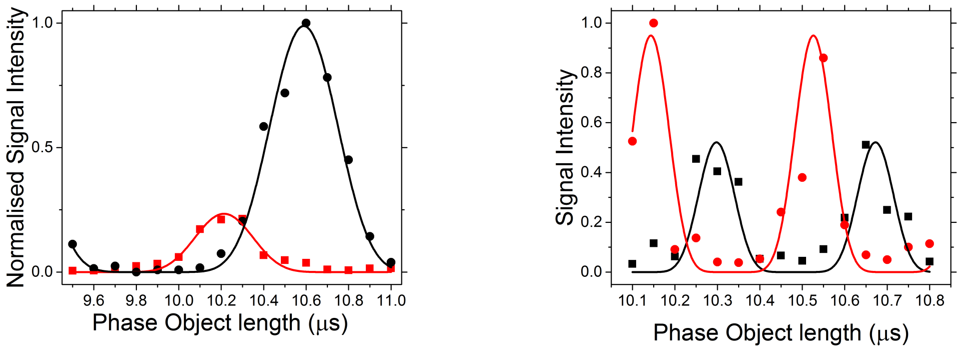

(a) (b)

Figure 5.25: The atomic signal intensity as the phase object interaction time is varied, for different sections of the $m = 2$ signal. Measurements are taken for the signal intensity at the top (black) and bottom (red) of the boxed region shown in figure 5.24. (a) shows the position of maximum signal intensity as the phase object interaction time is extended for a plate current of 1.7 A (b) shows the same measurement but for plate current of 10 A.

The peaks are again fitted using equation 2.24 and solved for B, the magnetic field strength. For a current of 1.7 A through the plate, the magnetic field strength changed between 38.17 ± 0.06 and $39.49 \pm 0.04\,\mu\text{T}$ along the 2 mm length of the signal in the y direction. This is a B gradient of $660\,\mu\text{T}\,\text{m}^{-1}$. Whereas in the case of 10A on the copper plate, the difference in field strength for the same two positions was between $122.43 \pm 0.1\,\mu\text{T}$ and $110.17 \pm 0.11\,\mu\text{T}$, a gradient of $6.13\,\text{mT}\,\text{m}^{-1}$. This increase in the magnetic field gradient indicates that a dominant source of the gradient is the current in the copper plate rather than the guiding coils or stray fields.

The magnetic field gradient parallel to the copper plate was measured using a Gaussmeter and shown in the data of figure 5.6. The change in magnetic field strength for 6 A of current, in the region of the atomic beam (1 mm either side of the centre of the copper plate, along y, and 2 mm away from the plate surface, along x) is 93 μT and 92.1 μT, giving a gradient of 300 $\mu\mathrm{T\,m^{-1}}$. This shows a discrepancy between the gradient measured with the LSGI and the gradient measured using the Gaussmeter.

At this point in the experiment, the plate was connected by only one wire on either end, whereas the measurements done on the bench top had the plate connected by two wires on each end. Within the LSGI, the current input was connected to the top corner and the ground to the bottom corner, on the same side as shown in figure 5.26(a),

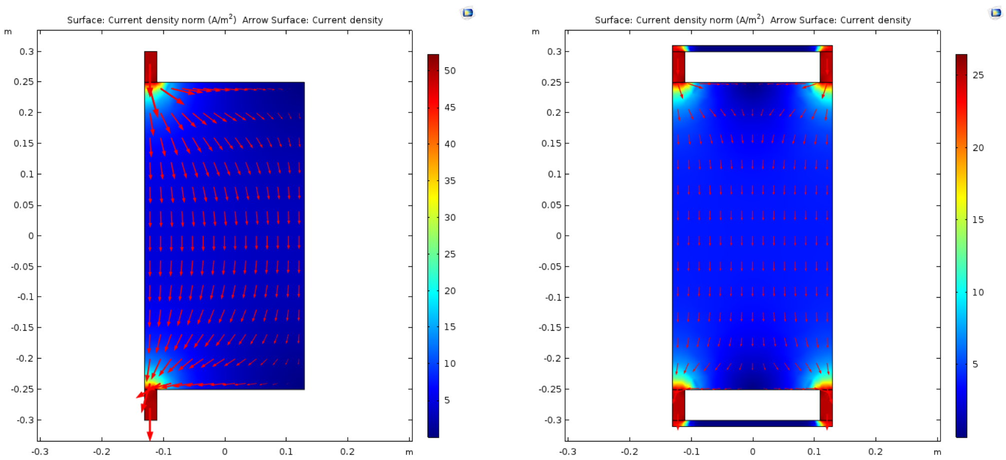

(a) (b)

Figure 5.26: COMSOL simulations of the current density and direction for (a) 2 terminals, both attached on the same side (b) 4 terminals, attached on all sides. The arrows indicate the current direction. When 2 terminals are used, the direction is not always completely parallel with the long edges of the plate and the current density is less uniform than when using 4 terminals.

The current density along the width of the plate, which would define the magnetic field strength at positions parallel to the plate is shown in figure 5.27, for a copper plate connected with one terminal at either end, and two terminals, one on each corner.

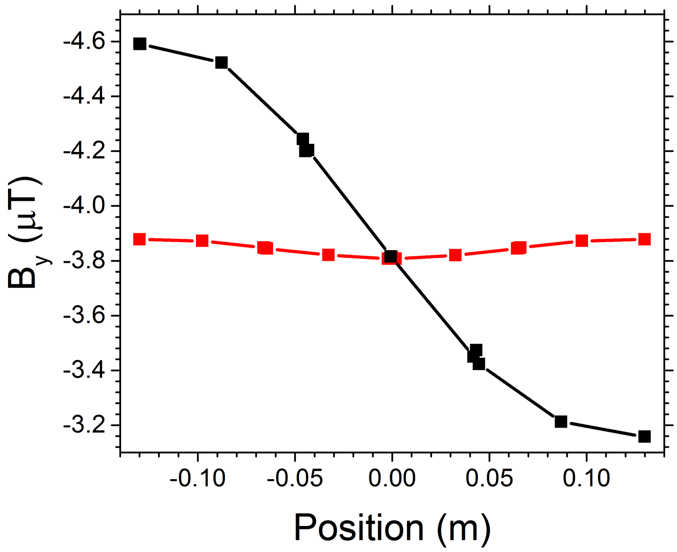

Figure 5.27: The copper plate field strength, B_y along the y axis for either 2 (black) or 4 (red) terminals connected to the plate. Modelled in COMSOL, this can be fully visualised in 2D in figure 5.26.

It was critical to minimise the non-uniformity along the plate for the subsequent weak measurement experiment. To do this, the copper plate was reconnected with 4 terminals as shown in 5.26(b). The guiding coils are modelled to have some non-uniformity in the radial direction (x or y). By also decreasing the current through the guiding coils and also the plate itself, all the contributions to any magnetic field gradients were reduced. The interaction time could be increased up to 80 μs without introducing significant oscillations in the y direction, as shown in figure 5.28

Analysing the data shows a magnetic field strength of 41.00 ± 0.03 μT and 40.28 ± 0.03 μT for the top and bottom respectively and an average gradient of 360 μT m^{-1} was measured over 4 mm longitudinally. This is a significant reduction compared to the gradient of 660 μT m^{-1} over 250 μm across the signal in the y axis for the case when the plate was connected using only two terminals.

The data also indicates a change in the rotation angle during the spin-flip

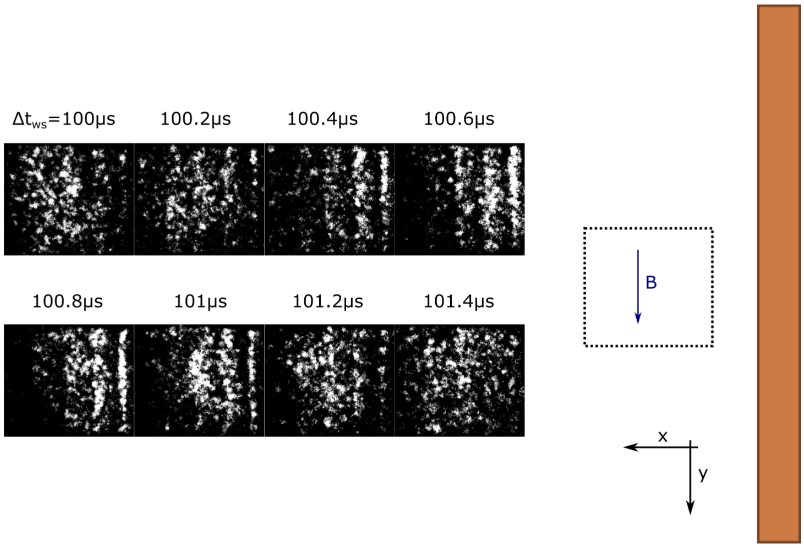

Figure 5.28: Raw data of the atomic beam signal on the detector. The beam has been split by the SG wire into five spatially separated m states. The empty box indicates where the atomic beam passes in relation to the copper plate and the direction of the associated B field. As the length of the phase object pulse is extended from 100 to 101.4 μs, the population of the states oscillate. There is little to no oscillation in the y direction.

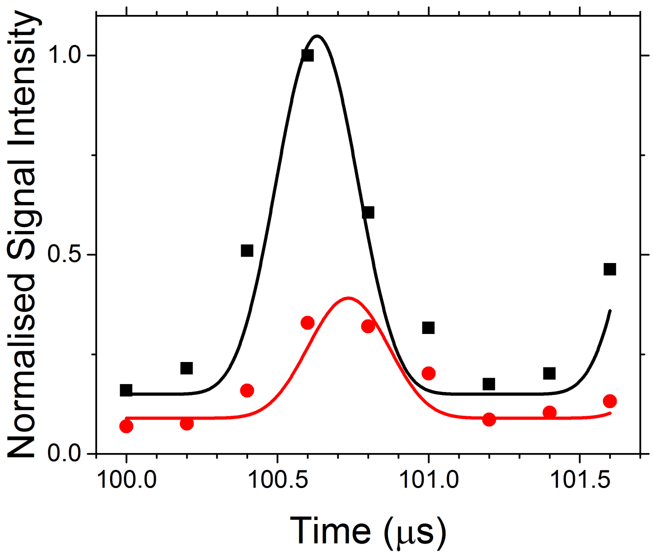

Figure 5.29: The signal intensity of the $m = 2$ state as the phase object interaction time is varied, for different sections of the signal for a plate current of 1.7 A. Measurements are taken for the signal intensity at the top (black) and bottom (red) of the boxed region shown in figure 5.28.

process. It can be seen that while the $m = 2$ state is maximally populated, there are still some atoms in the $m = 1$ state and even the $m = 0$ states. Referring to the simulated results for different rotation angles in figure 2.8, the populations of $m = 0, \pm 1$ when $m = 2$ is maximally populated, increase as the rotation angle moves away from 90°. Another result of an acute or obtuse rotation angle (rather than the 90° rotation) is that the $m = 2$ population/signal will never reach 0. This is observed in the raw data in figure 5.29.

Despite the oscillations in the population not being as distinctive for longer phase object lengths, the oscillations that the interferometer did produced could still be used to couple the m state population to the transverse momentum for a weak measurement. Extending the length of the phase object without seeing large magnetic field gradients was also a useful accomplishment. The atomic velocity used in this data is approximately $49\,\mathrm{ms}^{-1}$. At this velocity, a phase object interaction time of $80\,\mu\mathrm{s}$ equates to a phase object length of approximately 4 mm. Achieving m state interference using a 4 mm phase object length provides sufficient space to fit in a new tilted field for the weak measurement.

5.4 Conclusions

This chapter has demonstrated a measurement of the Zeeman phase shift acquired by metastable argon atoms, as a result of interacting with a magnetic field in an (LSGI). Two spin-state superpositions were created using a spin-flip process and the phase acquired between them is observed as interference fringes in the probability density of individual m states. The m states were observed separately using a state dependent force from the magnetic field gradient of a Stern-Gerlach (SG) wire.

For a given current of 1.7 A in the interferometer, a magnetic field strength of $33.41 \pm 0.35\,\mu\mathrm{T}$ was measured using the induced phase shift. The spatial distribution of the field strength was also measured. Using this technique, small gradients in the magnetic field strengths were measured.

The interferometer has demonstrated a measurement of magnetic field dependent phase shift in atomic spin states for a fixed interferometer interaction time. Modifying the LSGI such that the interaction is for a fixed magnetic field, but is dependent on time, indicates a path towards making a weak measurement of transverse momentum in a matter-wave interferometer.

Chapter 6

A weak measurement of the transverse momentum of an atom

The experimental results of this project have demonstrated the successful implementation of two important components required for a weak measurement of the atomic transverse momentum. This includes a multi-slit, matter-wave interferometer and the measurement of the Zeeman phase shift induced by a longitudinal Stern-Gerlach Interferometer (LSGI). Both have been achieved using the same metastable argon cold, atomic beam and detector. For measurements of transverse momentum, we aim to combine these two elements to create a weak measurement of the atom's transverse momentum in a matter-wave interferometer. In order to do this, the phase shift measured within the LSGI must be dependent upon the atom's transverse momentum. This is achieved by introducing a permanent magnetic field which is tilted with respect to the atomic beam's transverse axis. Such a magnetic field configuration ensures that the time which an atom spends in the field, and hence the observed phase shift, is dependent on its transverse momentum.

6.1 Experimental Sequence

The LSGI is modified from the experiment presented in chapter 5 to undertake weak measurements of transverse momentum. As before, the atomic beam is spin polarised and passes through the multi-slit grating, where the atoms diffract and acquire a new component to their transverse momentum. The atoms pass through the mu-metal cylinder, into a region of magnetic field created by the guiding coils. The field direction sets the atom's quantisation axis in the z direction. The atoms now fall past two copper plates, which replace the single copper plate to increase the magnetic field uniformity. When

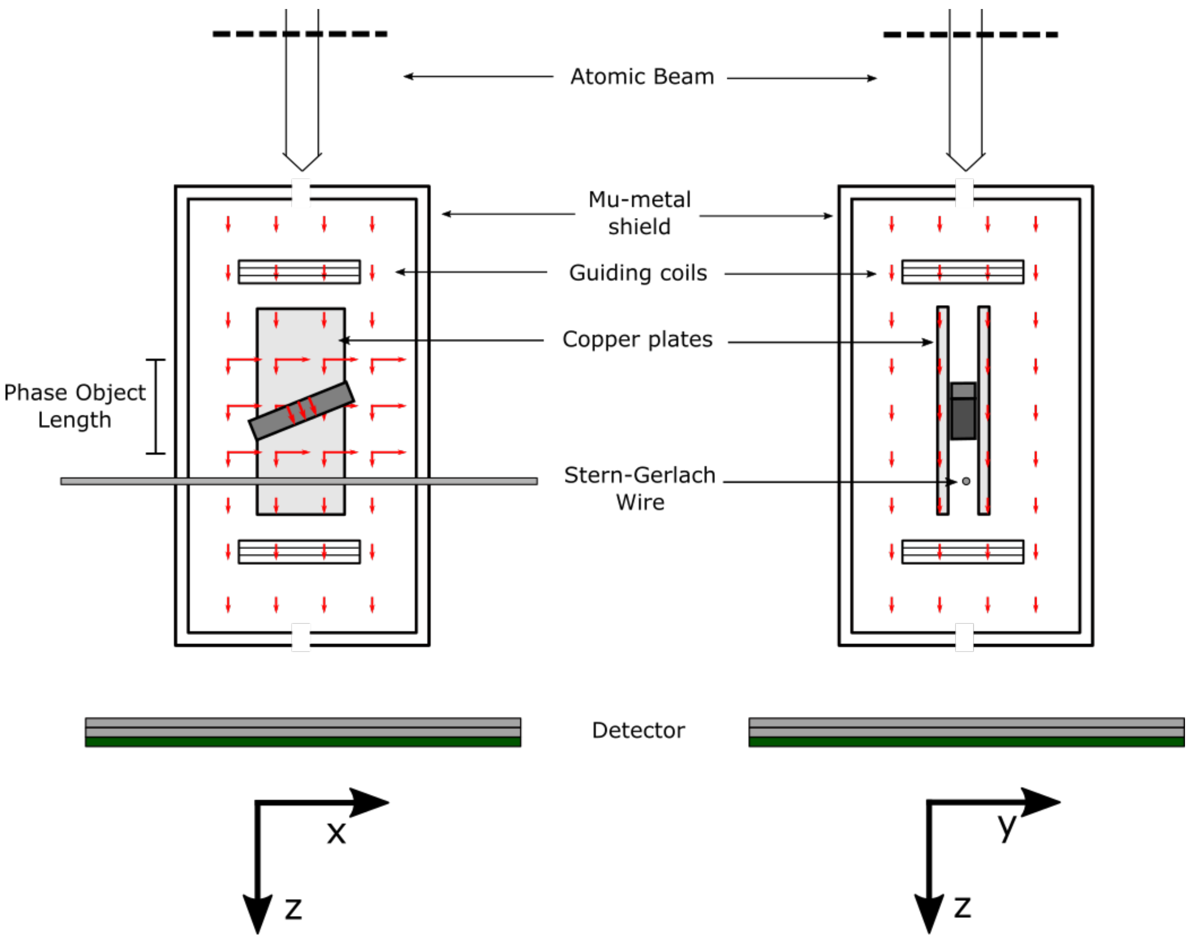

Figure 6.1: A schematic of the LSGI with the weak measurement stage included. The diagram shows the apparatus from two angles. The apparatus is generally the same as the LSGI (figure 6.1), although now there are two copper plates to improve field uniformity (one is removed in the xz view), the plates are rotated 90° and the tilted field is introduced.

the current through the plates is activated, the new transverse field direction rapidly rotates the atom's quantisation axis, creating a linear superposition of five spin states (m states). While in this state, the atoms fall through an additional weak measurement field, which is tilted to create the transverse momentum dependent interaction time. This field is the new addition that differentiates the experiment from the LSGI. The current for this field has no time dependence and is always constant. The atoms acquire a transverse momentum dependent phase shift of their spin due to the transverse momentum dependent interaction time.

The atoms fall through the weak measurement stage and remain in the phase object interaction stage until the current on the copper plate is switched off. At this point, as in the LSGI, the atom's quantisation axis is rapidly rotated back to the z axis and in doing so creates a new superposition of phase shifted m states. The new state creates interference in the probability density of the m state populations. The atoms then fall towards the detector and the individual m states are observed after a spatial separation via a Stern-Gerlach wire, or by optical quenching as previously described. The phase shift is observed as an intensity modulation of the interference pattern, allowing the transverse momentum to be measured.

6.2 Weak measurement design

Here, the design requirements for the magnetic field used for the weak measurement in terms of the geometry of the field, its spatial localisation and its uniformity are presented.

6.2.1 Creating a uniform field for the weak stage

In the LSGI, the phase shift in the atom's spin is measured using a pulsed current in a copper plate. The interaction time does not depend on the atomic momentum and cannot be used for a weak measurement of transverse momentum. The magnetic field of the weak measurement stage should allow the atom's interaction time to vary only according to the atom's transverse velocity. This means introducing a uniform, permanent, tilted magnetic field with fixed dimensions. This can be produced by a pair of thin wires, carrying equal currents in opposite directions, creating a magnetic field which is uniform along the length of the wires. The field direction, measured along the line which is equidistant from each wire, is perpendicular to the current direction, this is illustrated in figure 6.2.

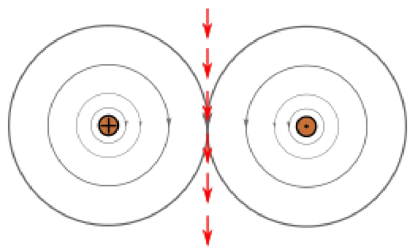

Figure 6.2: A cross section of the magnetic field created by two wires carrying current in opposite directions. The line bisecting the wires, has a field direction orthogonal to the wires.

To position the wires such that the magnetic field is uniform in the transverse x axis, the copper plates from the LSGI are rotated 90° so that they lie in the xz plane, instead of the xy plane used for the LSGI, this is shown in figure 6.1. The wires can then lie in the xz plane, unobstructed by the copper plates. The wire pair are separated by 2 mm shown in figure 6.3.

The wire pair are tilted by θ_t and set at 15° with respect to the y axis to create a transverse momentum dependent interaction time. The tilt angle is chosen such that the resulting phase shift distribution for a given magnetic field strength and distribution of transverse and longitudinal velocities, v_x, does not contain a phase shift greater than $\frac{\pi}{2}$ for all observed velocities. This ensures that the observed phase is approximately linear and no two v_x values give the same phase shift, $\phi(v_x)$. Atoms initially polarised in the $m = 2$ state, which pass through the spin-state interferometer and are detected in the $m = 0$ state will have a signal modulated by $\frac{3}{8}\sin\phi(v_x)^4$ (see equation 2.39).

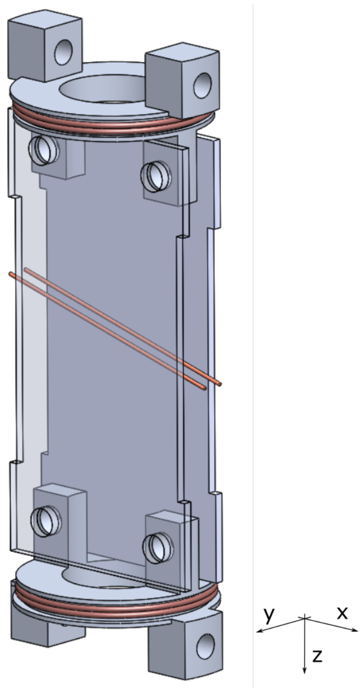

Figure 6.3: A CAD drawing of the how the wire pair would be positioned in the existing LSGI. The atomic beam passes through the centre of this apparatus along the z axis and towards the detector below. The two coils and the copper plates of LSGI are still used to set the quantisation axis and create a spin-flip, respectively.

The phase shift for a range of v_x is shown in figure 6.4. A peak magnetic field of 150 µT is chosen to give an approximately linear phase shift for the given weak measurement field design.

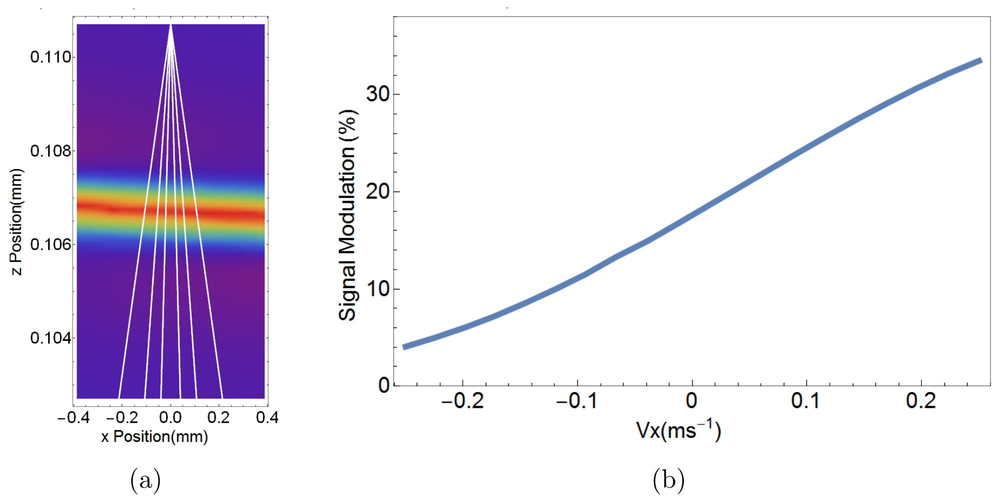

Figure 6.4: (a) The range of transverse velocities of an atom passing through the tilted field which has been diffracted by a multi-slit grating while travelling at 51 ms^{-1}. (b) The resulting modulation of the signal intensity, $\frac{3}{8}\sin\phi(v_x)^4$, for a range of transverse velocities and a field tilted at 15° to the transverse plane.

The new field direction within the weak stage is then 90-θ_t degrees from the quantisation axis set by the copper plates. The combined field strength of the copper plate and wire pair is shown in figure 6.6. As the atom falls through the wire pair, its quantisation axis rotates 75° and then -75° as it falls towards and away from the the wire pair. The atom's spin precesses about this field direction and the spin axis follows the changing field direction adiabatically for the atomic velocities achievable with the atomic beam. This rotation does not cause a spin-state re-projection since the rotation rate is slow and the spin-flip condition ($\omega_L \ll \omega_B$) is not met. Only the field strength is relevant here which we use to determine the phase shift.

The wire pair design also allows the magnetic field's z position to be adjusted. This means the weak measurement can be made at various distances from the grating to build up a map of the transverse velocities and reconstruct average momentum flow lines.

6.2.2 Localising the field

Introducing this new weak stage field into the existing phase object requires the field to be well localised in the z direction. The copper plate's magnetic field, must still be used to provide the spin-flip that creates the m state superposition in the LSGI. This new field could potentially interfere with the rotation rate and rotation angle of the spin-flip. Furthermore, magnetic field gradients will limit the length of the phase object and hence the weak stage. As described in section 5.2.2 and tested in section 5.3.3, the phase object length cannot exceed $\approx 80\mu s$ due to the field strength of the guiding coils and field gradients in the y direction across the face of the copper plate.

Localising the field is also important as the weak stage length defines the longitudinal spatial resolution of the weak measurement. To localise the field of the weak stage produced by the wire pair we use a mu-metal shield. This is in addition to the existing mu-metal shield that houses the LSGI. The wires are enclosed within a mu-metal rectangular tube measuring 1.5 x 3 x 22 mm. A empty volume between the wires and a slot in the centre allows atoms to pass through and interact with the magnetic field, as shown in figures 6.5 and 6.6.

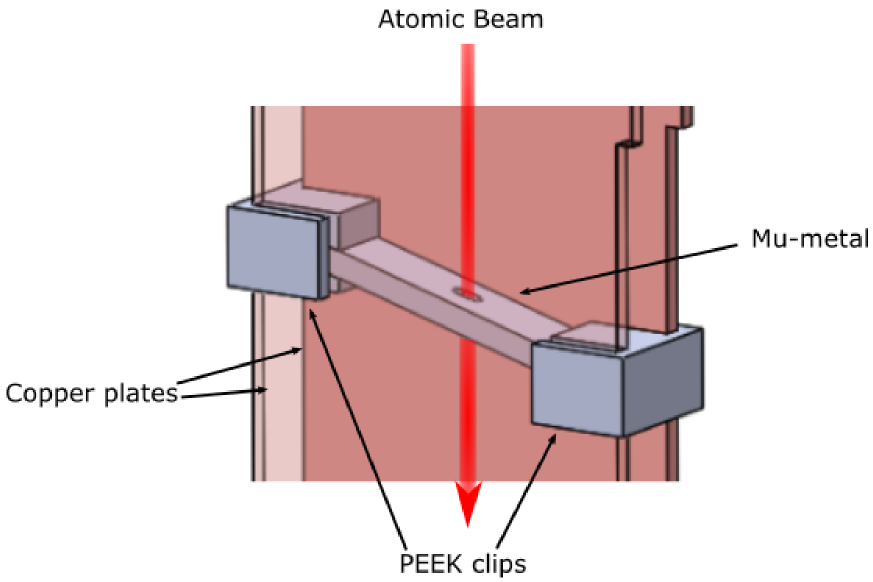

Figure 6.5: A CAD drawing showing the design for the mu-metal shield housing the wire pair. The shield is held at a fixed angle of 15° by two PEEK clips. The clips allow the weak measurement to be translated to different z positions. Also visible is the slot which allows the atomic beam to pass through. One of the copper plates has been made translucent to reveal the inner detail.

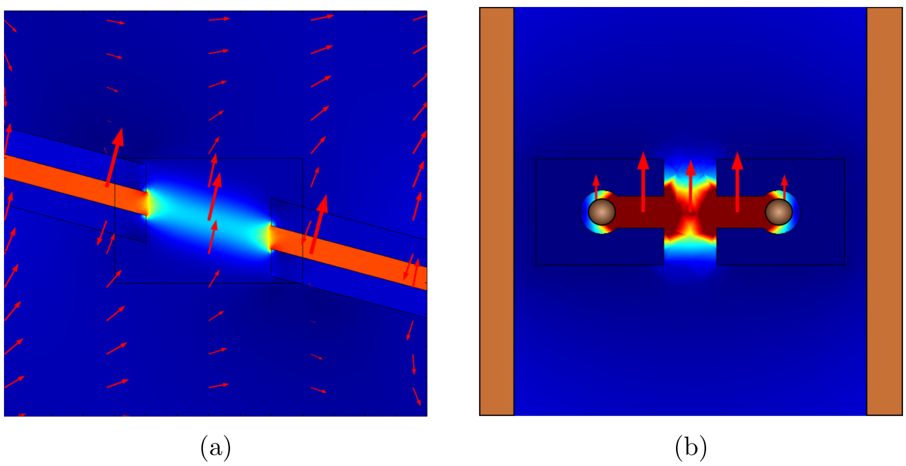

Figure 6.6: The direction and strength of the wire pair and the copper plate combined field, including the attenuation from mu-metal shield, modelled in COMSOL. This is the direction of the quantisation axis after the first spin-flip. (a) The field direction in the xz plane. (b) A cross section of the two wires and shield in the yz plane with the two copper plates on either side.

The slot creates an unavoidable problem of the slot reducing the effect of the shield in the region of the atomic beam. The size and shape of the slot is designed to achieve a balance between being large enough to allow a sufficient portion of the atomic beam through, but not too large such that the strength of the magnetic field significantly interferes with the magnetic field of the copper plates. Trying different designs in COMSOL showed the optimum shape had rounded corners and a width or height as narrow as possible. Given the matter-wave interferometer diffracted the atoms in the transverse x direction, the atomic signal in the y direction was not a priority. The final design is shown in figure 6.7

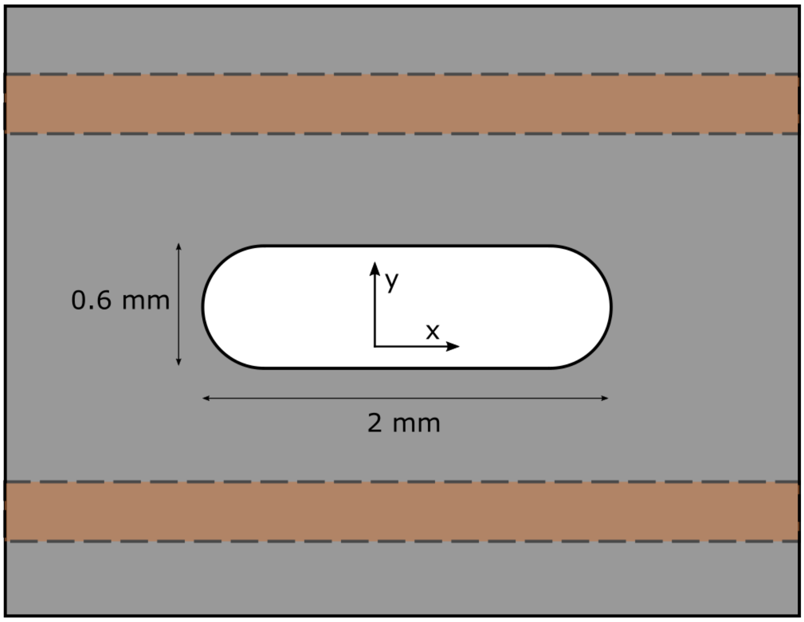

Figure 6.7: A view of the final slot design in the xy plane. The position of the wires within the shield are also indicated.

The combined field strength of B_x and B_z from the copper plate and the wire pair, for atoms passing through the centre of the slot and with no transverse velocity, is shown in figure 6.8. To calculate the effect that the wire pair have on the spin-flip process we recall that the probabilities of the m states when in superposition are dependent on the spin-flip rotation angle (section 2.2.1). Assume that the copper plate and wire pair would turn on at the same time. The spin-flip rotation angle is then between the z axis and combined

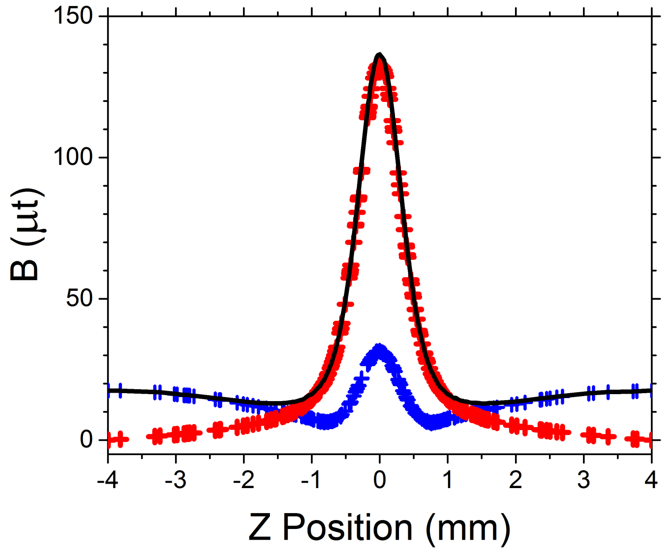

Figure 6.8: The B_x (blue crosses), B_z (red crosses) and B_{norm} (black line) magnitudes that an atom with $v_x = 0\,ms^{-1}$ experiences while travelling past the copper plate and then in addition, through the weak measurement field.

field direction of the copper plate and wire pair. The angle depends on the atom's position when the two fields are turned on, this is shown for 4 mm above and below the wire pair in figure 6.9.

In this representation, it is clear that the field from the wire pair will cause a spin-flip rotation angle of 60° or less at 2 mm above the wire pair. This will reduce the contrast of the spin-state interference fringes of the LSGI. However, by reversing the current on the wire pair, it may be possible to find a small region of field direction that keeps the rotation angle closer to 90°. It may also be possible to use a better combination of field strengths and tilt angles such that the wire pair field has a reduced effect on the copper plate field. A greater tilt angle would increase the angle from the vertical axis of the total magnetic field direction (copper plate and wire pair). Increasing the tilt angle also reduces the magnetic field strength needed from the wire pair to differentiate between the phase shifts for the atom's given transverse momentum distribution. This would also reduce the overall influence the wire pair field has on the copper plate field.

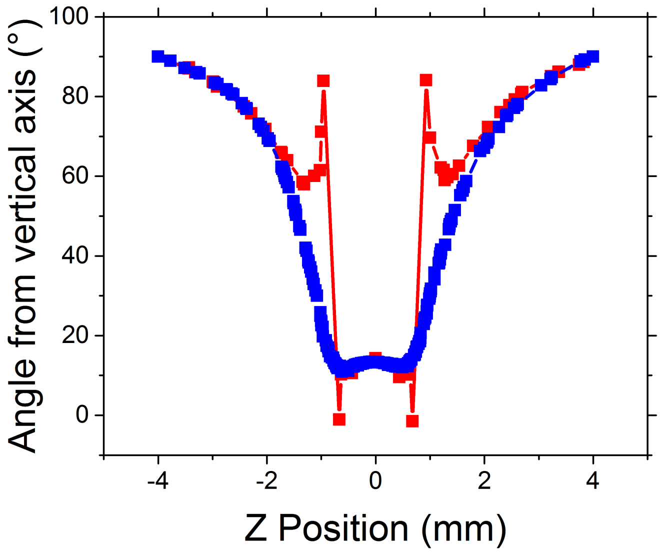

Figure 6.9: The spin axis rotation angle experienced by an atom that is quantised along the z axis and is then exposed to the combined field of the wire pair and the copper plates. The red and blue data show the angle for two opposite current directions and hence magnetic field directions. This is given for various positions from the position of the wire pair, z=0.

6.2.3 Transverse uniformity of the magnetic field

In the weak measurement region, the observed phase shift in the spin wavefunction is dependent on either a change in the magnetic field strength or a change in the interaction time. Therefore, in order to relate the phase shift to only the interaction time, the magnetic field strength must be sufficiently uniform across the region that the weak measurement is made.

The wire pair create field uniformity, along the length of the wires. However, introducing the mu-metal shield to localise the field deforms the areas of constant magnetic field strength. The area over which the weak measurement is made on the atoms is defined by the 2 x 0.6 mm slot in the mu-metal shield. The field around the mu-metal shield was modelled in COMSOL and a magnified area of the central region of figure 6.6(a) is shown in figure 6.10(a). The signal modulation is given for atoms with the same transverse velocity, but with a range of transverse positions. Again, this modulation is given by $\frac{3}{8}\sin\phi(v_x)^4$. Here, we show that for an arbitrary fixed transverse velocity,

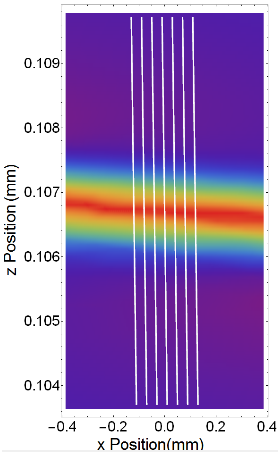

(a)

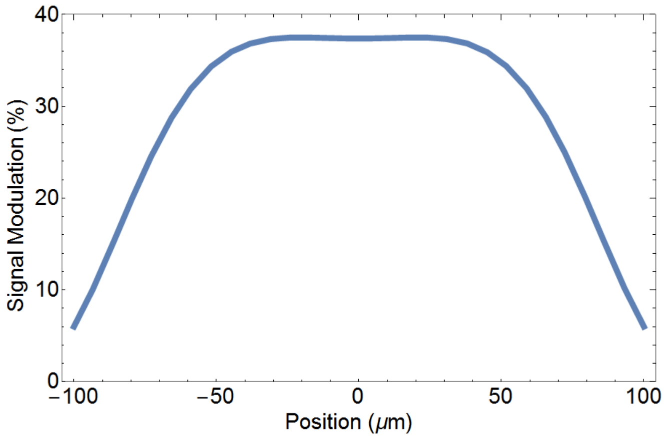

(b)

Figure 6.10: (a) Atom trajectories for a fixed transverse velocity are shown in white crossing the magnetic field strength of the tilted wire pair. (b) Shows the modulation of the atomic signal, due to the spin-state interferometer, as a function of position, for a fixed transverse velocity. The plot acts as a magnetometer and shows the region of uniformity in the x direction.

there is a 100 μm region of the weak measurement field that will give a uniform modulation of the signal intensity due to an almost uniform B field.

The area of this uniform region depends on the size of the slot in the mu-metal shield and the current in the wires. The width of the uniform region determines the transverse width of the interference pattern over which the weak measurement can be made. A small fluctuation of B across the chosen transverse length will contribute to the error in the measurement of transverse momentum. It should be noted that a change in B as little as 0.2 μT, will change the shape of the phase shift curve plotted in figure 6.10(b) such that the uniformity is lost. As a result, to achieve the desired uniformity, a very precise measurement and control of the magnetic field strength would be required.

6.2.4 Resolution of the measurement of transverse momentum

With the proposed design, the spatial resolution of the weak measurement of the transverse momentum is not sufficient to observe precise details of the atom's transverse momentum distribution, such as the spikes discussed in section 2.3.1.

The longitudinal spatial resolution of the transverse momentum measurement is an average value taken over the length of the phase object. This is at best 2 mm in the current design. However, the simulations show that the kinks occur over distances of ≈ 0.1 mm or less. In the near field of the matter-wave interferometer (figure 2.14(a)), the kinks would be too close together and would not be observed. If the longitudinal resolution of the weak measurement

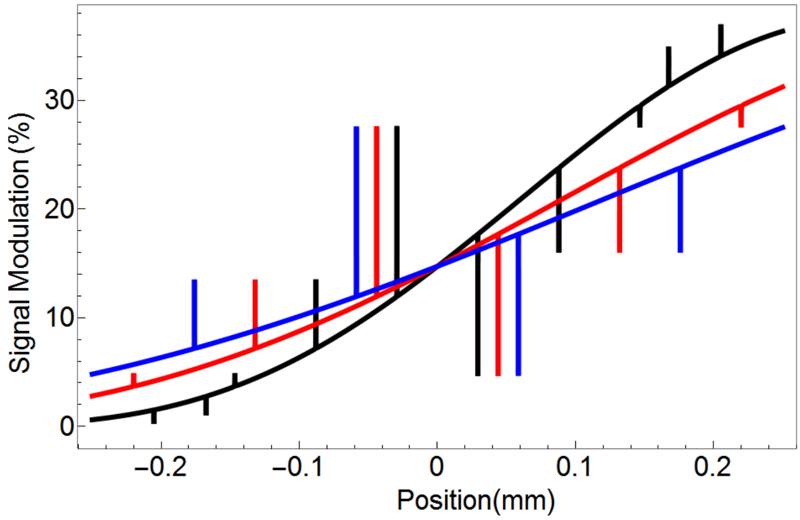

Figure 6.11: The signal intensity modulation due to a transverse momentum dependent m state phase shift, for atoms exiting the weak stage in $m = 0$. The plot effectively shows the transverse momentum dependence of the phase shift and this is shown for measurements taken at 3 distances from the grating, 40 mm (black), 60 mm (red) and 80 mm (blue).

is infinitely small, like in figure 6.11, then the spikes begin to appear when the plot uses an x data-point resolution of 2 μm or less. However, the width of the spikes will be affected by the longitudinal resolution. The width may increase if the longitudinal resolution is decreased. i.e. if a measurement made over a longer vertical distance. Figure 6.12 shows a magnified view of one of the spikes for three different longitudinal resolutions. In this case the transverse resolution is infinitely small.

For the measured transverse momentum to be coupled with a position, the MCP detector should coincide with the end of the phase object magnetic field. In this configuration, the detector's resolution in the x axis limits how close

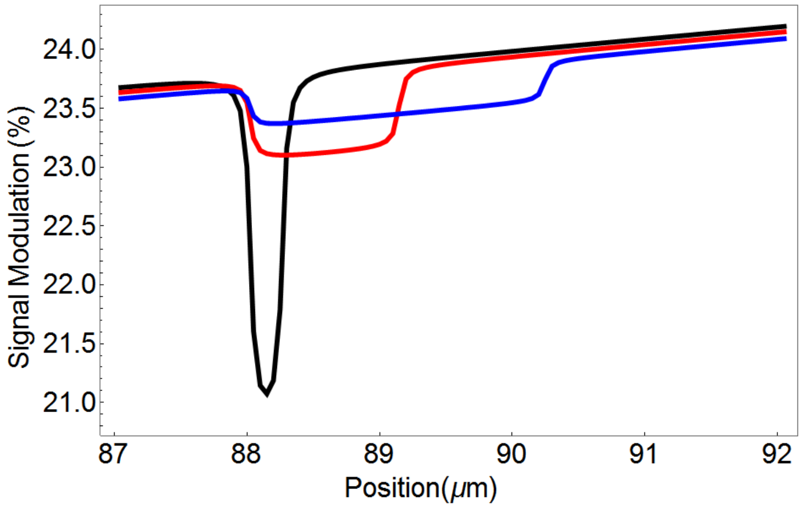

Figure 6.12: The signal modulation due to changes in the atom's transverse momentum across a small region containing the characteristic 'spikes' or 'kinks' in the atom's momentum. The plot shows the average transverse momentum measured using a weak stage length of 100 µm (black), 500 µm (red) and 1 mm (blue).

to the grating we can measure the spikes. For example, three pixels would be needed to resolve two spikes, given the current detector resolution limit of 11.4 µm, meaning the spikes would be separated by 22.8 µm. The spikes should occur with roughly same separation distance as the fringes, therefore the minimum grating-detector distance would be approximately 40-10 mm for atoms travelling at 50-12 ms^{-1}. Any measurement closer to the grating would not be possible.

6.3 Further experimental considerations

In order to realise the weak measurement of transverse momentum, the following points would need to be considered.

Measuring the transverse magnetic field uniformity

The magnetic field uniformity of the wire pair can be measured by setting $\theta_t = 0$. In this configuration, each atom within the detector's exposure window will spend approximately the same period of time interacting with the weak measurement magnetic field. Therefore, any modulation observed in the probability density will have arisen due to modulation in the magnetic field strength alone. From this, the field strength and region of uniformity could be characterised. This would need to be performed before any weak measurement.

Longitudinal uniformity of the magnetic field

This concerns the deflecting force that would arise from the gradient in the z direction as the atom passes through the weak stage. The mathematical description of the weak measurement assumes that the magnetic field is uniform throughout the interaction. In this simplified case, there is a small gradient upon entry to, and exit from, the field, but the atom's accumulated phase can simplified as a change in the Larmor frequency due to a magnetic field B, $\omega_L = \frac{g_f \mu_B B}{\hbar}$. As discussed, the wire pair create a transversely uniform field, however, there is no uniformity in the longitudinal direction. This gradient means there is an additional force deflecting each m state and for a tilted field there is a limit to how steep the gradient can be before the wavepacket is spatially separated according to its m states, via the Stern-Gerlach effect.

Position-measurement coupling

In order to relate the measurement of transverse momentum to a transverse position, the final position detection should be made as close as possible to the end of the weak measurement field. This means that the detector should have the capability to move in the z direction, along the beam axis. The detector that has been used is a standard 2-dimensional MCP detection stack with a modified design so the stack is removable from its flange. The stack is secured to the flange at three points using long screws. The screws can be replaced with threaded pillars and a lock-nut mechanism which would allow the distance between the stack and the flange, to be adjusted and fixed.

In addition, the phase object would need to be modified for it to be positioned close to the top of the detector. In its current form, with the guiding coils and the copper plates, the closest that the detector could realistically get to the measurement position is approximately 30-40 mm.

6.4 Conclusions

A design for a weak measurement of transverse momentum of an atom in a matter-wave interferometer has been presented. The design combines a multi-slit matter-wave interferometer and a modified longitudinal Stern-Gerlach interferometer (LSGI) to infer the atomic transverse momentum from the phase shift observed in the atom's spin states. The LSGI is tilted with respect to the atomic beam's transverse axis such that the interaction strength of the interferometer's magnetic field is dependent on the interaction time.

The design was modelled to show the limitations of the apparatus in terms of the spatial resolution of the weak measurement.

Chapter 7

Summary and conclusions

7.1 Summary of Experiments

7.1.1 Velocity-tuneable cold atomic beam

An atomic beam for a weak measurement of transverse momentum in a matter-wave interferometer requires a metastable atomic beam with a well-defined and narrow velocity distribution. This requirement led to the creation of a metastable argon atomic beam generated by applying radiation pressure from a laser to a cloud of cold trapped atoms. The resultant atomic beam was then velocity-tunable over a wide range by adjusting the properties of the push beam. Longitudinal velocities in the range of 1-50 ms^{-1} were demonstrated by adjusting the push beam frequency or pulse length and were shown to be suitable for the mater-wave interferometry experiment. The transverse and longitudinal coherence length of the beam was sufficient to resolve interference fringes for atomic velocities of up to approximately 18 ms^{-1}.

A closed cycle transition in the atom's metastable state was used to spin polarise the atomic beam when the light was left or right circularly polarised, with this an atomic beam in a pure $m = -2$ or $m = 2$ state was prepared. This important step was required for the construction of the spin-state interferometer.

7.1.2 Matter-wave interferometer

A multi-slit matter-wave interferometer was constructed for a weak measurement of transverse momentum of an atom. While the primary reason for building the interferometer was for weak measurements, the interference pattern was also used to characterise the atomic beam and to make a measurement of the Van der Waals C_3 coefficient.

The fringe spacing was used to measure the average longitudinal velocity of the atomic beam at the position of the grating. This velocity measurement was considered an improvement over the typical time-of-flight (TOF) velocity measurement and shows a new method for characterising the atomic beam. Additionally, the Van der Waals coefficient C_3 was measured. To our knowledge this was the first time such a measurement has been made for metastable argon.

7.1.3 Longitudinal Stern-Gerlach interferometer

The experiment demonstrated a measurement of the atom's Zeeman phase shift acquired by metastable argon atoms, as a result of an interaction with a magnetic field in a longitudinal Stern-Gerlach interferometer (LSGI). The successful demonstration of this was important for the design of the weak stage.

The average magnetic field strength within the interferometer was also measured from these phase shift measurements. The spatial distribution of the field strength could also be measured since the phase shift was observed for atoms with different paths through the interferometer. Using this technique, small gradients in the magnetic field strengths were measured. These measurements were important as they affect the final application of the weak measurement of transverse momentum using a modified LSGI.

Based on this work I designed and modelled a feasible scheme to undertake weak measurements of transverse momentum. This involved tilting the magnetic field of the LSGI such that the interaction strength that determines the atom's phase shift is dependent on the time that the atom spends in the field. With this, the observed phase shift taken from the spin-state interference pattern can be used to determine he atoms transverse momentum.

7.1.4 A weak measurement of atomic transverse momentum in a matter-wave interferometer

A design for a weak measurement of transverse momentum of an atom in a matter-wave interferometer was presented. The design combines the multi-slit matter-wave interferometer and the longitudinal Stern-Gerlach interferometer, both previously tested. The design was modelled and experimental results were simulated. The modelling data directed the experimental design based on suitable magnetic field strengths and geometries. Initial steps were taken in the construction of the experiment and the work presented informs of limitations of the design in terms of the spatial resolution of the measurement.

7.2 Improvements to the experiment

7.2.1 Increasing throughput/signal

The interferogram from the lowest velocity beam passing through the multi-slit grating, matter-wave interferometer was acquired over ≈ 50 hours. This long acquisition time was due to the low beam density used in the interferometer. To reduce the necessary acquisition time and allow clearer measurements, the throughput of the interferometer could be improved.

The source contains a very wide range of transverse velocities relative to the range which the collimation slits select. Therefore, to increase the throughput, the transverse velocities of the atoms in the MOT would need to be reduced. This could be done by further cooling atoms in the trap by further increasing the cooling beam detuning. In the case that the MOT operates in the lower range of the typical trap temperatures, it is also feasible to further reduce the transverse velocities by using a transverse cooling beam during the push phase. A pair of cooling beams, with the same polarisation configuration as the MOT cooling beams, would transversely intersect the atomic beam between the MOT position and the first slit. However, this could potentially change the spin polarisation of the atomic beam.

Assuming the throughput is maximised, the final observed signal of the spin-state interferometer could also be increased by choosing to observe a different final m state. The available space in the experiment meant the m states could be separated provided the beam has a narrow transverse velocity. In the weak measurement, the beam would diverge in x and y such that the spin-states could not be separated and resolved using the SG wire. Instead, the 'quench' method could be used to measure $m = 0$, the population of which is modulated by the function $\frac{3}{8}\sin[\phi(v_x)]^4$. Therefore, the maximum possible signal intensity is 37.5% of the total atomic beam intensity, since we discard the signal from other m states. However, the modulation for $m = \pm 2$, given by $\sin[\phi(v_x)/2]^8$, would produce a signal with a maximum intensity of 100% of the total atomic beam intensity.

Selecting only the $m = \pm 2$ states would be possible using right or left circularly polarised light in the quench beam. It would also require the quantisation axis of the atoms to be aligned with the axis of the quench beam (x axis), in the region where the quench beam intersects the atomic beam. This would require an additional magnetic field source since the background magnetic field is in the z direction.

7.2.2 Modifying the current weak stage design

One major problem highlighted in the thesis is that the spatial resolution of the weak measurement may not be sufficient to measure precise values of the atom's transverse momentum distribution.

The micro-channels in the experiment's detector were close to the smallest width possible and may not be small enough to observe the kinks close to the grating. To improve the transverse resolution of the weak measurement, the dimensions of the matter-wave interference region would need to be changed to expand the fringe spacing and resolve the pattern closer to the grating. A larger grating period or grating to detector distance, would increase the distances over which the kinks occur. This can be seen in the results from Kocsis's photon experiment [30] which is performed over 8 meters. The best possible spatial precision of the measurement is also dependent on the longitudinal resolution of the weak measurement interaction. The longitudinal resolution could be improved by miniaturising the wire pair and mu-metal shield that were used to create the transverse momentum dependent phase shift. To achieve this, printed electronic circuits can be created with current carrying components as small as $10\,\mu\text{m}$. These 'atom chips' have previously demonstrated manipulation of atoms including Stern-Gerlach interferometry [61, 62].

The guiding coils, which were used to set the quantisation axis of the atoms before and after the spin-state interferometer, created a uniform field direction along the atomic beam, but with a spatially varying magnetic field strength. The timing of the switch-on and switch-off of the interferometer was restricted to within a few millimetres of the central position of the two coils. Beyond that distance, the balance of the field strengths between the copper plates and the guiding coils would not create a superposition of m states. Additionally, the due to the gradient in the field strength, if the LSGI's measurement of the magnetic field strength is closer to the coils, it is less accurate.

Ideally, the quantisation axis should be a uniform field throughout the interferometer. This could've been achieved by constructing a solenoid that encloses the whole interferometer to set the quantisation axis.

7.2.3 Optical weak stage design

Considering the possible limitations to the magnetic weak stage that have been discussed, a number of alternative options were briefly explored. An interaction between atoms and photons would allow a much more localised interaction as laser beams can be focussed down to lengths of the order of 10μm.

Consider an atom, spin polarised in a stretched state, travelling longitudinally in the apparatus, with a small transverse component to its momentum. The atoms enters the optical field which is polarised such that the repeated absorptions of the photons will pump the atoms towards the opposite m state, via all the intermediary m states. The selection rules that allow this process were discussed in 3.6.4. The time that the atom spends in the laser field, will dictate the distribution of m state populations when the atom exits the beam.

7.3 Future work

Given that the project is a work in progress, the final chapter of the thesis overlaps with future work. When a weak measurement of transverse momentum can be made with sufficient resolution at one longitudinal position, the measurements at different z positions would need to be made in order to reconstruct the momentum flow lines. Theorists collaborating with this project are currently developing ideas of how the experiment could be modified to test the 'quantum potential' [63] which arises in Bohm's treatment of the Schrödinger equation, along with the phase representing the atom's local momentum.

The cold atomic beam and multi-slit matter-wave interferometer can be used to study unique atom-light interactions by illuminating the grating with a laser and observing the change in the interference pattern.

7.4 Concluding remarks

This thesis has taken the first steps towards making a weak measurement of the atomic transverse momentum in a multi-slit matter-wave interferometer. The experiments undertaken, together with simulations, have demonstrated how the individual components of such an experiment would work and has provided a useful platform for future experiments to explore the interpretations of quantum mechanics.

Appendix A

Appendices

A.1 Wigner matrix

From [64]

$$\begin{array}{c}
\begin{array}{ccccc} |-2\rangle & |-1\rangle & |0\rangle & |1\rangle & |2\rangle \end{array} \\
\begin{pmatrix}
\cos^4\frac{\theta}{2} & -\frac{1}{2}\sin\theta(1+\cos\theta) & \sqrt{\frac{3}{8}}\sin^2\theta & -\frac{1}{2}\sin\theta(1-\cos\theta) & \sin^4\frac{\theta}{2} \\
\frac{1}{2}\sin\theta(1+\cos\theta) & -\frac{1}{2}(1+\cos\theta(1-2\cos\theta) & -\sqrt{\frac{3}{2}}\sin\theta\cos\theta & -\frac{1}{2}(1-\cos\theta(1+2\cos\theta) & -\frac{1}{2}\sin\theta(1-\cos\theta) \\
\sqrt{\frac{3}{8}}\sin^2\theta & \sqrt{\frac{3}{2}}\sin\theta\cos\theta & \frac{1}{2}(3\cos^2\theta-1) & -\sqrt{\frac{3}{2}}\sin\theta\cos\theta & \sqrt{\frac{3}{8}}\sin^2\theta \\
\frac{1}{2}\sin\theta(1-\cos\theta) & \frac{1}{2}(1-\cos\theta)(1+2\cos\theta) & \sqrt{\frac{3}{2}}\sin\theta\cos\theta & -\frac{1}{2}(1+\cos\theta)(1-2\cos\theta) & -\frac{1}{2}\sin\theta(1+\cos\theta) \\
\sin^4\frac{\theta}{2} & \frac{1}{2}\sin\theta(1-cos\theta) & \sqrt{\frac{3}{8}}\sin^2\theta & \frac{1}{2}\sin\theta(1+\cos\theta) & \cos^4(\frac{\theta}{2})
\end{pmatrix}
\end{array}$$

for $\theta = \frac{\pi}{2}$ this gives

$$\begin{array}{c}
\begin{array}{ccccc} |2,-2\rangle & |2,-1\rangle & |2,0\rangle & |2,1\rangle & |2,2\rangle \end{array} \\
\begin{pmatrix}
\frac{1}{4} & -\frac{1}{2} & \sqrt{\frac{3}{8}} & -\frac{1}{2} & \frac{1}{4} \\
\frac{1}{2} & -\frac{1}{2} & 0 & -\frac{1}{2} & -\frac{1}{2} \\
\sqrt{\frac{3}{8}} & 0 & -\frac{1}{2} & 0 & \sqrt{\frac{3}{8}} \\
\frac{1}{2} & \frac{1}{2} & 0 & -\frac{1}{2} & -\frac{1}{2} \\
\frac{1}{4} & \frac{1}{2} & \sqrt{\frac{3}{8}} & \frac{1}{2} & \frac{1}{4}
\end{pmatrix}
\end{array}$$

Bibliography

[1] Schlosshauer, M., Kofler, J. & Zeilinger, A. (2013). A snapshot of foundational attitudes toward quantum mechanics. Stud. Hist. Philos. Sci. Part B - Stud. Hist. Philos. Mod. Phys. 44, 222–230.

[2] Bohm, D. (1952). A suggested interpretation of the quantum theory in terms of “hidden” variables. I. Physical Review, 85(2), 166–179.

[3] Philippidis, C., Dewdney, C. & Hiley, B.J., (1979). Quantum interference and the quantum potential. Il Nuovo Cimento B Series 11, 52(1), 15–28.

[4] Davisson, C., & Germer, L. H. (1927). The scattering of electrons by a single crystal of nickel. Nature, 119(2998), 558–560.

[5] Mitchell, P. & Powers, P. (1936). Bragg Reflection of Slow Neutrons. Physical Review, 50(5), 486-487

[6] Marton, L., Simpson, J. A., & Suddeth, J. A. (1953). Electron beam interferometer. Physical Review, 90(3), 490–491.

[7] Möllenstedt, G., & Düker, H. (1955). Fresnelscher Interferenzversuch mit einem Biprisma für Elektronenwellen. Die Naturwissenschaften, 42(2), 41.

[8] Jonsson, C. (1961). Elektroneninterferenzen an mehreren künstlich hergestellten Feinspalten. Zeitschrift Für Physik, 161(4), 454–474.

[9] Carnal, O., & Mlynek, J. (1991). Youngs double-slit experiment with atoms: A simple atom interferometer. Physical Review Letters, 66(21), 2689–2692.

[10] Arndt, M., O., Vos-Andreae, J., Keller, C., van der Zouw, G., & Zeilinger, a. (1999). Wave-particle duality of C(60) molecules. Nature, 401(6754), 680–682.

[11] Eibenberger, S., Gerlich, S., Arndt, M., Mayor, M., & Tüxen, J. (2013). Matter-wave interference of particles selected from a molecular library with masses exceeding 10,000 amu. Physical Chemistry Chemical Physics, 15(35), 14, 696–700.

[12] Nairz, O., Brezger, B., Arndt, M., & Zeilinger, A. (2001). Diffraction of complex molecules by structures made of light. Physical Review Letters, 87, 160401.

[13] Keller, C., Schmiedmayer, J., & Zeilinger, A. (2000). Requirements for coherent atom channeling. Optics Communications, 179(1), 129–135.

[14] Haslinger, P. et al. (2013). A universal matter-wave interferometer with optical ionization gratings in the time domain. Nature Physics, 9, February.

[15] Shimizu, F., Shimizu, K., & Takuma, H. (1992). Double-slit interference with ultracold metastable neon atoms. Physical Review A, 46(1), 17–21.

[16] Taillandier-Loize, T., Aljunid, S. A., Correia, F., Fabre, N., Perales, F., Tualle, J. M. & Dutier, G. (2016). A simple velocity-tunable pulsed atomic source of slow metastable argon. Journal of Physics D: Applied Physics, 49(13), 135503.

[17] Cacciapuoti, L., Castrillo, A., De Angelis, M., & Tino, G. M. (2001). A continuous cold atomic beam from a magneto-optical trap. European Physical Journal D, 15(2), 245–249.

[18] Aharonov, Y., Albert, D. Z., & Vaidman, L. (1988). How the Result of a Measurement of a Component of the Spin of a Spin 1/2 Particle Can Turn Out to be 100. Physical Review Letters, 60(14), 1351–1354.

[19] Starling, D. J., Dixon, P. Ben, Jordan, A. N., & Howell, J. C. (2010). Precision frequency measurements with interferometric weak values. Physical Review A - Atomic, Molecular, and Optical Physics, 82(6), 6–9.

[20] Magana-Loaiza, O. S., Mirhosseini, M., Rodenburg, B., & Boyd, R. W. (2014). Amplification of angular rotations using weak measurements. Physical Review Letters, 112(20), 1–5.

[21] Viza, G. I., Martínez-Rincón, J., Howland, G. a, Frostig, H., Shomroni, I., Dayan, B., & Howell, J. C. (2013). Weak-values technique for velocity measurements. Optics Letters, 38(16), 2949–52.

[22] Dixon, P. Ben, Starling, D. J., Jordan, A. N., & Howell, J. C. (2009). Ultrasensitive beam deflection measurement via interferometric weak value amplification. Physical Review Letters, 102(17), 1–4.

[23] Scully, M. O., Englert, B.-G., & Walther, H. (1991). Quantum optical tests of complementarity. Nature, 351(6322), 111–116.

[24] Hulet, R. G., Ritchie, N. W. M., & Story, J. G. (1997). Measurement of a weak value. Zeitschrift Fur Naturforschung - Section A Journal of Physical Sciences, 52(1–2), 31–33.

[25] Lundeen, J. S., & Steinberg, A. M. (2009). Experimental joint weak measurement on a photon pair as a probe of Hardy's paradox. Physical Review Letters, 102(2), 1–4.

[26] Yokota, K., Yamamoto, T., Koashi, M., & Imoto, N. (2009). Direct observation of Hardy's paradox by joint weak measurement with an entangled photon pair. New Journal of Physics, 11.

[27] Resch, K. J., Lundeen, J. S., & Steinberg, A. M. (2004). Experimental realization of the quantum box problem. Physics Letters, Section A: General, Atomic and Solid State Physics, 324(2–3), 125–131.

[28] Palacios-Laloy, A., Mallet, F., Nguyen, F., Bertet, P., Vion, D., Esteve, D., & Korotkov, A. N. (2010). Experimental violation of a Bells inequality in time with weak measurement. Nature Physics, 6(6), 442–447.

[29] Svensson, B.E.Y. (2013). Pedagogical review of quantum measurement theory with an emphasis on weak measurements. Quanta, 2(1), pp.18–49.

[30] Kocsis, S., Braverman, B., Ravets, S., Stevens, M. J., Mirin, R. P., Krister, S. L., & Steinberg, A. M. (2011). Science, 332, 1170-73

[31] Hiley, B. J., & Van Reeth, P. (2018). Quantum trajectories: Real or surreal? Entropy, 20(5).

[32] Berry, M. V. (2013). Five momenta. European Journal of Physics, 34(6), 1337–1348.

[33] Denkmayr, T., Geppert, H., Sponar, S., Lemmel, H., Matzkin, A., Tollaksen, J., & Hasegawa, Y. (2014). Observation of a quantum Cheshire Cat in a matter-wave interferometer experiment. Nature Communications, 5, 1–7.

[34] Shomroni, I., Bechler, O., Rosenblum, S., & Dayan, B. (2013). Demonstration of weak measurement based on atomic spontaneous emission. Physical Review Letters, 111(2), 1–5.

[35] Vanderbruggen, T., Kohlhaas, R., Bertoldi, A., Bernon, S., Aspect, A., Landragin, A., & Bouyer, P. (2013). Feedback control of trapped coherent atomic ensembles. Physical Review Letters, 110(21), 1–5.

[36] Smith, G. A., Chaudhury, S., Silberfarb, A., Deutsch, I. H., & Jessen, P. S. (2004). Continuous Weak Measurement and Nonlinear Dynamics in a Cold Spin Ensemble, (October), 1–4.

[37] Viaris de Lesegno, B., Karam, J. C., Boustimi, M., Perales, F., Mainos, C., Reinhardt & J. Robert, J. (2003). Stern Gerlach interferometry with metastable argon atoms: An immaterial mask modulating the profile of a supersonic beam. European Physical Journal D, 23(1), 25–34.

[38] Gondran, M. & Gondran, A., (2007). Numerical Simulation of the Double Slit Interference with Ultracold Atoms. American Journal of Physics, 507(2005), 25.

[39] Feynman, R. P. (1948). Space-time approach to non-relativistic quantum mechanics. Reviews of Modern Physics, 20(2), 367.

[40] Hecht, E. (1992). Optics. Addison-Wesley Publishing Company. 4th ed. Bonn.

[41] Tempelaars, J. G. C., Stas, R. J. W., Sebel, P. G. M., Beijerinck, H. C. W., & Vredenbregt, E. J. D. (2002). An intense, slow and cold beam of metastable Ne(3s) 3 P 2 atoms. European Physical Journal D, 18(1), 113–121.

[42] Slowe, C., Vernac, L., & Hau, L. V. (2005). High flux source of cold rubidium atoms. Review of Scientific Instruments, 76(10), 1–10.

[43] Lu, Z. T., Corwin, K. L., Renn, M. J., Anderson, M. H., Comell, E. A., & Wieman, C. E. (2008). Low-Velocity intense source of atoms from a magneto-optical trap. Collected Papers of Carl Wieman, 420–423.

[44] Wang, H., & Buell, W. F. (2003). Velocity-tunable magneto-optical-trap-based cold Cs atomic beam. Journal of the Optical Society of America B, 20(10), 2025.

[45] Pearson, B. J., Ferris, N., Strauss, R., Li, H., & Jackson, D. P. (2018). Measurements of slit-width effects in Young's double-slit experiment for a partially-coherent source. OSA Continuum, 1(2), 755.

[46] Grisenti, R.E., Schöllkopf, W. & Toennies, J.P., (1999) Determination of Atom-Surface van der Waals Potentials from Transmission-Grating Diffraction Intensities. Physical Review Letters, 83(9), 1755–1758.

[47] Lonij, V. P. A., Holmgren, W. F., & Cronin, A. D. (2009). Magic ratio of window width to grating period for van der Waals potential measurements using material gratings. Physical Review A - Atomic, Molecular, and Optical Physics, 80(6), 1–10.

[48] Brühl, R., Fouquet, P., Grisenti, R. E., Toennies, J. P., Hegerfeldt, G. C., Köhler, T. & Walter, C. (2002). The van der Waals potential between metastable atoms and solid surfaces: Novel diffraction experiments vs. theory. Europhysics Letters, 59(3), 357–363.

[49] Karam, J. C., Wipf, N., Grucker, J., Perales, F., Boustimi, M., Vassilev, G. & Robert, J. (2005). Atom diffraction with a "natural" metastable atom nozzle beam. Journal of Physics B: Atomic, Molecular and Optical Physics, 38(15), 2691–2700.

[50] Karam, J. C., Boustimi, M., Baudon, J., Ducloy, M., Perales, F., Reinhardt, J. & Robert, J. (2002). Endothermal fine-structure transition of metastable argon atoms passing through a micro-slit copper gratings. Europhysics Letters, 60(2), 207–213.

[51] Boustimi, M., Viaris de Lesegno, B., Baudon, J., Robert, J., & Ducloy, M. (2001). Atom symmetry break and metastable level coupling in rare gas atom-surface van der Waals interaction. Physical Review Letters, 86(13), 2766–2769.

[52] Douglas, P., Maher-Mcwilliams, C., & Barker, P. F. (2012). Frequency stabilization of an external-cavity diode laser to metastable argon atoms in a discharge. Review of Scientific Instruments, 83(6), 1–6.

[53] Edmunds, P.D., (2015). Trapping ultracold argon atoms. Diss. University College London

[54] Hoess, P. & Fleder, K. (2000). Time-integrated phosphor behavior in gated image intensifier tubes. Image Intensifiers and Applications II, 4128, 23.

[55] Bordé , C.J. (1989). Atomic interferometry with internal state labelling. Physics Letters A, 140(1–2), pp.10–12.

[56] Johnson, K. S., Thywissen, J. H., Dekker, N. H., Berggren, K. K., Chu, A. P., Younkin, R., & Prentiss, M. (1998). Localization of metastable atom beams with optical standing waves: Nanolithography at the Heisenberg limit. Science, 280(5369), 1583–1586.

[57] Gould, P.L., Ruff, G.A. & Pritchard, D.E. (1983). Diffraction of Atoms by Light: The Near-Resonant Kapitza-Dirac Effect. Physical Review Letters, 56, 46–52.

[58] Brezger, B., Hackermüller, L., Uttenthaler, S., Petschinka, J., Arndt, M. & Zeilinger, A. (2002). Matter-Wave Interferometer for Large Molecules. Physical Review Letters, 88(10), 4.

[59] https://www.ngdc.noaa.gov/geomag/calculators/magcalc.shtml

[60] Dubbers, D., (1986). Simple formula for multiple mu-metal shields. Nuclear Instruments and Methods in Physics Research Section A: Accelerators, Spectrometers, Detectors and Associated Equipment, 243, 511–517.

[61] Petrovic, J. et al., (2013). A multi-state interferometer on an atom chip. New Journal of Physics, 15.

[62] Machluf, S., Japha, Y. & Folman, R., (2013). Coherent Stern-Gerlach momentum splitting on an atom chip. Nature Communications, 4, 1–9.

[63] Flack, R. & Hiley, B.J.(2018). Feynman paths and weak values. Entropy, 20(5), pp.1–11.

[64] Wigner, E. (2012). Group theory: and its application to the quantum mechanics of atomic spectra (Vol. 5). Elsevier.